UNIVERSIDAD DE CHILE
FACULTAD DE CIENCIAS FÍSICAS Y MATEMÁTICAS
DEPARTAMENTO DE FÍSICA

DYNAMICS OF PARTICLE-LIKE SOLUTIONS IN NON-LOCAL SYSTEMS

TESIS PARA OPTAR AL GRADO DE
MAGÍSTER EN CIENCIAS MENCIÓN FISICA

MARTIN LUKAS BATAILLE GONZALEZ

PROFESOR GUÍA:
MARCEL CLERC GAVILAN

MIEMBROS DE LA COMISIÓN:
MARCEL CLERC
KARIN ALFARO
OLEH OMEL'CHENKO
IGNACIO BORDEU
MUSTAPHA TLIDI

SANTIAGO DE CHILE
2024

Resumen

Esta tesis está dedicada al estudio y caracterización de la dinámica de estructuras localizadas en sistemas no locales. Más específicamente, este trabajo abarca el estudio de dos tipos de estructuras localizadas en sistemas distintos, a saber, solitones disipativos en una cavidad de fibra de cristal fotónico, y quimeras espirales en arreglos bidimensionales de osciladores de fase acoplados no localmente. En ambos sistemas, se observa la aparición de estructuras localizadas móviles mediante distintos mecanismos, los cuales son correspondientemente identificados y discutidos.

En el Capítulo 1, se presenta una breve introducción a las estructuras localizadas y a los sistemas no locales, junto con el alcance y los objetivos de esta tesis. El Capítulo 2 proporciona los conceptos teóricos esenciales necesarios para comprender los capítulos siguientes, mientras que el Capítulo 3 introduce el método de continuación numérica empleado en los capítulos posteriores.

La primera parte de la investigación realizada en esta tesis se compone de los Capítulos 4 y 5, y está dedicada al estudio de solitones disipativos en cavidades de fibra de cristal fotónico bajo distintos efectos no locales. En particular, el Capítulo 4 está dedicado a la caracterización y análisis de solitones brillantes y oscuros móviles sujetos al efecto Raman y considerando dispersión de cuarto orden. Un sistema similar es considerado en el Capítulo 5, con la diferencia de que los dos términos anteriores son reemplazados por un filtro espectral, que surge de la adición de una rejilla de fibra al sistema.

La segunda parte está compuesta por los Capítulos 6 y 7, y se centra en quimeras espirales móviles en poblaciones de osciladores de fase acoplados. Comenzando con el Capítulo 6, se revela la existencia de estas estructuras, y se caracteriza su dinámica basada en simulaciones numéricas. Posteriormente, el Capítulo 7 profundiza el análisis a través del método de continuación numérica y métodos semi-analíticos, proporcionando una descripción detallada de la aparición y estabilización de quimeras espirales móviles.

Finalmente, el Capítulo 8 presenta las principales conclusiones de esta tesis.

Abstract

This dissertation is devoted to the study and characterization of the dynamics of localized structures in non-local systems. More specifically, we focus on two different kind of localized structures arising in different systems, namely, dissipative solitons in a photonic crystal fiber cavity, and spiral chimeras in two-dimensional arrays of nonlocally coupled phase oscillators. In both systems, we observe the emergence of moving localized structures due to distinct mechanisms, which we identify and discuss.

In Chapter 1, a brief introduction to localized structures and nonlocal systems is presented, along with the scope and objectives of this thesis. Chapter 2 provides the essential theoretical concepts needed to understand the following chapters, while Chapter 3 introduces the numerical continuation method employed in the subsequent Chapters.

The first part of the research made in this dissertation consists of Chapters 4 and 5, and is dedicated to the study of dissipative solitons in photonic crystal fiber cavities under different nonlocal effects. In particular, Chapter 4 is dedicated to the characterization and analysis of moving bright and dark subject to the Raman effect and considers fourth order dispersion. A similar system is considered in Chapter 5, with the difference that the two former terms are replaced by a spectral filter, arising from the addition of a fiber grating to the system.

The second part is composed of Chapters 6 and 7, and focuses on moving spiral chimeras in populations of coupled phase oscillators. Starting with Chapter 6, the existence of these structures is revealed, and their dynamics are characterized based on numerical simulations. Subsequently, Chapter 7 deepens the analysis through numerical continuation and semi-analytical methods, providing a detailed description of the emergence and stabilization of moving spiral chimeras.

Finally, Chapter 8 presents the main conclusions of this dissertation.

tbd.

\- *tbd.*

Acknowledgments

tbd

Contents

Chapter 1

Introduction

Almost a century ago, our understanding of elementary or quantum particles went through a complete change of paradigm. Indeed, what was originally thought to be a microscopic speck of matter with a well-defined position, momentum and size was discovered instead to be a localized field that occupies all space, and whose amplitude is related to the probability density [1–3]. As a consequence, the former quantities of position and momentum were replaced by expectation values. Conversely, the concept of a particle as a localized field was extended to meso- and macroscopical systems, typically described by extended fields. In fact, Nicolis and Prigogine argued that the energy transfer present in these systems allows for a rich variety of complex and stable structures to form, including localized structures [4, 5]. These localized states or particle-like solutions are thus supported by a robust balance between gains and losses and have been observed in a variety of systems due to their universality [6–10].

Traditionally, the mathematical description of localized structures has been carried out using reaction diffusion models or their generalizations with higher order derivatives [11–13]. As the name suggests, the spatial coupling occurs through diffusive (or hyperdiffusive) terms and, therefore, is solely local. Nevertheless, various optical [14], neural [15] and even vegetation [16] systems present a more complex and far-reaching coupling, usually called nonlocal coupling. In these cases, it has been found that the nonlocal term gives rise to richer dynamics and is often responsible for the stabilization of particle-like solutions [17, 18]. Mathematically, the nonlocal term is usually modeled as an integral operator, which strongly limits the analytical and numerical tools available to study these systems. Consequently, the dynamics of localized structures in nonlocal systems are still not well understood.

The aim of this dissertation is to provide an in-depth study and characterization of the dynamics of localized structures in non-local systems. In particular, we will focus on two different systems: dissipative solitons in a photonic crystal fiber cavity, and spiral chimeras in two-dimensional networks of heterogeneous phase oscillators. In both cases, we observe the emergence of uniformly moving localized structures due to different mechanisms, which we will identify and analyze.

1.1 Contents

This dissertation is a compilation of four articles that have been published or submitted to peer-reviewed journals. For each article, there is an associated chapter containing a brief introduction to the subject, along with a short discussion at the end.

The first three chapters of this dissertation are dedicated to the theoretical and numerical background necessary for the subsequent chapters. More specifically, Chapter 1 corresponds to the present introduction, and provides an overview of the context and scope of the dissertation. Chapter 2 introduces the main concepts and theory needed to approach the current study. In Chapter 3, an introduction to numerical continuation, the main numerical method used in the following articles, is presented.

The following four chapters contain the core of the dissertation, which is divided into two main parts. The first part contains Chapters 4 and 5, and focuses on dissipative solitons in photonic crystal fiber cavities, under different asymmetric nonlocal effects. Starting with Chapter 4, the formation of isolas of solitons due to the Raman effect is studied. In Chapter 5, a similar system is considered under a different nonlocal coupling, arising from the addition of a spectral filter.

On the other hand, the second part of the dissertation is devoted to the study of moving spiral wave chimeras in a two-dimensional array of nonlocally coupled phase oscillators. In particular, Chapter 6 reveals the existence of these structures and characterizes their dynamics based on direct numerical simulations. Chapter 7 extends the analysis through numerical continuation and semi-analytical methods, and provides a detailed description of the bifurcations that lead to the creation, stabilization and disappearence of moving spiral chimeras. Finally, Chapter 8 presents the main conclusions of this thesis.

1.2 Objectives

The main objective of this dissertation is to study and characterize the creation, stabilization and disappearence of propogative localized structures in nonlocal systems. To achieve this, the following specific objectives were proposed.

- Identify and understand the different physical mechanisms responsible for the propagation of localized structures.
- Classify the different types of dynamics through an extensive exploration of the parameter space.
- Develop and implement a numerical method for the continuation of complex traveling solutions in one- and two-dimensional nonlocal systems.
- Identify and characterize the bifurcations that lead to the creation, stabilization and disappearence of localized structures through the use of numerical continuation techniques.

1.3 Common abbreviations

- **LS**: Localized structures
- **DS**: Dissipative soliton
- **SHE**: Swift-Hohenberg Equation
- **LLE**: Lugiato-Lefever Equation
- **NLS**: Nonlinear Schrödinger Equation
- **KdV**: Korteweg-de Vries Equation
- **HHS**: Homogeneous Steady State
- **SRS**: Stimulated Raman Scattering

1.4 Contribution statement

1.4.1 Isolas of localized structures and Raman–Kerr frequency combs in micro-structured resonators (Chaos, Solitons & Fractals 174, 113808)

Marcel G. Clerc and Mustapha Tlidi conceptualized the study and designed the research. **Martin Bataille-Gonzalez** implemented and performed numerical simulations and continuation. Marcel G. Clerc and Mustapha Tlidi wrote the manuscript. **Martin Bataille-Gonazalez** contributed to editing and revising the manuscript.

1.4.2 Dissipative Soliton Combs with Spectral Filtering. (submitted to Physical Review A)

Marcel G. Clerc and Mustapha Tlidi conceptualized the study and designed the research. **Martin Bataille-Gonzalez**, Bilal Kostet and Youri Soupart performed research (numerical integration, implementation of numerical continuation, and analysis of numerical data). Bilal Kostet and Mustapha Tlidi developped the analytical framework. Bilal Kostet, Youri Soupart, Mustapha Tlidi and Marcel Clerc wrote the manuscript. **Martin Bataille-Gonazalez** contributed to editing and revising the manuscript.

1.4.3 Moving spiral wave chimeras (Physical Review E, 104(2), L022203)

Oleh Omel'chenko conceptualized the study and designed the research. **Martin Bataille-Gonzalez** performed research (numerical integration, and analysis of numerical data). Marcel G. Clerc supervised the research and provided critical feedback. Oleh Omel'chenko and

Marcel G. Clerc wrote the manuscript. **Martin Bataille-Gonazalez** contributed to editing and revising the manuscript.

1.4.4 Traveling spiral wave chimeras in coupled oscillator systems: emergence, dynamics, and transitions (New Journal of Physics 25, 103023)

Oleh Omel'chenko conceptualized the study and designed the research. **Martin Bataille-Gonzalez** and Oleh Omel'chenko implemented and performed numerical simulations and continuation. Marcel G. Clerc and Edgar Knobloch supervised the research and provided critical feedback. Oleh Omel'chenko and Edgar Knobloch wrote the manuscript. **Martin Bataille-Gonazalez** and Marcel G. Clerc contributed to editing and revising the manuscript.

Chapter 2

Preliminary concepts

2.1 Dynamical Systems

The general form for a dynamical system is the following.

$$\frac{d\boldsymbol{u}}{dt} = \boldsymbol{f}(\boldsymbol{u}, \eta), \qquad \boldsymbol{f} : \mathbb{R}^N \times \mathbb{R}^{n_\eta} \to \mathbb{R}^N. \tag{2.1}$$

Here, $\boldsymbol{u}$ represents the state vector of the system, it might correspond to the concentrations of different chemicals, the population of certain species or the amplitude of an electric field. The temporal evolution of the state of the system is thus determined by the vector function $\boldsymbol{f}$. This function may, in turn, depend on one or more control parameters η relevant to the modeled experiment (i.e. driving frequency, pumping power, etc.).

In this thesis, different dynamical systems in the form of Eq. (2.1) with a *nonlinear* function $\boldsymbol{f}$ will be considered. Although it might be argued that, at a fundamental level, the physical laws that describe the evolution of a system are linear (such as the Schrödinger equation), when one looks at meso- or macroscopical systems, nonlinear terms naturally arise due to the coarse-graining of the microscopical degrees of freedom [19].

In the case of a nonlinear dynamical system, it becomes extremely difficult, and often impossible, to find general explicit solutions of Eq. (2.1). But it turns out that in most cases, an in-depth description of the model can be provided by studying only the steady states ($\boldsymbol{f}(\boldsymbol{u}, \eta) = 0$) and their qualitative changes as parameters are varied. In other words, the problem can be reduced to finding the *equilibria* and *bifurcations* of the system. In the following section, the elementary bifurcations a system can experience will be described.

2.2 Bifurcations

One of the pioneers in identifying the importance of bifurcations in the study of dynamical systems was Henri Poincaré while studying the different stable configurations of a gravitating rotating fluid, along with their respective stability [20]. In doing so, he coined the term *bifurcation*, refering to the point in the parameter space at which different solutions branch off from a another solution. To this day, his definition remains valid and, more formally, corresponds to a qualitative change in the system's behavior, related to the transition between different equilibria or to the exchange of stability, as a control parameter is varied [21].

2.2.1 Saddle-Node bifurcation

Saddle-node or *fold* bifurcations provide the simplest mechanism for which a pair of stable and unstable equilibria can be created (or destroyed) as the control parameter is changed [21]. Although they arise in a huge variety of systems [22], close to the bifurcation point, the dynamics can always be reduced to the following minimal or *normal form*.

$$\frac{du}{dt} = \eta - u^2 \tag{2.2}$$

Following the notation of Eq. (2.1), u represents the state variable and η the control parameter. For $\eta > 0$, the system presents two equilibria $u_\pm = \pm\sqrt{\eta}$, where u_+ is stable and u_- unstable. An interesting case occurs when $\eta = 0$, at which point $u = 0$ is half-stable (stable for positive perturbations and unstable for negative perturbations). Lastly, for $\eta < 0$ there are no equilibria. Figure (2.1) provides a visual representation of the previous analysis.

In short, as the bifurcation parameter η is decreased (increased) starting from positive (negative) values, the two equilibria attract (repel) each other and suddenly annihilate (appear).

Example 2.2.1. For centuries, the mystery of synchronization between fireflies has captivated the scientific community, and only recently has it been partially unveiled. Although the topic is intricate and will be discussed in more detail in Section 2.4.1, we will aim to shed *light* on this topic only with the knowledge of saddle-node bifurcations and a simple model proposed by Ermentrout and Rinzel [23].

Consider the problem of a firefly flashing under the presence of a periodically flashing light. We will model the flashing of the firefly with an angular variable θ such that $\theta = 0$ represents the firefly's flash. The firefly has its own inherent frequency ω, i.e. in the absence of stimuli $\dot{\theta} = \omega$. On the other hand, the periodic stimulus will be represented by a phase ϕ that satisfies $\dot{\phi} = \Omega$, where Ω is of course the stimuli period. In order to synchronize with the stimuli, the firefly will either want to speed up if it is lagging behind or slow down if it is going too fast. The simplest non-linear model that fulfills these assumptions is the following,

$$\begin{aligned}\dot{\phi} &= \Omega,\\ \dot{\theta} &= \omega + A\sin(\phi - \theta).\end{aligned}$$

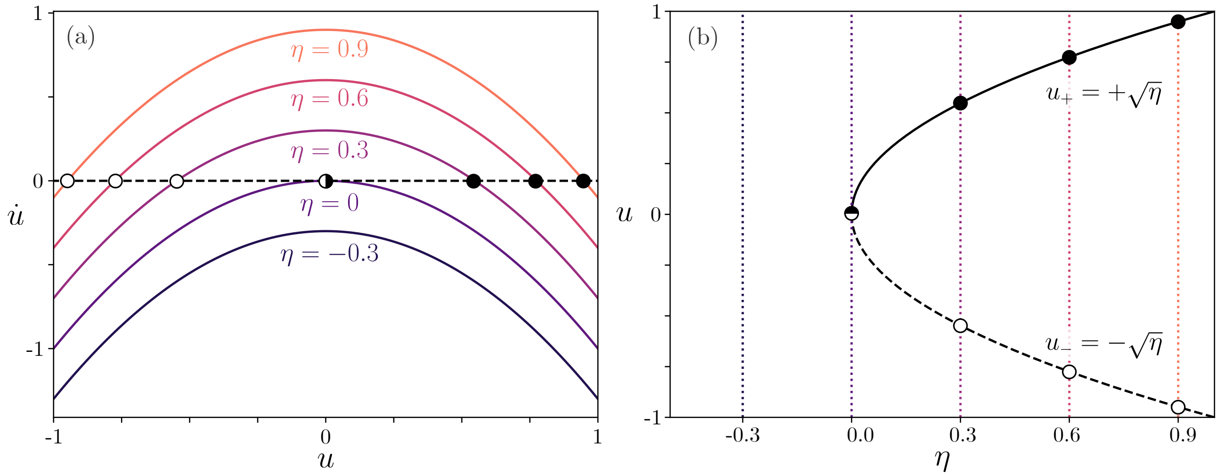

Figure 2.1: Prototipical scenario for a saddle-node bifurcation. (a) Phase space showing both stable and unstable fixed points for different values of η. Black (white) circles represent stable (unstable) fixed points. (b) Bifurcation diagram showing the creation of a stable-unstable pair of fixed points. Solid (dashed) line represents stable (unstable) branch.

Subtracting both equations and defining $\varphi = \dot{\phi} - \dot{\theta}$ yields

$$\dot{\varphi} = \Omega - \omega - A \sin \varphi,$$

which can be adimensionalized by rescaling $t \to At$ and introducing the non-dimensional parameter $\mu = (\Omega - \omega)/A$,

$$\dot{\varphi} = \mu - \sin \varphi. \tag{2.3}$$

For $\mu = 0$ where the forcing and intrinsic frequencies are the same, there is a stable fixed point at $\varphi = 0$ and an unstable fixed point at $\varphi = \pi$. As μ increases, both equilibria approach each other until they collide for $\mu = \mu_c = 1$ at $\varphi = \pi/2$ and then disappear for $\mu > 1$. We can recognize that the pair of fixed points appear (or disappear) through a saddle-node bifurcation.

Moreover, close to the bifurcation point where $\mu_c = 1$ and $\varphi_c = \pi/2$, we can do a Taylor expansion: $\mu = 1 + \eta$ and $\varphi = \pi/2 + u$ where $\eta, u \ll 1$. Using the identity $\sin \varphi = \sin(\pi/2 + u) = \cos u$ and inserting the previous ansatz into Eq. (2.3) yields the following

$$\begin{aligned} \dot{\varphi} = \dot{u} &= 1 + \eta - \cos u, \\ &\approx 1 + \eta - (1 - \frac{1}{2}u^2), \\ &= \eta - \frac{1}{2}u^2, \end{aligned}$$

which after adequate rescaling corresponds exactly with the saddle-node normal form.

2.2.2 Pitchfork bifurcation

Pitchfork bifurcations typically arise in systems with reflection symmetry and provide a universal mechanism for symmetry-breaking [21]. A simple example is given by the statistical description of magnetization. In the absence of an external field, the net magnetization m (below the critical temperature T_c) can either be positive or negative with no preferred orientation, thus depending only on the initial condition. On the other hand, if the system is heated above the critical temperature, no net magnetization is observed, i.e. $m = 0$. In the context of statistical mechanics, this second-order transition can be described by a mean-field approximation from Landau theory [19, 24], where the free energy functional is expanded in (even) powers of m, thus arriving at exactly the pitchfork normal form, given by

$$\frac{du}{dt} = \eta u - u^3. \tag{2.4}$$

As shown in Fig. (2.2), for $\eta < 0$ there is only one equilibrium of Eq. (2.4), it is stable and corresponds to the trivial solution $u = 0$. For $\eta > 0$, the trivial solution loses stability and two stable symmetric branches $u_{\pm} = \pm\sqrt{\eta}$ emerge.

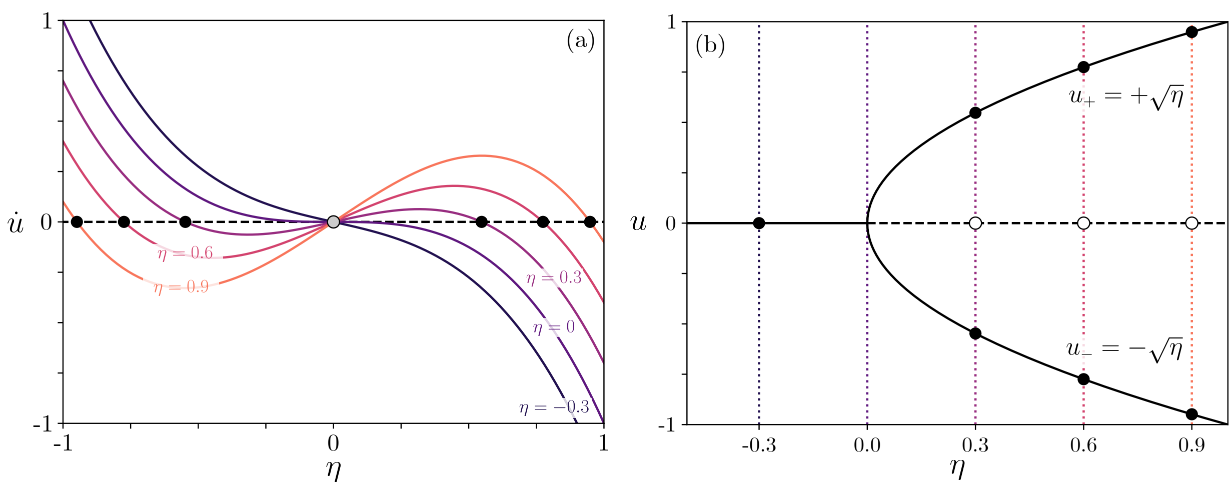

Figure 2.2: Prototipical scenario for a pitchfork bifurcation. (a) Phase space showing both stable and unstable fixed points for different values of η. Black circles represent stable fixed points, the grey circle represents a stable for $\eta < 0$ and unstable for $\eta > 0$ fixed point. (b) Bifurcation diagram showing the emergence of two stable branches at the bifurcation, along with the change of stability of the trivial solution. Solid (dashed) lines represent stable (unstable) branches.

Two types of pitchfork bifurcations should be distinguished: the *supercritical* and the *subcritical* case. The former corresponds to Eq. (2.4) and was discussed above. In the latter, the two symmetric branches that emerge at the bifurcation point are unstable. In that case, the cubic term in the normal form has a positive sign and a negative quintic term is added to ensure the solution is bounded, and thus, that is physically relevant. The modified normal form corresponds to Eq. (2.5).

$$\frac{du}{dt} = \eta u + u^3 - u^5. \tag{2.5}$$

Moreover, due to the additional quintic term, the symmetric branches are stabilized at a secondary saddle-node bifurcation point η_{sn}, as shown in Fig. 2.3. It is important to mention that in subcritical bifurcation, a hysteresis loop is typically observed.

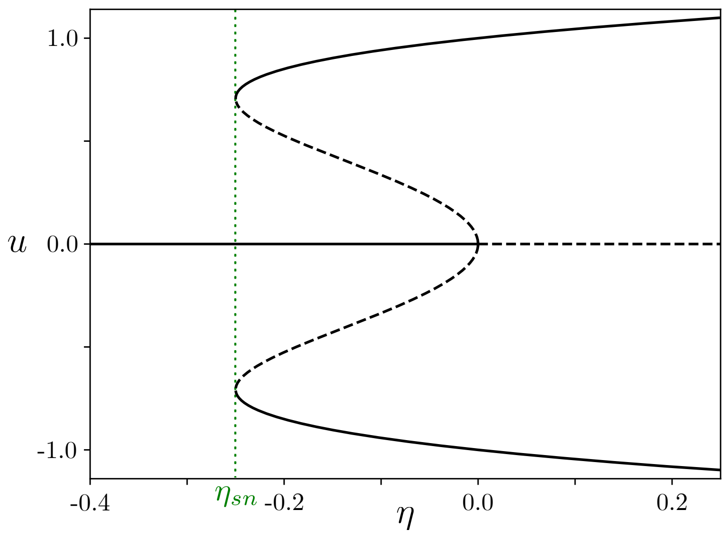

Figure 2.3: Bifurcation diagram for the subcritical pitchfork. At the bifurcation point for $\eta = 0$, two symmetric unstable branches emerge and gain stability after undergoing a saddle-node bifurcation for $\eta = \eta_{sn} = -\frac{1}{4}$. The trivial solution is stable for $\eta < 0$ and unstable for $\eta > 0$.

2.2.3 Andronov-Hopf bifurcation

The two bifurcations discussed previously describe the emergence of steady states or fixed points. More specifically, they belong to the class of *stationary* bifurcations. Here, a different class of bifurcations will be introduced, that of *dynamical* bifurcations, in which dynamical equilibria emerge. The simplest scenario is the Andronov-Hopf bifurcation that allows for the emergence of a limit cycle or, in other words, a periodic equilibrium. Since oscillations are impossible in one dimension [21], this bifurcation can only be present in systems of two or more dimensions. For simplicity, the following analysis will be restricted to only two dimensions. Nevertheless, it can easily be extended to the more general case of arbitrary dimensions. The normal form can be written in a compact form as a complex equation, Eq. (2.6), for the order parameter $A = x + iy$. It is important to mention that the coefficient accompanying the cubic term could be complex, in that case, it corresponds to the Stuart-Landau equation [25, 26] which is the homogeneous part of the widely known Complex Ginzgurg-Landau equation [27].

$$\frac{dA}{dt} = (\eta + i\omega)A - |A|^2 A. \tag{2.6}$$

It can directly be observed that there is a trivial fixed point at $A = 0$. Linear stability analysis around this fixed point reveals a pair of complex eigenvalues $\lambda_{\pm} = \eta \pm i\omega$. Therefore, for $\eta < 0$ the fixed point is a stable focus, whereas for $\eta > 0$, the eigenvalues have crossed the imaginary axis rendering the focus unstable. Moreover, by rewriting Eq. (2.6) in polar coordinates $A = re^{i\theta}$, the emergence of a limit cycle is evidenced.

$$\dot{r} = r(\eta - r^2), \tag{2.7}$$

$$\dot{\theta} = \omega. \tag{2.8}$$

From Eq. (2.8) it can be observed that a limit cycle emerges from $\eta = 0$ with frequency ω and an amplitude $|A| = r = \sqrt{\eta}$ that increases continuously from zero. Similarly, as in the pitchfork bifurcation, this case corresponds to a supercritical bifurcation given that the limit cycle arising from the bifurcation is stable. Furthermore, the two results mentioned previously apply also in general, namely, that close to the bifurcation point η_c, the amplitude of the limit cycle grows with $\sqrt{\eta - \eta_c}$ and the frequency is approximately the imaginary part of the eigenvalue at the bifurcation point: $\operatorname{Im} \lambda(\eta_c)$.

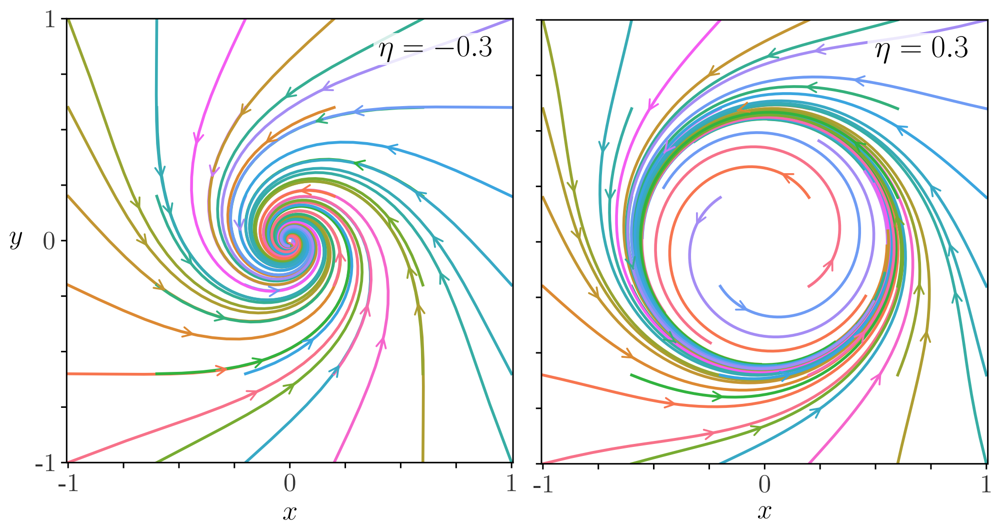

Figure 2.4: Phase plane trajectories of Eq. (2.6) showing a stable focus for $\eta = -0.3$ in the left panel and a stable limit cycle for $\eta = 0.3$ in the right panel

There is, however, a subcritical variation of the Andronov-Hopf bifurcation in which the emerging limit cycle is unstable and may stabilize at a secondary bifurcation point. The normal form is similar to the subcritical pitchfork since the cubic term has now the opposite sign and a quintic term is added to ensure the solution is bounded. Due to the additional quintic term, the emerging limit cycle stabilizes at $\eta_{sn} = -\frac{1}{4}$ through a saddle-node bifurcation.

$$\frac{dA}{dt} = (\eta + i\omega)A + |A|^2 A - |A|^4 A \tag{2.9}$$

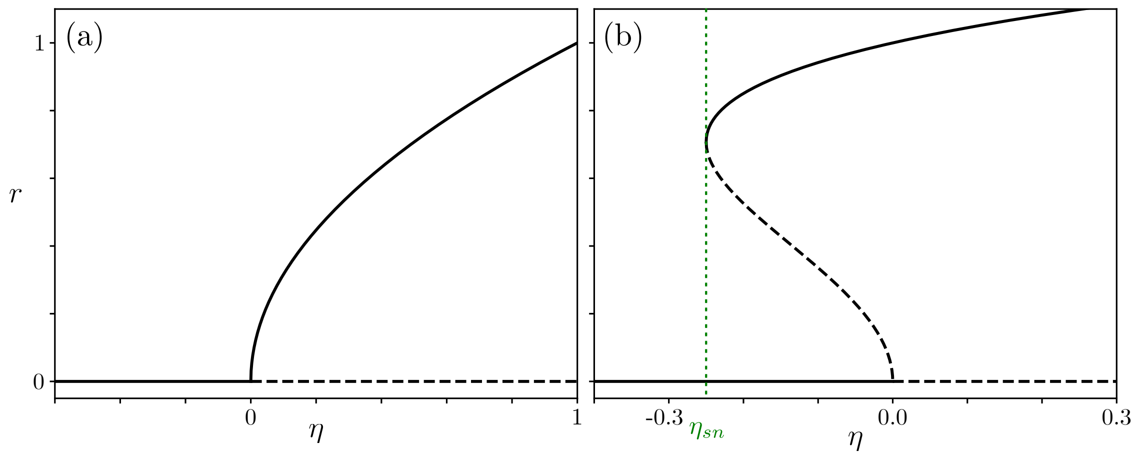

Figure 2.5: The subcritical and supercritical scenarios of the Andornov-Hopf bifurcation. Panel (a) shows the supercritical case and panel (b) shows the subcritical case.

2.3 Localized Structures

Almost a century ago, our understanding of elementary or quantum particles went through a complete change of paradigm. Indeed, what was originally thought to be a microscopic speck of matter with a well-defined position, velocity and size was discovered instead to be a localized wave function lacking the former quantities. Half a century later, this change of paradigm carried over to meso- and macroscopical out-of-equilibrium systems. Nicolis and Prigogine [4] argued that the energy transfer present in these systems allows for complex and stable structures to form, such as localized structures. These localized states or particle-like solutions are supported by a robust balance between gains and losses and have been observed in a variety of systems due to their universality.

Formally speaking, a LS corresponds to a well localized deviation of some reference background, typically a homogeneous steady state, although it might also be periodic (in space) or oscillatory (in time). As illustrated in Figure (2.6), they have been observed experimentally in one, two, and even three dimensions. Their temporal dynamics are quite rich as well, they can present uniform motion, breathing or even chaotic behavior. From a mathematical point of view, their description relies on partial differential equations or, in the case of non-local systems, integro-differential equations. At least in one spatial dimension, it is possible to think of LS as a homoclinic orbit asymptotically approaching the reference state at the boundaries and performing an excursion in the neighborhood of another equilibrium in the center. In the more general case of two and three-dimensional LSs, the picture becomes more complex but the coexistence between two distinct equilibria remains necessary for the formation of LSs.

2.3.1 Solitons

Among localized states, a particularly interesting type are solitons. They were discovered for the first time in 1834 by John Scott Russell. He described them as a *"large solitary*

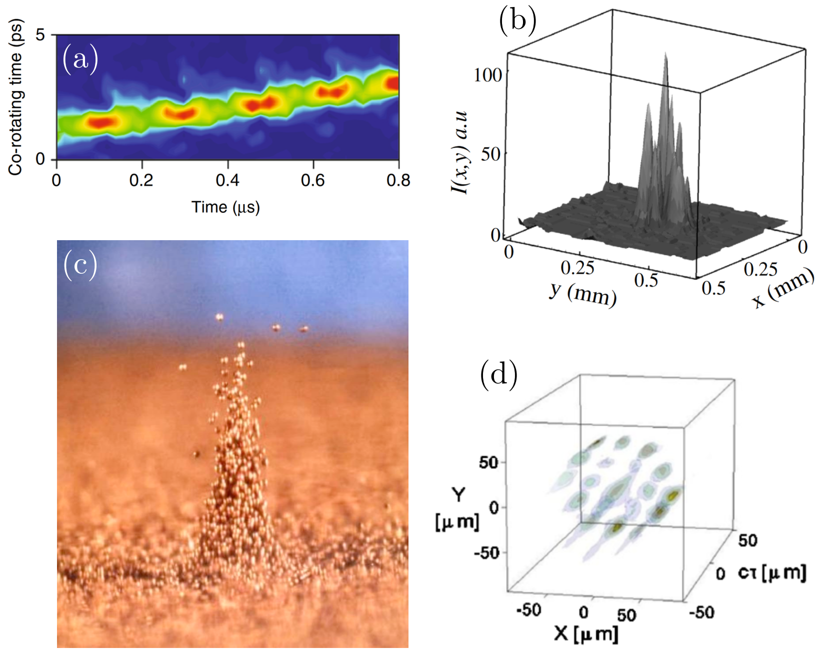

Figure 2.6: Examples of localized structures in nonlinear optics and granular media. Panels (a)-(d) show experimental observations of a drifting breather soliton in a microcavity [10], a chaoticon in a liquid crystal light valve [9], an oscillon in a vibrating layer of sand [6, 7], and a three-dimensional light bullet in a waveguide array [8].

[...] heap of water, which continued its course along the channel without change of form or diminution of speed" [28]. These solitary waves were highly controversial at the time until Korteweg and de Vries provided an integrable model for shallow water waves and proved their existence in the now called Korteweg de Vries (KdV) equation [29]. It was only a century later that the term soliton was coined by Zabusky and Kruskal to emphasize their particle-like behavior after observing that solitons in the KdV equation could pass through each other with no change in shape or speed [30]. In the following years, the newly discovered inverse scattering transform [31, 32] allowed to completely solve the KdV equation and find the analytical expression of solitons. Immediately after, it was extended to other integrable and conservative equations such as the nonlinear Schrödinger (NLS) equation [33] and the sine-Gordon equation [34]. In these systems, they arise due to a balance between dispersion and nonlinearity.

More recently, the term dissipative soliton (DS) was introduced to extend the previous definition and refers to a qualitatively similar state, but in driven dissipative systems, where there is a continuous energy influx and dissipation, requiring thus a balance between influx and dissipation. Although there is not a commonly agreed-upon definition of DSs, they typically exhibit certain features. Firstly, DSs are attractors with well-defined amplitude and shape, and possess a characteristic length independent of the system size or boundary. Moreover, they tend to interact with other nearby DSs in a manner reminiscent of classical particles. As a result, they often receive the name of particle-like states. It is important to emphasize that classical (conservative) solitons and dissipative solitons are two very different structures; the mathematics behind their presence, and therefore their properties, are distinct.

In the following sections, a more in-depth description of LSs and DSs will be presented in the context of two paradigmatic models: the Swift-Hohenberg equation and the Lugiato-Lefever equation.

2.3.2 Swift-Hohenberg equation

The Swift-Hohenberg equation (SHE) is possibly the simplest and most studied model for the formation of patterns and localized structures, see [13, 35] for a comprehensive review. It was first introduced by Swift and Hohenberg as a phenomenological model to describe Rayleigh-Bénard convection [36, 37], although it was later known that Turing had already written a similar and more general equation in the context of morphogenesis [38]. Thus, it is also refered to as the Turing-Swift-Hohenberg equation. The SHE can be written in several forms, depending on the nonlinearities. The most common presents only a cubic nonlinearity, similar to a supercritical pitchfork; while other variations with either a quadratic-cubic or cubic-quintic nonlinearities can be envisaged [13, 39]. In the former case, the pattern (spatially periodic) state emerges supercritically whereas in the latter, it emerges subcritically. Since a coexistence between the pattern and the trivial state is necessary for the formation of LSs, the subcritical case will be the focus of the following discussion, and in particular the case of the cubic-quintic SHE,

$$\partial_t u = \varepsilon u + u^3 - u^5 - \nu \nabla^2 u - \nabla^4 u, \tag{2.10}$$

where u is a real scalar field, ε is the control parameter and $\nu > 0$ can be set to one without loss of generality. It can be noted that Eq. (2.10) is reflection symmetric with respect to both the x and u axes, i.e. is invariant under transformation $x \to -x$ and $u \to -u$. Moreover, the equation is variational, meaning that it minimizes a Lyapunov (or free energy) functional $\mathcal{F}[u]$ such that,

$$\mathcal{F} = \frac{1}{2}\int_{-\infty}^{\infty} -\varepsilon u^2 - \frac{1}{2}u^4 + \frac{1}{3}u^6 - (\nabla u)^2 + (\nabla^2 u)^2 \; d^d r. \tag{2.11}$$

As a result, the solutions of Eq. (2.10) evolve into stationary states. In principle, Eq. (2.10) can be written in d spatial dimensions, however, the following discussion will be restricted to the case of $d = 1$ for simplicity. It can be observed that the SHE admits a trivial solution $u = 0$. Linear stability analysis with respect to perturbations of the form $\delta u = e^{\sigma t + ikx}$ yields the following dispersion relation for the growth rate,

$$\sigma = \varepsilon + \nu k^2 - k^4. \tag{2.12}$$

The critical mode for which patterns emerge can be obtained by setting $\sigma = 0$ in Eq. (2.12), revealing the critical wavenumber $k_c^2 = \frac{\nu}{2} \pm \sqrt{\varepsilon - \frac{\nu^2}{4}}$. From where it can be inferred that patterns emerge at a critical point $\varepsilon_c = \frac{\nu^2}{4}$ (also called Turing point, or modulational instability). For increasing values of ε, the critical mode, along with its neighboring band of modes, becomes unstable, leading to an exponential growth until it saturates due to the nonlinear terms. In consequence, patterns form with a characteristic length scale determined by k_c, provided the system is large enough to neglect boundary effects.

Furthermore, perturbation theory close to the bifurcation point [39] predicts that the pattern state emerges subcritically, along with four branches of localized states parametrized by their phase $\phi = 0, \pi/2, \pi, 3\pi/2$. These four branches come in even ($\phi = 0, \pi$) and odd ($\phi = \pi/2, 3\pi/2$) pairs. Each pair of branches is related by a reflection symmetry $u \to -u$, and thus, share the same norm. By means of numerical continuation (see Chapter 3 for a detailed explanation), the solution branches far from the bifurcation point can be followed, revealing the bifurcation diagram shown in Fig. 2.7.

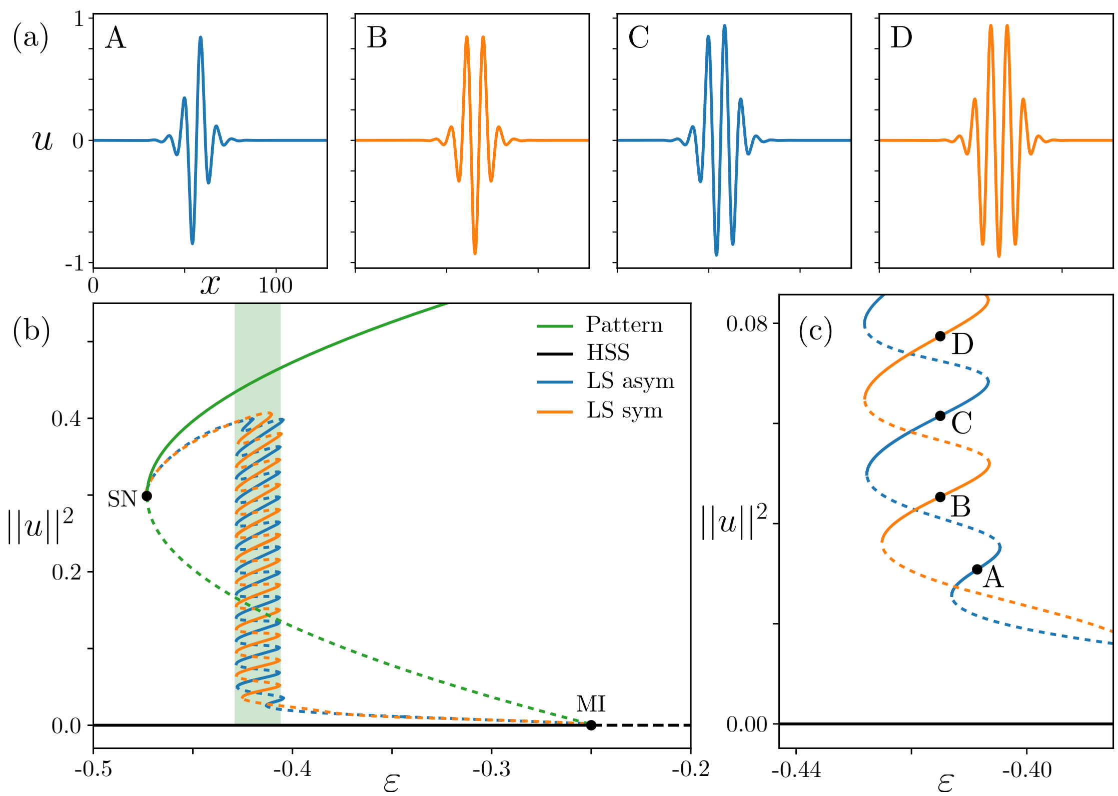

Figure 2.7: Homoclinic snaking of LSs in the cubic-quintic SHE, Eq. (2.10). Panels (a) show the spatial profile of the first two odd and even LSs. Panel (b) corresponds to the bifurcation diagram showing the two pairs of symmetric (blue) and asymmetric (orange) LSs, along with the homogeneous steady state (black) and the pattern state (green). The snaking or pinning region is shaded in green. Solid (dashed) lines represent stable (unstable) branches. A zoom of the snaking region is shown in panel (c).

An intriguing feature of Eq. (2.10) is the snaking behavior of the branches of LSs, as shown in Fig. 2.7. Indeed, it can be observed that a new wavelength is added to the LSs after it undergoes a pair of saddle-node bifurcations. On a finite domain, this behavior continues until no more wavelengths can be added, at which point the branches of LSs connect to the pattern state at its saddle-node bifurcation point. This so-called homoclinic snaking is a consequence of the heteroclinic tangle between the stable and unstable manifolds of the HSS and pattern state, respectively [12, 40]. Indeed, as the control parameter varies and enters the snaking region, both manifolds start to intersect each other, tangentially at first, and then transversally [13]. It is due to these intersections that homoclinic orbits connecting the HSS and the pattern state (i.e. LSs) are formed.

The snaking bifurcation scenario discussed previously is not exclusive to the SHE. On the contrary, it has been observed in a wide variety of systems, albeit with some qualitative differences. For instance, in the case of conservative or non-local systems, it has been found that the snaking may become slanted or tilted [41–43]. Nevertheless, the underlying picture remains the same, provided that the system is spatially reversible and manifolds intersect transversally [13].

2.3.3 Resonant cavities and the Lugiato-Lefever equation

In the preceeding section, the main ingredients and phenomenology of LSs have been discussed in a simple yet universal model. In this section, the discussion will be continued in a more complex and realistic system, arising in nonlinear optical resonators. Indeed, in an effort to provide a minimal model for the formation of patterns and dissipative structures in the context of optics, Lugiato and Lefever derived a damped driven nonlinear Schrödinger equation in [44] to describe resonant cavities under idealized conditions. Although this equation had been reported earlier in the context of condensate [45] and plasma physics [46], Lugiato and Lefever were pioneers in its application to optics, hence it is now known as the Lugiato-Lefever equation (LLE), at least in this context.

In recent years, the idealized conditions assumed by the authors have been fulfilled particularly well in driven microresonator systems, as shown by the excelent agreement between experiments and simulations of the LLE [47]. Moreover, these microresonators systems have become essential for the generation of broadband frequency combs, corresponding to equally spaced spectral lines, with applications in numerous fields [48–50]. The generation of frequency combs has been found to be intamately related to the formation of LSs inside the resonator [51–53]. As a result, the LLE has become a fundamental model for the study of dissipative structures in optics, both because of its simplicity and its accuracy in describing the dynamics of driven resonators.

In non-dimensional form, the longitudinal LLE can be written as follows,

$$\partial_t E = E_0 - (1 + i\theta)E + i|E|^2 E + i\beta\partial_\tau^2 E, \tag{2.13}$$

where $E(t, \tau)$ is the complex electric field envelope, t represents the slow time (over many roundtrips) and τ the fast time in the moving frame of reference (along the cavity roundtrip), E_0 is the normalized pump power, θ is the normalized detuning from the cavity resonance, and β is the normalized dispersion. Depending on the sign of the dispersion, two regimes can be distinguised: the normal dispersion regime ($\beta = -1$) and the anomalous dispersion regime ($\beta = 1$). The two cases support different types of LSs, with the former presenting dark solitons and the latter bright solitons. The following analysis will be restricted to the anomalous dispersion regime, as it is the most relevant for subsequent chapters.

The homogeneous steady states (HSS) of Eq. (2.13) can be found by setting $\partial_t E = \partial_\tau^2 E = 0$, and taking the modulus squared of the equation, yielding the following cubic equation for the intracavity amplitude $I = |E|^2$, in terms of the pump amplitude $I_0 = |E_0|^2$,

$$I^3 - 2\theta I^2 + (1+\theta^2)I - I_0 = 0. \tag{2.14}$$

For $\theta < \sqrt{3}$, Eq. (2.14) has only one real root, in which case the system is monostable; whereas for $\theta > \sqrt{3}$, three real roots are present, and the systems is said to be bistable. In the latter case, the transition between the three distinct HSS occurs via two saddle-node bifurcations, located at

$$I_{sn}^{\pm} = \frac{1}{3}\left(2\theta \pm \sqrt{\theta^2 - 3}\right). \tag{2.15}$$

Moreover, linear stability analysis with respect to perturbations of the form $e^{\sigma t + i\kappa\tau}$ predicts a modulational instability at $I = 1$ for $\theta < 2$. On the other hand, for $\theta > 2$, the modulational instability occurs at the lower saddle-node bifurcation point I_{sn}^{-}.

2.3.4 Spontaneous symmetry breaking and motion instabilities

In the preceeding sections, the formation of localized structures and dissipative solitons has been discussed in the context of two paradigmatic models. Yet, their dynamics, which is an integral part of this dissertation, has eluded the discussion. In this section, the focus will be placed on uniformly moving LSs and, in particular, on the mechanisms that drive their motion.

The appearance of moving LSs is associated with the breaking of reflection symmetry. Two distinct mechanisms responsible for this symmetry breaking can be identified: forced (or external) and spontaneous (or internal). The former has been widely observed and corresponds to the case where the LS is driven by an external perturbation, such as a phase gradient [54], a space-delayed feedback [55], or nonreciprocal coupling [56]. A typical feature in these systems is that the LSs move in a direction determined by the symmetry-breaking perturbation, since there is a preferred direction. The latter, on the other hand, is less frequent and arises in isotropic and nonvariational systems, where an asymmetric mode becomes unstable through an internal instability [57], thus leading to the propagation of LSs. This transition from motionless to traveling solutions is also known as an out-of-equilibrium Ising-Bloch transition [57–61]. In these cases the LSs may move in more than one direction, which will be determined by the initial condition.

2.4 Phase oscillators and Chimera states

Previously, the self-organization of extended systems into localized patterns has been exposed in a variety of contexts. In this section, the focus will be diverted to a different kind of collective behavior in coupled oscillators systems. In particular, it will be shown that these interacting oscillators may, under certain conditions, synchronize or even form unexpected synchrony patterns known as chimera states. The presentation and definition of such states will be delayed to the end of the present section, after the introducing the concept of phase oscillators and their description through the Kuramoto model.

For several centuries, the synchronization of oscillators has intrigued scientists of a number of disciplines. The first recorded observation of synchronization dates back to 1665, when Christiaan Huygens observed that two pendulum clocks mounted on the same beam synchronized their motion after some time [62]. Only a few years later, in 1680, Engelbert Kaempfer reported the same phenomenum in a population of glowworms in Siam [63]. Since then, synchronization has been reported in populations of fireflies [64], pacemaker cells [65], laser arrays [66], Josephson junctions [67], to name a few.

Through the examples mentioned above, it is clear that synchronization is a universal and robust phenomenon which does not depend on the particular laws governing each system. Consequently, its mathematical description should be kept as abstract and universal as possible. Then what could be the common feature of all these oscillators, that could serve as a starting point for a universal description? They are all coupled *self-sustained oscillators*, i.e. active units that, isolated from the rest, would oscillate indefinitely with their own rythm. As it will be explained in the following section, the dynamics of these oscillators–despite their diversity–can be reduced to a single universal quantity: their phase.

2.4.1 Phase oscillators

Consider a self-sustained oscillator with a natural frequency ω, described by the following system of M ordinary differential equations,

$$\frac{d\mathbf{x}}{dt} = \mathbf{f}(\mathbf{x}), \qquad \mathbf{x} \in \mathbb{R}^M. \tag{2.16}$$

In phase space, the oscillation can be represented by a stable limit cycle, i.e. a closed isolated attractrive trajectory. Due to its attractive nature, trajectories in the vicinity of the limit cycle, or more specifically, in its bassin of attraction, will eventually converge to it. Therefore, under the assumption of weak perturbation or coupling, the trajectory of the oscillator will only slightly deviate from the limit cycle, and rapidly return to it. Hence, the dynamics of the oscillator's amplitude can be neglected since it will remain close to that of the limit cycle. Only one variable remains relevant: the *phase* of the oscillator.

The asymptotic phase θ, or phase for short, is defined as a monotonically and uniformly increasing variable in time that wraps around the limit cycle, this is to say, it grows uniformly from 0 to 2π in one period T. In other words, the phase obeys the following relation,

$$\frac{d\theta}{dt} = \omega. \tag{2.17}$$

Moreover, the definition of the phase can be extended to the whole basin of attraction of the limit cycle, by assigning the same phase to all points which eventually converge (in the absence of perturbation) to the same point in the limit cycle. The set of points with the identical phase is called an *isochron*.

With the phase defined, a relation between the phase and the state $\mathbf{x}$ of the oscillator can be established through,

$$\frac{d\theta(\mathbf{x})}{dt} = \nabla_{\mathbf{x}}\theta \cdot \frac{d\mathbf{x}}{dt},$$

where $\nabla_{\mathbf{x}}\theta$ is the gradient of the phase with respect to $\mathbf{x}$. Combining Eqs. (2.16) and (2.17), the above equation takes the form,

$$\nabla_{\mathbf{x}}\theta \cdot \mathbf{f}(\mathbf{x}) = \omega. \tag{2.18}$$

At this stage, the phase may not seem to be a particularly useful quantity. However, in the following scenario, a glimpse of its power will be appreciated.

2.4.2 Mutual synchronization and the Adler equation

Consider the case of two weakly coupled oscillators with natural frequencies ω_1 and ω_2, described by

$$\frac{d\mathbf{x}_1}{dt} = \mathbf{f}_1(\mathbf{x}_1) + \varepsilon\mathbf{p}_1(\mathbf{x}_1, \mathbf{x}_2), \tag{2.19}$$

$$\frac{d\mathbf{x}_2}{dt} = \mathbf{f}_2(\mathbf{x}_2) + \varepsilon\mathbf{p}_2(\mathbf{x}_2, \mathbf{x}_1), \tag{2.20}$$

where ε is the (small) coupling strength and $\mathbf{p}_1$, $\mathbf{p}_2$ are the interaction terms. As previously mentioned, the weak coupling will only slightly perturb the trajectory of the oscillators from their limit cycles. Hence, the phases can still be defined in the vicinity of the limit cycles. Furthemore, there will be a small correction to Eq. (2.17) due to the coupling, which can be written as

$$\begin{aligned}\frac{d\theta_1}{dt} &= \nabla_{\mathbf{x}_1}\theta_1 \cdot \frac{d\mathbf{x}_1}{dt}, \\ &= \nabla_{\mathbf{x}_1}\theta_1 \cdot (\mathbf{f}_1(\mathbf{x}_1) + \varepsilon\mathbf{p}_1(\mathbf{x}_1, \mathbf{x}_2)), \\ &= \omega_1 + \varepsilon\nabla_{\mathbf{x}_1}\theta_1 \cdot \mathbf{p}_1(\mathbf{x}_1, \mathbf{x}_2), \end{aligned} \tag{2.21}$$

and similarly for the second oscillator. The second term in the right hand side is small, and thus, deviations of $\mathbf{x}_1$ to its limit cycle can be neglected. As a result, $\mathbf{p}_1(\mathbf{x}_1, \mathbf{x}_2)$ can be directly evaluated at the limit cycle. The benefit of this approximation is that, at the limit cycle, there is an invertible mapping between θ_1 and $\mathbf{x}_1$, and thus, the dependence on $\mathbf{x}_{1,2}$ can be replaced by a dependence on $\theta_{1,2}$. This allows to write the phase equations in closed form,

$$\frac{d\theta_1}{dt} = \omega_1 + \varepsilon q_1(\theta_1, \theta_2), \tag{2.22}$$
$$\frac{d\theta_2}{dt} = \omega_2 + \varepsilon q_2(\theta_2, \theta_1). \tag{2.23}$$

The above equations are much simpler in form than the original system. This, however, comes at a cost: the functions $q_{1,2}$ are not known, and their determination is not straightforward. Nevertheless, it is possible to make some reasonable approximations to derive a simple expression for these functions. For instance, consider the case of nearly identical oscillators, i.e. $\omega_1 \approx \omega_2$, with $\delta = \omega_1 - \omega_2$ is the frequency detuning, which can be considered positive without loss of generality. Expanding the interaction terms as a double Fourier series in $\theta_{1,2}$ yields the following expression for $q_{1,2}$,

$$q_1(\theta_1, \theta_2) = \sum_{k,l} a_{k,l} e^{i(k\theta_1 + l\theta_2)},$$
$$q_2(\theta_2, \theta_1) = \sum_{k,l} b_{k,l} e^{i(k\theta_1 + l\theta_2)}.$$

At order zero, the phases evolve independently of each other: $\theta_{1,2} = \omega_{1,2} t$. Thus, by substituting in the above equations, it is possible to observe slow and fast varying terms. The fast oscillations can be averaged out, leaving only the slow rotations that satisfy the resonance condition: $k\omega_1 + l\omega_2 \approx 0$. Since the frequencies are nearly identical, this condition is satisfied for $l = -k$, and the averaged Fourier expansions become,

$$q_1(\theta_1, \theta_2) = \sum_{k} a_{k,-k} e^{ik(\theta_1 - \theta_2)},$$
$$q_2(\theta_2, \theta_1) = \sum_{k} b_{k,-k} e^{ik(\theta_2 - \theta_1)}.$$

It can be noted that the coupling term now depends only on the phase difference $\psi = \theta_1 - \theta_2$. Exploiting this fact, the equation for ψ can be written in closed form as,

$$\frac{d\psi}{dt} = \delta + \varepsilon q(\psi), \tag{2.24}$$

where $q(\psi) \equiv q_1(\psi) - q_2(-\psi)$. In the case of reciprocal coupling $q_1(\psi) = q_2(\psi)$, q becomes an odd function. The simplest choice for a 2π-periodic odd function is, of course, the sine function $q(\psi) = \sin(\psi)$. Replacing this function in Eq. (2.24) gives the Adler equation [68],

$$\frac{d\psi}{dt} = \delta + \varepsilon \sin(\psi). \tag{2.25}$$

Notably, the Adler equation predicts the emergence of mutual synchronization through a saddle-node bifurcation at $\delta = |\varepsilon|$. More specifically, for $\delta < |\varepsilon|$ and $\varepsilon < 0$ ($\varepsilon > 0$) there exists a stable (unstable) fixed point at $\psi_- = -\arcsin(\delta/\varepsilon)$ and an unstable (stable) fixed point at $\psi_+ = \pi + \arcsin(\delta/\varepsilon)$. In other words, if the detuning is small enough (relative to the coupling strength), then the oscillators will synchronize with a non vanishing phase difference, in which case they are said to be *phase locked*. Moreover, depending on the sign of the coupling strength, two cases can be distinguished. If $\varepsilon < 0$, the phase difference lies around zero and the oscillators try to synchronize in phase, in such case the coupling is said to be attractive. On the contrary, if $\varepsilon > 0$, the phase difference lies around π and the oscillators try to synchronize in anti-phase, and thus the coupling is repulsive, corresponding to Huygens' original observation.

2.4.3 Kuramoto model

Previously, the emergence of synchronization was shown in a system of two coupled oscillators. However, in nature, synchronization is more frequently observed in large populations of oscillators. In such case, an extension of the Adler equation to a system of N oscillators is necessary. Intuitively, and as a first approximation, the coupling between the oscillators can be assumed to be global (or all-to-all), and equally strong for all pairs of oscillators. This is the essence of the Kuramoto model [69, 70],

$$\frac{d\theta_i}{dt} = \omega_i + \frac{K}{N}\sum_{j=1}^{N}\sin(\theta_j - \theta_i), \tag{2.26}$$

where θ_i is the phase of the i-th oscillator, ω_i its natural frequency, and K the coupling strength. It is noteworthy to mention that the natural frequencies are not necesarrily identical. In fact, they are tipically drawn from a unimodal symmetric distribution, such as a Lorentzian or Gaussian distribution. The above equation can be manipulated into a simpler form by introducing the Kuramoto order paramater defined as follows,

$$re^{i\psi} = \frac{1}{N}\sum_{j=1}^{N} e^{i\theta_j}. \tag{2.27}$$

Through the above definition, it can be infered that r is a mesure of the degree of synchronization of oscillators. More specifically, $r = 0$ represents a completely incoherent state, where the phases are uniformly distributed on the circle. On the other hand, $r = 1$ corresponds to a completely coherent state with identical phases. In addition, the phase ψ represents the average phase of the population.

Note that the Kuramoto model, Eq. (2.26), can be rewritten in terms of the order parameter as,

$$\begin{aligned}\frac{d\theta_i}{dt} &= \omega_i + \mathrm{Im}\left(\frac{K}{N}\sum_{j=1}^{N} e^{i(\theta_j-\theta_i)}\right), \\ &= \omega_i + K\ \mathrm{Im}\left(re^{i(\psi-\theta_i)}\right), \\ &= \omega_i + Kr\sin(\psi-\theta_i). \end{aligned} \tag{2.28}$$

In this form, the oscillators seem to be effectively decoupled from each other, and coupled only to the mean field quantities r and ψ. Of course, this is only in appearance, since the coupling between pairs of oscillators remains, though it is mediated by the order parameter. In fact, the strength of the coupling with the mean field is proportional to the degree of synchrony r. Consequently, the more synchronized the population is, the stronger the coupling to the mean field becomes, and thus, even more oscillators are encouraged to synchronize, which in turn increases the coupling strength. This positive feedback loop is the mechanism underlying spontaneous synchronization. For the feedback loop to exist, it can be expected that a critical coupling strength K_c must be reached. Otherwise, the coupling would be too weak to overcome the dispersion of the oscillator's natural frequencies, and synchronization would not be possible.

The previous analysis can be made quantitative in the limit of infinitely many oscillators, $N \to \infty$, by considering the contribution of the synchronous and asynchronous oscillators to the mean field, in terms of the mean field itself. The resulting relation is a self-consistency equation which can be solved analytically in the case of a Lorentzian distribution,

$$g(\omega) = \frac{\gamma}{\pi(\omega^2+\gamma^2)}, \tag{2.29}$$

where γ is the width of the distribution. The solution of the self-consistency equation predicts a critical coupling strength $K_c = 2\gamma$ for the onset of synchronization. For coupling strengths slightly larger than the critical value K_c, the order parameter r grows continuously from zero following a square root law,

$$r = \sqrt{1-\frac{K_c}{K}},$$

revealing partially synchronized states that asymptotically approach the fully synchronized state as $K \to \infty$.

As we have seen, despite the simplicity of the Kuramoto model, it is extremely succesful in describing the transition to synchronization in large populations of oscillators. Furthermore, it can be easily tweaked to describe more complex scenarios in a variety of ways. For instance, extensive studies have been carried out of different coupling topologies, both in the context of networks, where the coupling strength becomes an adjacency matrix [71], and in the context of spatially extended systems, where the coupling essentially becomes a convolution kernel [72]. Additionally, more intricate coupling terms can be envisaged, with higher harmonics [73], or even going beyond pairwise interactions and include many-body interactions [74]. Among these countless extensions, Kuramoto and Battogtokh experimented with the combined use of a non-local coupling kernel, and the inclusion of a phase lag in the coupling term [75]. Surprisingly, they stumbled upon a new kind of synchrony pattern, which later became known as a chimera state.

2.4.4 Chimera states

The traditional Kuramoto model for non-identical oscillators predicts the existence of either incoherent or partially coherent states, depending on the coupling strength. It turns out that the addition of a phase lag in the coupling term (somewhat similar to a time delay), along with a non-local coupling kernel, can lead to the emergence of an intermediate equilibrium state, where the population splits into a coherent and an incoherent domain that coexist in space. Unexpectedly, this state can form even if the oscillators are completely identical! In such case, despite the homogeneity of the system, the oscillators spontaneously break the symmetry and self-organize into two distinct groups. This remarkable state was first reported by Kuramoto and Battogtokh [75], and later named chimera state by Abrams and Strogatz [76].

Ever since their discovery two decades ago, chimera states have been observed in a wide variety of systems and have been the subject of intense research. Specifically, they have been theoretically predicted in one-, two-, and three-dimensional spatially extended systems, in arbitrary networks, and even in more realistic systems beyond the Kuramoto model, see [72, 77–81] for comprehensive reviews. Experimental observations, although much less abundant than theoretical studies, have proved that chimeras are not just a mathematical curiosity or *chimera* (in the literary sense of a thing which is hoped for but impossible to achieve), but a real phenomenon observed in optical [82], chemical [83–85] and mechanical system [86], among others [87–89].

Chapter 3

Numerical Continuation

In the previous chapter, we mentioned the importance of finding and following the solution branches as they experience several bifurcations. There, we considered simple models where this information could be obtained analytically. However, in the problems considered in this dissertation, and in general, it is not usually possible to do so. Therefore, we must resort to numerical methods, more specifically, *numerical continuation* algorithms [90]. This type of methods aim to solve a nonlinear equation or, more generally, a system of nonlinear equations to find the desired steady states of a dynamical system as parameters are changed. This task corresponds to finding the roots (zeros) of a vector function $\boldsymbol{F}$, as in Eq. (3.1).

$$0 = \boldsymbol{F}(\boldsymbol{u}, \eta) \tag{3.1}$$

Although there are several methods for finding the roots of a vector function, in this thesis we will only use Newton-Raphson's method because of its fast (quadratic) convergence and simplicity. This method corresponds to an iterative algorithm that, given an initial guess $\boldsymbol{u_0}$, will perform successive iterations until a certain accuracy or tolerance is reached. Each iteration is computed using Eqs (3.2-3.3), where $\mathbf{J}(\boldsymbol{u}_i, \eta)$ is the Jacobian of $\boldsymbol{F}$ in Eq. (3.1). Moreover, since the Jacobian is computed at every point, the stability of the solution and the location of bifurcation points can be determined by tracking the sign of the determinant of the Jacobian.

$$\mathbf{J}(\boldsymbol{u}_i, \eta)\Delta\boldsymbol{u}_{i+1} = -\boldsymbol{F}(\boldsymbol{u}_i, \eta) \tag{3.2}$$

$$\boldsymbol{u}_{i+1} = \boldsymbol{u}_i + \Delta\boldsymbol{u}_{i+1} \tag{3.3}$$

3.1 Natural parameter continuation

The simplest way to perform numerical continuation is to fix the value of the parameter, in this case η, and solve the equation (or system of equations) by means of Newton's method. Then, one can increase the parameter by a small step $\eta = \eta_0 + \Delta\eta$ and find the new solution using the previous solution $\boldsymbol{u_0}$ as initial guess for Newton's method. The process is repeated until the whole solution branch has been computed. This method is usually called *Natural Parameter Continuation* [91].

Example 3.1.1. To illustrate the method, consider the normal form of the *imperfect pitchfork bifurcation*. Depending on the context, this model could describe magnetization under an external electric field or even optical bistability [21]. We will keep $\varepsilon > 0$ fixed and find both the stable and unstable solution branches as η is varied.

$$\dot{u} = \eta + \varepsilon u - u^3 \tag{3.4}$$

This task corresponds to finding the roots of a cubic polynomial: $F(u, \eta) = \eta + \varepsilon u - u^3 = 0$. The derivative can be determined easily: $J(u, \eta) = \varepsilon - 3u^2$. Starting the algorithm at $\eta = -0.02$ with the initial guess $u_0 = -0.4$ and moving forward (increasing η) yields the orange triangles shown in Fig. 3.1. Similarly, repeating the process backward (decreasing η) gives the green triangles shown in the same figure.

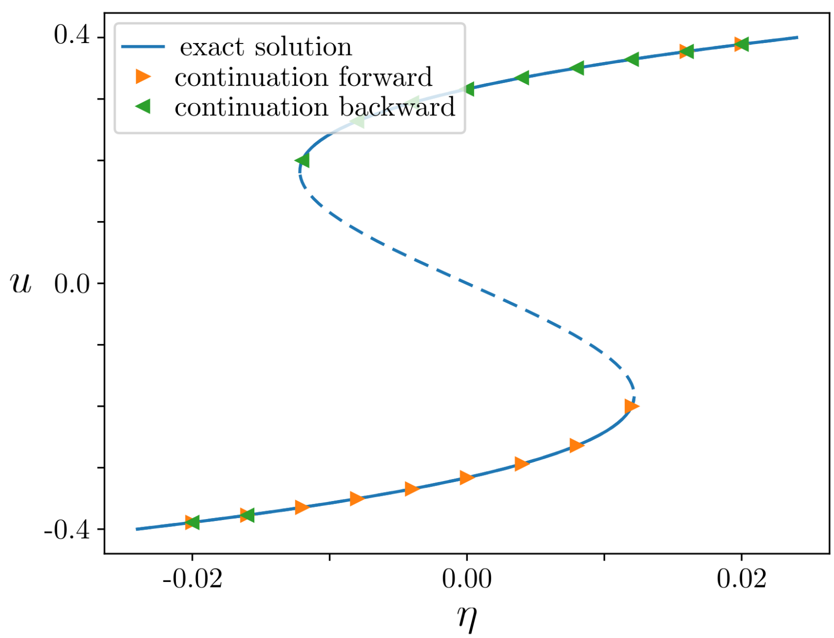

Figure 3.1: Solution of Eq. (3.4) as a function of the parameter η obtained through natural continuation (orange and green triangles) compared to the exact solution (blue curve) with $\varepsilon = 0.1$.

Note that in the example, the natural continuation succeeds at finding the lower and upper solution branches. However, it could not follow the branch past the fold (or saddle-node) bifurcation. The only way to access the middle branch using this algorithm would be to use an adequate initial guess close to the middle branch. Although in this case, it is not difficult to find a good guess, for a higher-dimensional system where the bifurcation scenario is more complicated, this quickly becomes impractical. To overcome this limitation, one can implement a more robust continuation scheme: the *pseudo-arclength continuation* [92].

3.2 Pseudo-arclength continuation

As shown in the previous example, η is not necessarily a good parameter to describe the solution curve, as it does not follow the branch through folds. A different approach can be taken where the solution branch is parametrized by a different variable: s, which is somewhat similar to the arc-length. Therefore, our goal is to obtain a set of points $\boldsymbol{y}(s) = (\boldsymbol{u}(s), \eta(s))$. The *pseudo-arclength* algorithm [92] achieves this goal through essentially two steps.

1. *Predictor step.* Extrapolate a distance Δs along the tangent $\boldsymbol{\tau}_0$ from a previously known point $(\boldsymbol{u}_0, \eta_0)$ in the $(\boldsymbol{u}, \eta)$ space, to obtain the predicted point (the point used as initial guess).
$$\boldsymbol{y} = \boldsymbol{y}_0 + \boldsymbol{\tau}_0 \Delta s$$
2. *Corrector step.* Force the solution to stay at a distance Δs in the plane perpendicular to the tangent. Or, equivalently, that the solution projected onto the tangent has length Δs.
$$(\boldsymbol{y} - \boldsymbol{y_0}) \cdot \boldsymbol{\tau}_0 = \Delta s$$

In these steps, a new object has been introduced: the tangent $\boldsymbol{\tau}$ of the solution curve $\boldsymbol{y}(s)$ which is defined as follows.

$$\boldsymbol{\tau} = \frac{d}{ds}\boldsymbol{y} = \left(\frac{d\boldsymbol{u}}{ds}, \frac{d\eta}{ds}\right) \tag{3.5}$$

An additional step must therefore be carried out to implement this method: computing the tangent vector at each point. To do this, it is convenient to revisit Eq. (3.1) and write out the dependence on the new parameter s explicitly.

$$0 = \boldsymbol{F}(\boldsymbol{u}(s), \eta(s)) \tag{3.6}$$

Taking the derivative with respect to s on both sides of the previous equation yields

$$0 = \mathbf{J}(\boldsymbol{u}(s), \eta(s))\frac{d\boldsymbol{u}}{ds} + \boldsymbol{F}_{\boldsymbol{\eta}}(\boldsymbol{u}(s), \eta(s))\frac{d\eta}{ds} \tag{3.7}$$

Note that Eq. (3.7) does not provide a unique solution for the tangent vector. Consequently, another equation must be added by restricting the length of the vector, more specifically, to normalize it.

$$\left|\left|\frac{d\boldsymbol{u}}{ds}\right|\right|^2 + \left(\frac{d\eta}{ds}\right)^2 = 1 \tag{3.8}$$

Without loss of generality, one can fix the value of $\frac{d\eta}{ds} = 1$, solve Eq. (3.7) for $\frac{d}{ds}\boldsymbol{u}$ and then normalize the obtained vector τ. Since Eq. (3.7) is just a system of linear equations, it can be solved using a standard linear solver. It is important to mention that the sign of τ must be chosen such that it has the same orientation as the previously known tangent $\boldsymbol{\tau}_0$ i.e. such that $\boldsymbol{\tau}\cdot\boldsymbol{\tau}_0 > 0$. In the very first step of the continuation method, the previous tangent is unkown. In that case, one can choose the orientation of $\boldsymbol{\tau}$ such that its last element (corresponding to $\frac{d\eta}{ds}$) is positive to move forward (increasing η) or negative to move backward (decreasing η).

To simplify the notation, it is convenient to define an extended vector function $\tilde{\boldsymbol{F}}$ that incorporates $\boldsymbol{F}$ and the corrector step in the following manner,

$$\tilde{\boldsymbol{F}}(\boldsymbol{y}) = \begin{pmatrix} \boldsymbol{F}(\boldsymbol{y}) \\ (\boldsymbol{y}-\boldsymbol{y}_0)\cdot\boldsymbol{\tau}_0 - \Delta s \end{pmatrix}. \tag{3.9}$$

The corresponding extended Jacobian $\tilde{\mathbf{J}}$ becomes

$$\tilde{\mathbf{J}} = \begin{pmatrix} \mathbf{J} & \boldsymbol{F}_\eta \\ \dfrac{d\boldsymbol{u}}{ds} & \dfrac{d\eta}{ds} \end{pmatrix}. \tag{3.10}$$

Notice that the last row of the extended Jacobian $\tilde{\mathbf{J}}$ corresponds exactly to the tangent vector $\boldsymbol{\tau}$.

The pseudo-arclength continuation algorithm can be summarized in the following steps.

0. Compute a first point in the solution branch $\boldsymbol{y}_0 = (\boldsymbol{u}_0, \eta_0)$, typically through direct numerical simulations. Additionally, one could run Newton's method once while keeping the parameter fixed at $\eta = \eta_0$ to obtain a more accurate approximation for $\boldsymbol{u}_0$.
1. Solve Eq. (3.7) and find the tangent at that point $\boldsymbol{\tau}_0$. Choose the orientation of $\boldsymbol{\tau}_0$ such that it points in the desired direction on the η-axis.
2. Using $\boldsymbol{y}_0 + \boldsymbol{\tau}_0\Delta s$ as initial guess in Newton's method, solve Eq. (3.9) to find the next point in the solution branch $\boldsymbol{y}_{i+1}$.
3. Again, solve Eq. (3.7) and find the tangent at that point $\boldsymbol{\tau}_{i+1}$. Choose the orientation such that it matches the previous tangent, $\boldsymbol{\tau}_{i+1}\cdot\boldsymbol{\tau}_i > 0$.
4. Repeat steps 3-4 until the whole solution branch has been computed. One could also track changes in the sign of the determinant of $\mathbf{J}$ in order to estimate the location of bifurcation points.

Example 3.2.1. To illustrate the method, it is useful to revisit the previous example and implement the pseudo-arclength continuation to the same problem. The extended function $\tilde{\boldsymbol{F}}(u,\eta)$ can be written in the following form,

$$\tilde{\boldsymbol{F}}(u,\eta) = \begin{pmatrix} \eta + \varepsilon u - u^3 \\ (u-u_0)\dfrac{du}{ds} + (\eta-\eta_0)\dfrac{d\eta}{ds} - \Delta s \end{pmatrix}. \tag{3.11}$$

Therefore, the extended Jacobian $\tilde{\mathbf{J}}$ reads,

$$\tilde{\mathbf{J}} = \begin{pmatrix} \varepsilon - 3u^2 & 1 \\ \dfrac{du}{ds} & \dfrac{d\eta}{ds} \end{pmatrix}.$$

The tangent vector $\boldsymbol{\tau} = (\tau_u, \tau_\eta)$ can be computed by solving Eq. (3.7). We start by fixing $\frac{d}{ds}\eta = 1$, then $\frac{d}{ds}u$ can be obtained directly,

$$\frac{du}{ds} = -\frac{F_\eta}{J} = -\frac{1}{\varepsilon - 3u^2}.$$

Finally, we normalize $\boldsymbol{\tau}$ to obtain the tangent vector.

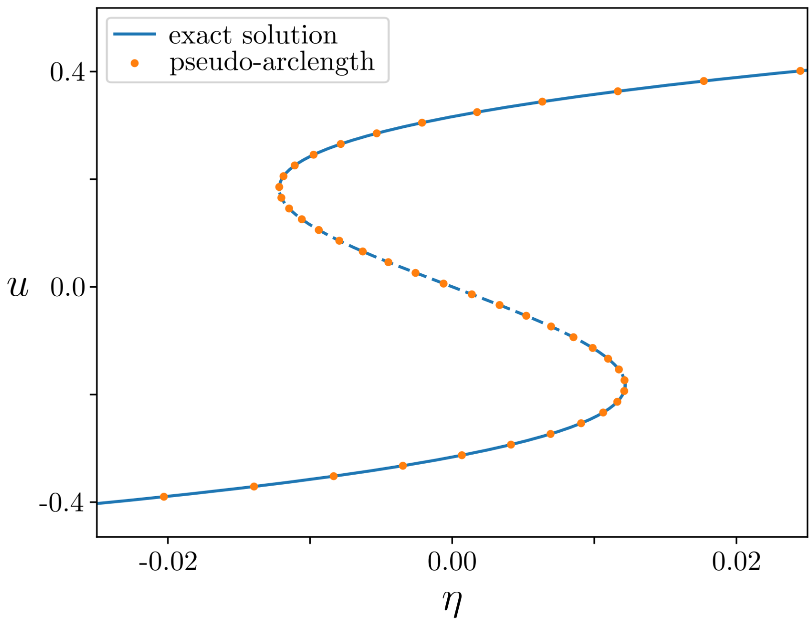

Figure 3.2: Solution of Eq. (3.11) as a function of the parameter η obtained through the pseudo-arclength continuation (orange dots) compared to the exact solution (blue curve).

3.3 Continuation of traveling states

In the particular case of following moving solutions with constant speed c, which is the core of this work, some difficulties arise. The first and most evident one, is that the desired solution is not steady anymore. This can be solved rather easily by changing to the co-moving frame of reference, i.e. by inserting the traveling wave ansatz $\boldsymbol{u}(x,t) = \boldsymbol{a}(x - ct)$, where a is the solution profile in the co-moving frame, into Eq. (3.1). Due to the chain rule, an additional term in the form of a spatial derivative appears in the equation,

$$0 = \boldsymbol{F}(\boldsymbol{a}, \eta) + c\partial_x \boldsymbol{a} \tag{3.12}$$

The second problem is that usually the speed c will change as parameters are varied along the solution branch. Therefore, at each step, the speed will have to be determined by the algorithm. The solution to this problem is to add the speed as another unknown, that is to say, we will now be interested in solving for $\boldsymbol{y} = (\boldsymbol{a}, c, \eta)$. This leads to the third and final problem, which is that due to the additional unknown, we are a missing an additional equation that will guarantee a unique solution to the linearized system. Moreover, we will be solving these systems considering periodic boundary conditions meaning that a translational invariance will appear. In order to deal with the translational symmetry and guarantee a unique solution, a *phase condition* or *pinning condition* must be established. Indeed, if we find a solution $\boldsymbol{a}(x)$, then $\tilde{\boldsymbol{a}}_\theta(x) = \boldsymbol{a}(x+\theta)$ is also a solution for every θ.

The most widely used condition is the *integral phase condition* [93] which takes a reference solution $\boldsymbol{a}_0$ for a certain parameter value η_0 close to the desired solution. The idea is to find the phase that minimizes the difference D between the desired solution $\boldsymbol{a}$ and the reference solution $\boldsymbol{a}_0$. We can define the difference as follows,

$$D(\theta) = \int_0^L dx' \, ||\boldsymbol{a}(x'+\theta) - \boldsymbol{a}_0(x')||^2 \tag{3.13}$$

In order to minimize the difference, we differentiate the above equation, set it equal to zero and then integrate by parts. Thus, we arrive at the following condition which is simpler to implement.

$$p(\boldsymbol{a}, \boldsymbol{a}_0) = \int_0^L dx' \boldsymbol{a}(x') \cdot \left.\frac{d\boldsymbol{a}_0}{dx}\right|_{x'} = 0. \tag{3.14}$$

We can re-define the extended vector function for which we want to find the root of in the following manner,

$$\boldsymbol{H}(\boldsymbol{y}) = \begin{pmatrix} \boldsymbol{F}(\boldsymbol{a}, \eta) + c\partial_x \boldsymbol{a} \\ p(\boldsymbol{a}, \boldsymbol{a}_0) \\ q(\boldsymbol{y}, \boldsymbol{y}_0) \end{pmatrix} \tag{3.15}$$

The derivative of the integral phase condition with respect to the state vector $p_{\boldsymbol{a}}$ may differ depending on the chosen phase condition and implementation of the phase condition. In the simplest case, replacing the integral as a Riemann sum (which is the same as the trapezoidal rule in the case of periodic boundary conditions), the derivative reads

$$p_{\boldsymbol{a}} = \Delta x \frac{d\boldsymbol{a}_0}{dx}. \tag{3.16}$$

Therefore, the corresponding Jacobian of the extended function reads

$$\mathbf{J_H}(\boldsymbol{y}) = \begin{pmatrix} \mathbf{J}(\boldsymbol{a}, \eta) + c\partial_x & \partial_x \boldsymbol{a} & \boldsymbol{F}_\eta(\boldsymbol{a}, \eta) \\ p_{\boldsymbol{a}}(\boldsymbol{a}_0) & 0 & 0 \\ \dot{\boldsymbol{a}} & \dot{T} & \dot{\eta} \end{pmatrix}. \tag{3.17}$$

Note that the last row corresponds, once again, exactly to the tangent vector $\tau = (d\boldsymbol{u}/ds, dT/ds, d\eta/ds) = (\dot{\boldsymbol{u}}, \dot{T}, \dot{\eta})$.

3.4 Continuation for periodic orbits

If we know wish to follow periodic solutions with the continuation method we must first derive a new set of equations to be solved. Mainly, periodic solutions are not steady solutions of the differential equation, however they satisfy the following boundary-value problem.

$$\frac{d\boldsymbol{u}}{dt} = \boldsymbol{F}(\boldsymbol{u}, \eta) \tag{3.18}$$

$$\boldsymbol{u}(t=0) = \boldsymbol{u}(t=T) \tag{3.19}$$

It is convenient to rescale the time $t \to tT$, therefore the condition for periodicity of the solution becomes $\boldsymbol{u}(t=0) = \boldsymbol{u}(t=1)$. Moreover, due to the rescaling in time, a factor T appears on the right-hand side of the dynamical equation. Therefore, the rescaled system becomes,

$$\frac{d\boldsymbol{u}}{dt} = T\boldsymbol{F}(\boldsymbol{u}, \eta) \tag{3.20}$$

$$\boldsymbol{u}(t=0) = \boldsymbol{u}(t=1) \tag{3.21}$$

Moreover, due to the additional time-dependence of $\boldsymbol{u}$, the parametrizing equation for the pseudo-arclength method needs to be modified accordingly. It now reads,

$$q(\boldsymbol{y}, \boldsymbol{y}_0) = \int_0^1 (\boldsymbol{u}(t) - \boldsymbol{u}_0(t)) \cdot \frac{d\boldsymbol{u}}{ds} dt + (T - T_0)\frac{dT}{ds} + (\eta - \eta_0)\frac{d\eta}{ds} - \Delta s = 0 \tag{3.22}$$

Additionally, one can add weights to the previous equation in order to tune the search direction in Newton's method "horizontally" (taking larger steps in the parameter η) or "vertically" (smaller steps in η), see [94] for a more detailed discussion.

Note that we have introduced the period T as another unknown which will be solved through Newton's method along with $\boldsymbol{u}$ and η, i.e. we want to solve for $\boldsymbol{y}(t) \equiv (\boldsymbol{u}(t), T, \eta)$. Moreover, as in the previous section, a phase condition $p(\boldsymbol{u}, \boldsymbol{u_0}) = 0$ must be satisfied in order to deal with the translational invariance (in time) and guarantee the uniqueness of the solution. Finally, we can re-define the extended vector function for which we want to find the root of in the following manner,

$$\boldsymbol{H}(\boldsymbol{y}) = \begin{pmatrix} T\boldsymbol{F}(\boldsymbol{u}, \eta) - \frac{d\boldsymbol{u}}{dt} \\ p(\boldsymbol{u}, \boldsymbol{u}_0) \\ q(\boldsymbol{y}, \boldsymbol{y}_0) \end{pmatrix} \tag{3.23}$$

In order to solve this system of equations subject to periodic boundary conditions, many strategies can be followed. Namely, orthogonal collocation methods (implemented in AUTO

[93]), multiple shooting methods [95], and last but not least, finite difference methods (implemented in pde2path [94]). Although the latter has the least accuracy it is by far the simplest to implement. In the finite difference method, a possible approximation to the first equation in the above system is the trapezoidal rule (used for instance in the Crank-Nicolson scheme for simulating PDEs),

$$\left(\frac{F(\boldsymbol{u}_i)+F(\boldsymbol{u}_{i+1})}{2}\right)T-\frac{\boldsymbol{u}_{i+1}-\boldsymbol{u}_i}{t_{i+1}-t_i}=0 \tag{3.24}$$

Note that the derivative of $\boldsymbol{u}$ with respect to t can be written as a product of a matrix ∇_t and the time-discretized vector $\boldsymbol{u}_i$ $(1 \leq i \leq n_t)$, i.e. it can be written as $\nabla_t \boldsymbol{u}$, in which case the Jacobian $\mathbf{J_H}$ of $\boldsymbol{H}$ reads

$$\mathbf{J_H}(\boldsymbol{y})=\begin{pmatrix} T\mathbf{J}(\boldsymbol{u},\eta)-\nabla_t & \boldsymbol{F}(\boldsymbol{u},\eta) & T\boldsymbol{F}_\eta(\boldsymbol{u},\eta) \\ p_{\boldsymbol{u}}(\boldsymbol{u}_0) & 0 & 0 \\ \dot{\boldsymbol{u}} & \dot{T} & \dot{\eta} \end{pmatrix}. \tag{3.25}$$

Chapter 4

Isolas of localized structures and Raman–Kerr frequency combs in micro-structured resonators (Chaos, Solitons & Fractals 174, 113808)

In section 2.3 the concept of dissipative localized structures (LSs) was introduced. These states can be observed in a huge variety of systems including vegetation patterns, biology, magnetic systems, fluids, granular matter and nonlinear optics [13, 96–100]. In the case of nonlinear optical systems, a particularly interesting type of localized structure can be identified, the so-called optical solitons. Moreover, it has recently been discovered that the formation of solitons in both fiber and micro-resonators gives rise to frequency combs, which are equally spaced spectral lines. These frequency combs are exceedingly useful for technological purposes such as chip-scale atomic clocks [48], terabit per second communication [49] and even the calibration of spectrometers for exoplanet search [50]. From a theoretical perspective, the dynamics of solitons in these optical resonator systems can be accurately described by the forced dissipative nonlinear Schrödinger equation [45, 46, 101, 102], more commonly known as the Lugiato-Lefever equation [44] in the context of optical systems.

The aim of this chapter is the study of the formation of such structures in the case of short solitons where the influence of the stimulated Raman scattering (SRS) cannot be neglected and higher-order dispersion terms appear. In this case, a reduced model in the form of a non-local Swift-Hohenberg equation is proposed to provide analytical results and an in-depth numerical description. By means of a combination of numerical simulations and continuation of the reduced model (see 3.3 for a detailed discussion on the continuation of traveling states), it can be seen that the SRS induces a forced symmetry breaking leading to the motion of both the bright and dark solitons, as well as a disconnection between the different branches of LSs. Consequently, the traditional homoclinic snaking bifurcation diagram breaks apart and instead, a family of isolas emerges. Lastly, a numerical analysis of the original model, the generalized LLE, confirms both the formation of drifting LSs and the presence of isolas due to the reflection symmetry breaking, in agreement with previous studies [103, 104].

Chaos, Solitons and Fractals 174 (2023) 113808

Contents lists available at ScienceDirect

Chaos, Solitons and Fractals

journal homepage: www.elsevier.com/locate/chaos

Isolas of localized structures and Raman–Kerr frequency combs in micro-structured resonators

M. Tlidi [a,*], M. Bataille-Gonzalez [b], M.G. Clerc [b], L. Bahloul [c,d], S. Coulibaly [e], B. Kostet [a], C. Castillo-Pinto [f], K. Panajotov [f,g]

[a] Faculté des Sciences, Université libre de Bruxelles (ULB), Campus Plaine, 1050, Brussels, Belgium

[b] Departamento de Física and Millennium Institute for Research in Optics, Facultad de Ciencias Físicas y Matemáticas, Universidad de Chile, Casilla 487-3, 1050, Santiago, Chile

[c] Electronics Department, Institute of Science, University Center of Tipaza Morsli Abdallah, Ouade Merzouk, 4200, Tipaza, Algeria

[d] Laboratoire d'Instrumentation, University of Sciences and Technology Houari Boumediene (USTHB), Algeria

[e] Université de Lille, CNRS, UMR 8523-PhLAM-Physique des Lasers Atomes et Molécules, F-59000, Lille, France

[f] Brussels Photonics Team, Department of Applied Physics and Photonics (B-PHOT TONA), Vrije Universiteit Brussel, Pleinlaan 2, 1050, Brussels, Belgium

[g] Institute of Solid State Physics, Bulgarian Academy of Sciences, 72 Tzarigradsko Chaussee Blvd., 1784, Sofia, Bulgaria

A B S T R A C T

We theoretically investigate the combined impact of the Kerr and stimulated Raman scattering effect on the formation of localized structures and frequency comb generation. We focus on the regime of traveling wave instability. We first perform a real-order parameter description by deriving a Swift–Hohenberg equation with nonlocal delayed feedback. Second, we characterize the motion of traveling wave periodic solutions by estimating their thresholds as well their speed. By using a numerical continuation method, we construct a bifurcation diagram showing the emergence of traveling wave periodic solutions, as well as bright and dark moving localized structures. Numerical simulations of the generalized Lugiato–Lefever equation confirm evidence of isolas of localized structures. More importantly, we show that the stimulated Raman scattering strongly impacts the dynamics of localized structures by creating isolas consisting of bright and dark localized structures, and by inducing a motion of these structures. Finally, we provide a geometrical interpretation of the formation of isola stacks based on dynamical systems theory.

1. Introduction

In the early 2000s, Hänsch and Hall introduced and developed the optical frequency combs, which are equally spaced coherent laser lines [1,2]. They were generated by microcavity resonators and used to count light cycles. Their realization using mode-locked lasers and dissipative solitons has revolutionized many fields of science and technology, such as high-precision spectroscopy, metrology, and photonic analog-to-digital conversion [3,4]. The so-called soliton frequency combs are associated with the formation of localized structures (LSs) of light, which maintain their shape during propagation, and they have been experimentally reported in optical microcavities [5,6]. Those frequency combs are the spectral content of the localized structures, often called dissipative solitons, which have been theoretically predicted in driven cavities [7,8]. Dissipative solitons have been reported in the conservative limit when the injection and losses are both small and under zero frequency detuning limit [9,10]. The link between the localized structure in (micro-)resonators and frequency combs has been established [11–14]. The dynamics of interacting LSs can cause the stabilization of bounded localized states when a periodic forcing is applied [15–17], when taking into account fourth-order dispersions [18–21] or spatial filtering (or gain dispersion in the time domain) [22]. This is caused by Cherenkov radiation [23–27], i.e., the radiation of dispersive waves that are weakly decaying.

Considerable attention has been paid recently to the formation of frequency combs under the combined action of Kerr nonlinearity and stimulated Raman scattering (SRS) in optical resonators such as whispering gallery mode resonators [28,29]. Since the Raman gain bandwidth is large (it is around 10 THz for silica glass), the combined influence of Raman scattering and Kerr nonlinearity is frequently observed [30–35]. The effects of SRS and Kerr on the front dynamics leading to the stabilization of LSs have recently been studied [36–40] in normal dispersion materials. In this case, LSs have been observed in a domain far from the traveling wave instability. In this regime, it has been shown that the combined action of SRS and Kerr nonlinearity is at the origin of generation of moving bright LSs [36–40]. In the absence of the SRS effect, bright LSs are unstable. The mechanism leading to the formation of LSs with varying width results from the locking front connecting two coexisting continuous wave states [41–44]. Close to the critical point associated with optical bistability, the

* Corresponding author.
E-mail address: mtlidi@ulb.ac.be (M. Tlidi).

https://doi.org/10.1016/j.chaos.2023.113808
Received 7 June 2023; Accepted 7 July 2023
Available online 27 July 2023

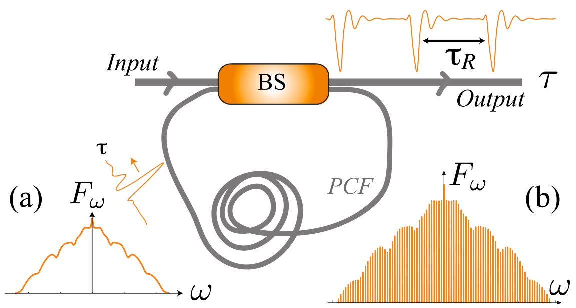

Fig. 1. Schematic setup of a ring cavity filled with a photonic crystal fiber (PCF). The cavity is driven by a coherent external injected beam. BS denotes a beam splitter and τ_R is the roundtrip time. (a) A single moving dark localized structure circulating within the cavity and its Fourier transform. (b) Frequency comb representing the Fourier transform of the train of dark localized structures coming out from the cavity.

interaction law between two well-separated fronts has been established analytically [37,39]. In many cases, properties of such localized states can be related to the phenomenon of collapsed snaking that has been found in the scalar Lugiato–Lefever equation (LLE [45]) with SRS [40] and without SRS [46,47], and in the vectorial case where polarization degree of freedom is considered [48,49].

The dispersion curve may be highly controlled using photonic crystal fibers. Such fibers play a significant role, especially traveling waves (TW) for supercontinuum generation [50–53]. When optical resonators are operating close to the zero dispersion wavelength, it is necessary to take into account higher-order dispersion. In silicon microring resonators, Kerr-Raman scattering and higher order dispersion have an impact on frequency comb formation [54–60]. In particular, complex dynamics characterized by the formation of dispersive waves, self-frequency-shifting, and frequency-locking have been reported [54].

In regimes devoid of traveling modulational instability, the impact of stimulated Raman scattering and the Kerr effect has been reported. In this case, bistability between CW solutions is necessary since the resulting LSs consist of an heteroclinic connection between the two branches of CW states [37,39]. Their bifurcation diagram follows a collapsed snaking type of bifurcation [40].

In this contribution, we theoretically investigate the homoclinic type of LSs in the regime where the system develops a traveling wave instability. Temporal LS can be formed even in the monostable regime. This type of solution has a homoclinic snaking type of bifurcation in the absence of SRS. We show that stimulated Raman scattering breaks the snaking structure and promotes LS branches in the form of isolas, which can form even in the monostable regime.

We show that when this instability becomes subcritical, the system develops a high degree of multistability: besides the continuous wave (CW), and the traveling periodic solutions, which are both stable, an additional variety of stable localized structures are generated. This behavior is independent of whether the system is operating in the monostable or the bistable regime. Using a continuation algorithm, we have established the bifurcation diagram associated with traveling waves. More importantly, we show that localized structures and combs branches of solution are isolas since they are not connected to any modulational instability or traveling wave thresholds.

The structure of the paper is as follows. We describe the creation of periodic TW solutions in the supercritical domain following the presentation of the Swift–Hohenberg equation with stimulated Raman scattering in Section 2. To characterize the motion, we estimate the threshold associated with the onset of motion as a function of injected field amplitude, as well as their speed. We show that when this instability becomes subcritical, the system develops a high degree of multistability: besides the continuous wave (CW), and the traveling periodic solutions, which are both stable, an additional variety of stable localized structures is generated. This behavior is independent of whether the system is operating in the monostable or bistable regime. Then, in Section 3, we carry out a direct numerical simulation of dark and bright localized structures. We are able to create their bifurcation diagram, which provides proof of the existence of a stable single and multiple isolas, thanks to the continuation algorithm (see Subsection 3.1). In the last part of Subsection 3.2, we present numerical simulations showing that the generalized LLE supports isolas of temporal LSs. Section 4 discusses a geometrical interpretation of isola stack formation. Following the conclusions, we provide as an appendix a full derivation of the Swift–Hohenberg equation with nonlocal delayed feedback.

2. A derivation of a Swift–Hohenberg equation with stimulated Raman scattering

We consider a ring resonator filled-in with a Kerr dispersive medium such as a photonic crystal fiber (PCF). Fig. 1 shows a schematic of the PCF resonator. This resonator is coherently driven by a continuous wave monochromatic light with an electric field E_i and corresponding power E_i^2. Through the use of a beam splitter, the transmitted portion of this field is directed into the cavity and propagates through the PCF under the influence of dispersion, the Kerr effect, stimulated Raman scattering, and losses. During each round trip, the driving field and the light that moves throughout the resonator are coherently superimposed. High-order chromatic dispersion effects are crucial to the dynamics of this system when the PCF resonator is operating close to the zero dispersion wavelength. Taking into account these effects, the slowly varying envelope of the electric field within the resonator is described by the following generalized Lugiato–Lefever equation [55]

$$\begin{aligned}\frac{\partial E}{\partial \zeta} &= E_i - (1+i\Delta)E + i\left(1-f_r\right)|E|^2 E \\ &+ i\beta_2\frac{\partial^2 E}{\partial T^2} + i\beta_4\frac{\partial^4 E}{\partial T^4} \\ &+ i f_r E\int_{-\infty}^{T}\phi(T-T')|E(T')|^2 dT'. \end{aligned} \tag{1}$$

where $E = E(\zeta, T)$ is the normalized mean-field cavity electric field, Δ accounts for the normalized detuning parameter, and losses are normalized to unity. The time ζ is the slow time describing the evolution over successive round trips, and T is the fast time in the reference frame moving with the group velocity of the light within the resonator. E_i is the input field amplitude. β_2 and β_4 are the second- and the fourth-order dispersion terms, respectively. The stimulated Raman scattering is described by the last term of Eq. (1) and by the cubic nonlinear term. The strength of the Raman is f_r. The kernel function is

$$\phi(\tau) = a\exp(-\tau/\tau_2)\sin(\tau/\tau_1)$$

with $a = \tau_0(\tau_1^2+\tau_2^2)/(\tau_1\tau_2^2)$, and $\tau_0 = [|\beta_4 L|/24\alpha]^{1/4}$, where α is the loss parameter, and L is the resonator length. The optical losses are determined by the mirror transmission and the intrinsic material absorption. The choice of this kernel, or influence function, shows an excellent agreement with experiments using standard fibers [61,62]. In the absence of the stimulated Raman scattering, i.e., $f_r = 0$, we recover the LLE with fourth-order dispersion [63]. In this case, Eq. (1) admits front-like states connecting the two continuous wave solutions (CWs) forming a bistable state [41], stationary LSs [18], and moving LSs due to the third-order dispersion effect [19,64–66].

We derive a paradigmatic Swift–Hohenberg equation (SHE) with stimulated Raman scattering describing the evolution of pulses propagating in a photonic crystal fiber resonator. This reduction is performed close to nascent optical bistability. Starting from the generalized LLE Eq. (1), the deviation u of the electric field from its value at the onset of bistability obeys a generalized SHE with stimulated Raman scattering

$$\begin{aligned}\partial_t u &= \eta + \mu u - u^3 + \beta\partial_\tau^2 u - \partial_\tau^4 u \\ &+ \int_{-\infty}^{\tau}\phi(\tau-\tau')u(\tau')d\tau', \end{aligned} \tag{2}$$

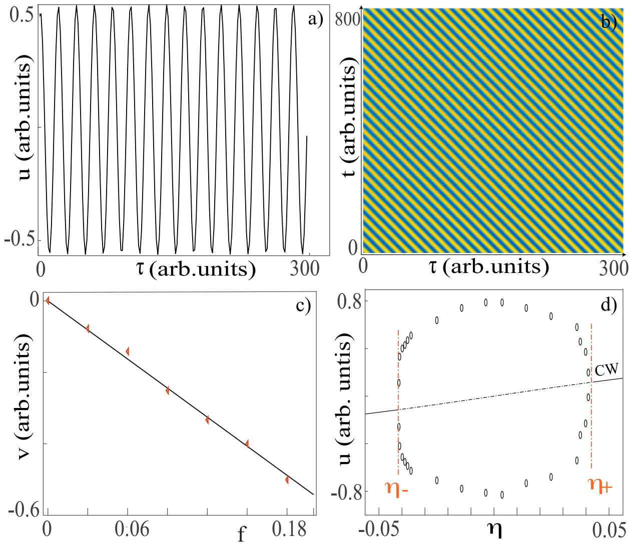

Fig. 2. Traveling wave solutions in the supercritical regime. (a) Profile of a periodic traveling wave solution obtained by numerical simulations of Eq. (2). (b) $t-\tau$ map showing the time evolution of the profile. (c) The velocity of the traveling wave solution v as a function of the strength of the Raman effect. Full line and red triangles show, respectively, the analytical solution (formula Eq. (5)) and numerical simulation results. (d) Supercritical bifurcation diagram obtained in the monostable regime. The full and broken lines correspond to the stable and unstable homogeneous steady state, respectively, while the circles correspond to the maxima and the minima of moving periodic structures. Parameters are $\beta=-1.5$, $\tau_0=14$, $f=0.18$, $\tau_1=3$, $\tau_2=10$ (a, b, c) $\mu=-0.35$, and $\eta=-0.35$. (For interpretation of the references to color in this figure legend, the reader is referred to the web version of this article.)

A detailed derivation is presented in the Methods section. The parameters η and μ represent, respectively, the driven field and the frequency detuning deviations from their value at the critical point associated with bistability. The second and fourth-derivatives describe dispersion terms. The last contribution accounts for the stimulated Raman scattering with the new kernel function defined as $\phi(\tau) = \sqrt{3}/2af\,\exp^{-\tau_0(\tau-\tau')/\tau_2}\sin(\tau_0(\tau-\tau')/\tau_1)$ where f is the strength of the nonlocal delayed feedback.

The Fisher–Kolmogorov–Petrovsky–Piscunov (FKPP) equation derived in earlier research [37,39] is much different from Eq. (2). First, because the fourth derivative term originating from high-order dispersion is missing, the FKPP equation is unable to characterize the traveling modulational instability. Second, the scaling in fast and slow times utilized to derive the FKPP equation differs significantly from the scaling used to establish the Swift–Hohenberg with nonlocal response Eq. (2).

In the absence of stimulated Raman scattering, we recover the well-know SHE that has been first derived in the spatial domain [67,68] and in the temporal domain [66]. Without the fourth-order dispersion and the stimulated Raman scattering, Eq. (2) supports stationary localized structures and clusters of them both in the spatial domain [8] and in the temporal domain [66]. In this case, traveling wave instability and motion of temporal structures are forbidden. This is because, in the absence of stimulated Raman scattering and fourth order of dispersion, Eq. (2) is variational. This means that a Lyapunov functional exists for this equation, ensuring that the evolution will move towards the state, for which the functional has the smallest possible value that is compatible with the system boundary conditions.

The linear CW solutions of Eq. (2) satisfies the cubic equation $\eta = u_s^3 - (\mu + \sqrt{3}f/2)u_s = u_s^3 - 3\delta u_s/4$. The linear stability analysis with respect to finite frequency perturbations of the form $\exp(\lambda t + i\omega\tau)$ yields eigenvalues λ of the linear operator. The CWs states exhibit a traveling wave instability leading to moving periodic solutions when the real part of λ is positive. When taking into account the stimulated Raman scattering and higher order dispersion, a portion of homogeneous solutions u_s undergo a traveling wave instability in the range $u_- < u_s < u_+$. The thresholds associated with this instability are

$$u_\pm = \pm\sqrt{\frac{\beta^2+4\mu}{3} - \frac{\sqrt{3}f(\tau_1^2+\tau_2^2)}{3(\tau_1^2-\tau_2^2)}}. \tag{3}$$

The corresponding injected field amplitudes are

$$\eta_\pm = -\left[\frac{\sqrt{3}f}{6}\frac{\tau_1^2}{\tau_1^2-\tau_2^2} + \frac{5\sqrt{3}f+8\mu-\beta}{12}\right]u_\pm, \tag{4}$$

where the frequency at both thresholds is $\omega_c^2 = -\beta/2$ with ω_c as the critical frequency. From this threshold emerge periodic traveling wave solutions whose profile and $t-\tau$ map are shown respectively, in Fig. 2(a) and 2(b). We derive an analytical formula for the velocity v of a traveling wave solution. The results are plotted in Fig. 2(c), showing excellent agreement between the analytical formula and numerical results. The bifurcation diagram is shown in Fig. 2(d) indicating that the traveling wave instabilities appear supercritically. The mathematical expressions for the traveling wave instability thresholds $\eta_\pm$ and the corresponding intracavity field amplitudes $u_\pm$ are provided explicitly in Methods section, respectively (see Eqs. (3) and (4)). The temporal period at both thresholds is $T_c = 2\pi\sqrt{2}/\sqrt{-\beta}$. We have also estimated the linear velocity of the periodic solution

$$v = \frac{\partial Im(\lambda)}{\partial\omega_c} = \frac{4\sqrt{3}f_r\beta{\tau_0}^3\tau_1^4\tau_2^4\left({\tau_1}^2+{\tau_2}^2\right)A_1}{A_2^2}, \tag{5}$$

where A_1 and A_2 are

$$\begin{aligned} A_1 &= \left[3\beta\tau_1^2\tau_2^2 - 4\tau_0^2(\tau_1^2-{\tau_2}^2)\right] \\ &\quad -4{\tau_0}^4(\tau_1^2+\tau_2^2)^2, \\ A_2 &= \beta\tau_1^2\tau_2^2\left[\beta\tau_1^2\tau_2^2 - 4\tau_0^2(\tau_1^2-{\tau_2}^2)\right] \\ &\quad +4\tau_0^4({\tau_1}^2+{\tau_2}^2)^2. \end{aligned} \tag{6}$$

The velocity as well as the thresholds associated with the traveling wave instability have been obtained analytically within the limit of a low-frequency regime.

3. Isolas of frequency comb generation

In the absence of stimulated Raman scattering, the fourth-order dispersion strongly affects the dynamical behavior of all fiber resonators by allowing for new unstable frequencies to appear, and the modulational unstable domain to become bounded [63]. In the monostable case, the primary instability threshold is degenerate where two separate frequencies simultaneously appear while in the bistable case, high-frequency modulational instability precedes the limit point [63]. Furthermore, the fourth-order dispersion allows for the stabilization of dark LSs in the temporal [18] and spatial [69] domains. The interaction and pinning can be strongly modified by the influence of high-order dispersion effects [25,26].

Localized structures usually found close to the subcritical modulational instability [7,8] exhibit a well-known homoclinic snaking type of bifurcation that has been first reported in the time domain in [18], and in the spacial domain [69] (see also recent papers on this issue [70,71]). They exhibit multistability behavior in a finite range of parameters referred to as the pinning region [72]. From a dynamical point of view, their bifurcation diagram consists of two snaking curves; one describes LSs with odd number of peaks, the other corresponds to an even number of peaks. The two snaking curves are connected and emerge from the modulational instability threshold. They are intertwined, which is associated with the back-and-forth oscillations across the pinning region. This feature is a characteristic of systems possessing a reflection symmetry in the spatial domain $x \to -x$ or in the temporal domain ($\tau \to -\tau$) such as a Swift–Hohenberg type of equation [73,74] and the Lugiato–Lefever equation [70,71,75].

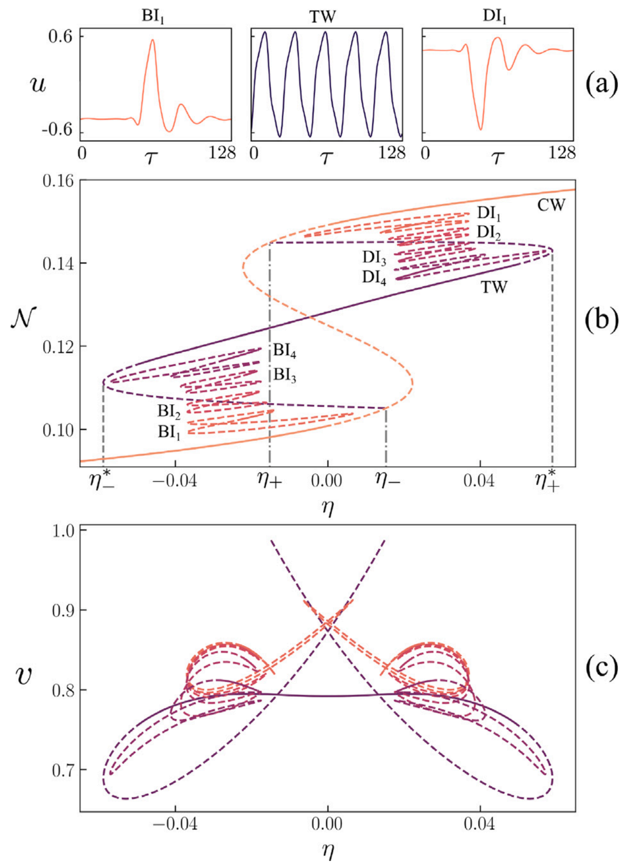

Fig. 3. Isola stack of localized structures obtained by continuation algorithm of Eq. (2). (a) Solution profiles for the respective points in the bifurcation diagram with $\eta = -0.015$, $\eta = 0.003$, and $\eta = +0.014$. (b) Bifurcation diagram obtained in the bistable regime. BI_n and DI_n, i=1,2,3,4 represent bright and dark isolas of solutions with n peaks and n dips, respectively. (c) Speed of LSs as a function of the injection parameter η. Parameters are $\mu = -0.1$, $\beta = -1.8$, $f = 0.28$, $\tau_0 = 1$, $\tau_1 = 3$, and $\tau_2 = 10$. (For interpretation of the references to color in this figure legend, the reader is referred to the web version of this article.)

3.1. Isolas of localized structures in the Swift–Hohenberg equation with nonlocal response

In what follows, we investigate numerically the formation of both bright and dark LSs under the combined influence of SRS-Kerr together with fourth-order dispersion. The presence of stimulated Raman scattering breaks the reflection symmetry and allows for the motion of LS. We focus on a strongly nonlinear regime where the traveling wave bifurcation is subcritical. For this purpose, we proceed by discretizing Eq. (2) in $N = 512$ nodes with a temporal step size of $\Delta\tau = 0.25$. Temporal derivatives with respect to the retarded time τ are then computed spectrally for better accuracy and time integration is performed using a 4th order adaptive Runge–Kutta scheme. traveling waves and moving bright and dark localized structures solutions of Eq. (2) are obtained by integrating numerically with periodic boundary conditions. They are shown in Fig. 3(a), and they are denoted by TW, BI_1, and DI_1, respectively.

We first seek moving periodic and localized states with constant speed υ. These states correspond to solutions of Eq. (2) in the co-moving frame with υ

$$0 = \eta + \mu u - u^3 + \upsilon\partial_\tau u + \beta\partial_\tau^2 u - \partial_\tau^4 u + \frac{\sqrt{3}}{2fa}\int_{-\infty}^{\tau}\phi(\tau-\tau')u(\tau')d\tau'. \tag{7}$$

In addition, due to the translational symmetry of the system, we must add a pinning condition in order to ensure the uniqueness of the solution

$$0 = \int u_0(\tau)\partial_\tau u(\tau)d\tau. \tag{8}$$

This condition can be derived by imposing that the difference with a previously known solution u_0 for a given parameter $\eta_0 \approx \eta$ must be minimized, i.e., $min_{\Delta\tau}\|D(\Delta\tau)\|$, where $\|.\|$ is the L_2 norm, which will be defined below, and $D(\Delta\tau) \equiv u(\tau+\Delta\tau) - u_0(\tau)$. Eqs. (7) and (8) are solved by means of the pseudo-arclength continuation method [76] which allows to seamlessly follow the solution branch through folds (cf. Fig. 3).

To visualize these solutions, it is convenient to plot the dimensionless L_2 norm,

$$\mathcal{N} = \int d\tau|u-u_s|^2 \tag{9}$$

as a function of η. The results are summarized in the bifurcation diagram shown in Fig. 3(b). The critical thresholds $\eta_\pm$ associated with the TW instability are located on the upper and lower branch of the CW solution.

In the bistable regime, the TW instability always appears subcritically. From the threshold associated with this instability emerges an unstable branch of TW periodic solutions (dotted purple curve). The existence domain of TW periodic solutions is in the range $\eta_-^* < \eta < \eta_+^*$ (purple curve). This branch of TW solutions is connected to the upper threshold η_+ by a dotted purple curve as shown in Fig. 3(b). More importantly, the left (right) portion of Fig. 3(b) shows a set of branches of bright (dark) LS. These localized state branches are distinguished by the multitude of peaks and dips in their temporal structure. An example of periodic TW wave, bright and dark localized structures are shown in Fig. 3(a). The two sets of branches of bright and dark LSs form isolas of localized states that are not connected to the thresholds of the TW instabilities. We estimate the velocity of LSs to better characterize them, and the results are presented in Fig. 3(c). This figure shows that the speed reduces as the number of peaks rises. The isola branch with the purple color corresponds to the single peak solution that is the fastest LSS.

Although both the bright and the dark localized branches of solutions are shown in the bifurcation diagram in Fig. 3, to simplify the analysis, we focus on the dark localized structures. Their shape changes as a function of the strength of the injected field amplitude as shown Fig. 4(a) for the corresponding points A, B, C, and D in the bifurcation diagram of Fig. 4(c). This figure is obtained by zooming in on Fig. 3(b) around the upper CW solution. This portion of the bifurcation diagram reveals clearly that branches of localized structures are not connected to the TW instability. Moving dark localized structures form single or multiple isolas. This feature is displayed in Fig. 4(c). The spectra of dark LS are shown in Fig. 4(b).

3.2. Isolas of localized structures in the generalized LLE with Raman scattering

The reduction from the generalized LLE Eq. (1) to a Swift–Hohenberg equation without a nonlocal delayed response Eq. (2) is a well-known framework for the analysis of periodic or localized structures [8]. It typically applies to systems that experience a modulational instability close to a second-order critical point, marking the onset of a hysteresis loop (nascent bistability). It has been demonstrated that the Swift–Hohenberg equation with high orders of dispersion and no Raman scattering reproduces qualitatively the same results as the full LLE model [66].

In what follows, we shall show that isolas of localized structures are also solutions of the full LLE model Eq. (1). For this purpose, let us fix the detuning parameter by considering the monostable regime, i.e., $\Delta < \sqrt{3}$. Fig. 5 depicts an example of a single peak moving localized structures and their corresponding comb.

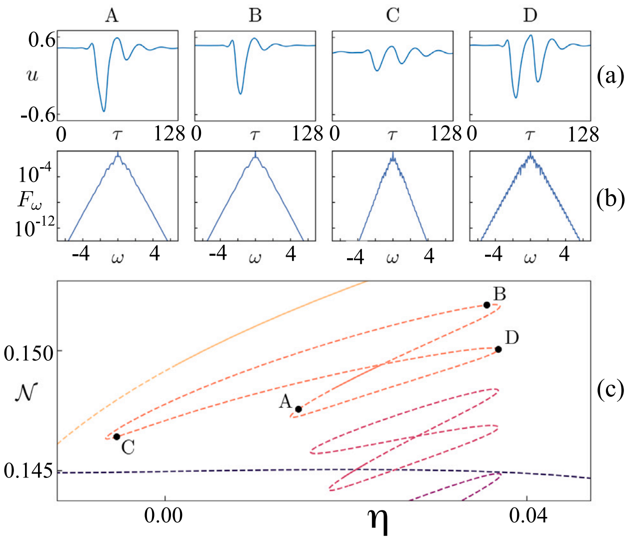

Fig. 4. (a) Solution profiles corresponding to the points A, B, C and D in the bifurcation diagram. (b) Corresponding Fourier spectra. (c) Magnification on the upper CW branch of the bifurcation diagram presented in Fig. 3(b). Same parameters as in Fig. 3. (For interpretation of the references to color in this figure legend, the reader is referred to the web version of this article.)

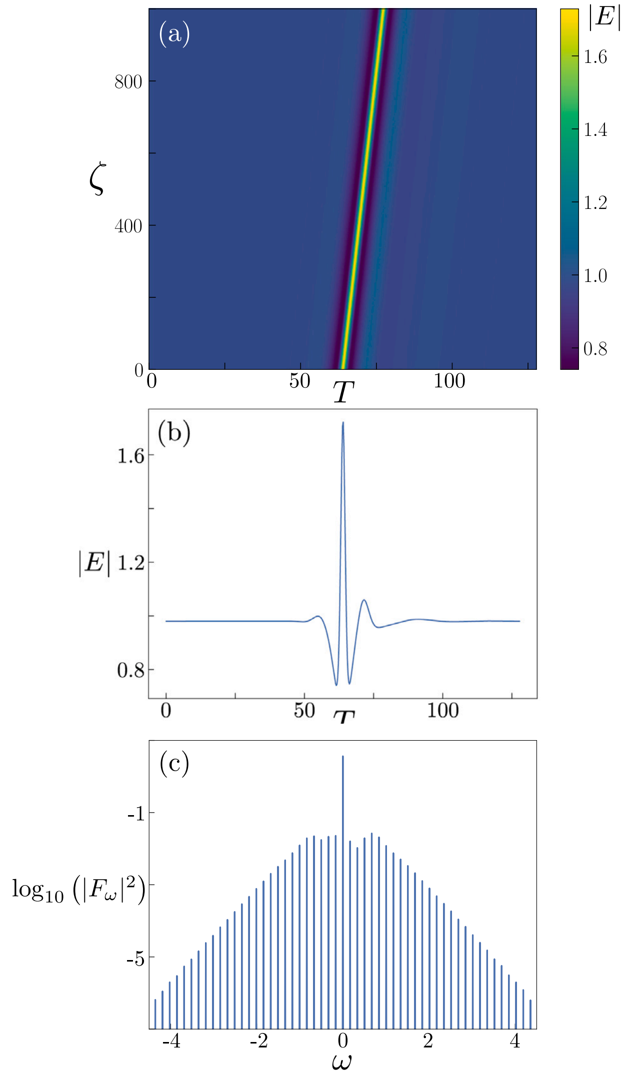

Fig. 5. Moving localized structures obtained by numerical simulations of Eq. (1). (a) T-ζ map. (b) Temporal profile (c) Corresponding Fourier spectrum. Parameters are $\Delta = 1.7$, $E_i = 1.219$, $f_r = 0.05$, $\beta_2 = 1$, $\beta_4 = 0.01$, $\tau_0 = 1$, $\tau_1 = 3$, $\tau_2 = 10$. Numerical simulation has been performed using 512 cells, with a T step of 0.25 and a ζ step of 0.001.

They are obtained numerically by using a periodic boundary condition compatible with the ring geometry of the optical resonator depicted in Fig. 1. The grid size is 512 with a temporal step size of 0.25.

The T-ζ map of Fig. 5(a) depicts traveling temporal localized structures with a constant speed. The motion is directly imputable to the stimulated Raman scattering effect since it breaks the reflection symmetry $\zeta \to -\zeta$. As shown in Fig. 5(b), the profile of temporal localized structures becomes asymmetric in this case. The spectral content of the intensity profile forms an optical frequency comb that shows an asymmetry as shown in Fig. 5(c). The comb lines are all equally spaced since the free spectral range, given by the inverse of the cavity round-trip time, has a fixed value.

Fig. 6 depicts a single peak localized structure (BI_1), bounded states (BI_2), and a periodic train of peaks (TW) moving at constant speed. The above mentioned continuation algorithm allows for the construction of the bifurcation diagram shown in Fig. 6(b). There are four curves in the plot of the L_2 norm as a function of the injected field E_i. The blue curve displays a single CW solution. The red curve represents the branch of traveling periodic solutions that emerges from the CW solutions. The green and orange curves represent the single and bound branches, which state localized structures with one and two peaks, respectively. Because they are far apart, temporal localized structures interact via their exponentially decaying tails and bounded states. Interactions of localized structure have been studied in the absence of stimulated Raman scattering, in the spatial domain [77]. This weak type of interaction is affected by the third- [25] and the fourth- [26] orders of dispersion.

The profile of a moving peak localized structure is deeply affected by the change of the injected field amplitude. This feature is illustrated in Fig. 7(a). A zoom on that figure shows that neither branches of single and bounded states localized are connected to the CW solutions (see Fig. 7(b)). As in the limit of nascent bistability where the dynamics is governed by a Swift–Hohenberg with nonlocal delayed feedback (Eq. (2)), the generalized LLE Eq. (1) exhibits isola type of solutions. The stimulated Raman scattering is directly responsible for disconnecting the localized branches of solutions from the CW solution. Because we integrate the nonlocal delayed integral term from $-\infty$ to a finite time, the reflection symmetry is broken. However, the branches of periodic TW solutions are still connected to the CW solutions.

In order to better understand the creation of isolas from the perspective of dynamical system theory, we give a geometrical explanation in the next section.

4. Geometrical interpretation

The localized states are stationary solutions of the co-moving frame of Eq. (2). Geometrically, these solutions correspond to homoclinic curves in the phase portrait [78]. The latter is a geometrical representation of the trajectories of the dynamical system of Eq. (2) in the phase plane, which is the Poincaré plane (see Fig. 8). The geometrical interpretation of homoclinic snaking is a well-documented issue and is by now fairly well understood [74]. The homoclinic orbit bifurcates from a heteroclinic loop which is generated by connecting CW (equilibrium) to a periodic orbit. The homoclinic curves correspond to the asymptotic state of the localized solutions and are formed by the intersection of the stable (W^s) and unstable (W^u) manifolds of the uniform equilibrium. The phase portrait's manifold intersection is shown schematically in Fig. 8. The points represent the various localized states or homoclinic curves. Note that the equilibrium that produces manifolds is a hyperbolic equilibrium for the related stationary system and corresponds to

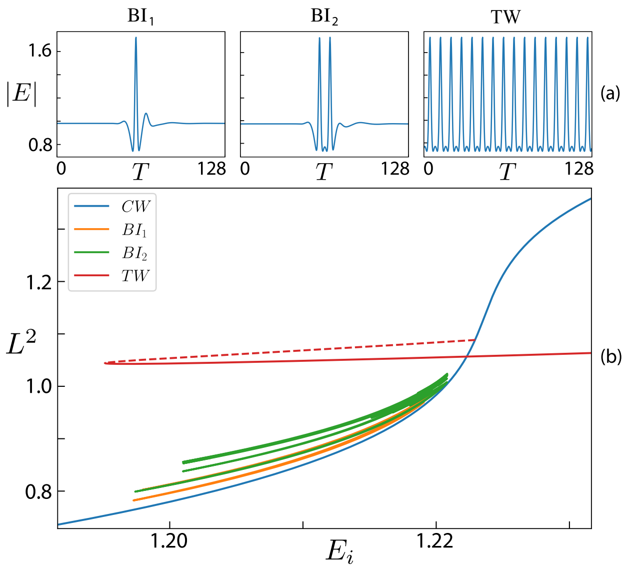

Fig. 6. (a) Temporal profile of a single, bounded states, and periodic train of pulses indicated by BI_1, BI_2, and TW, respectively. (b) Bifurcation diagram representing CW (blue curve), train of periodic pulses (red curve) solutions. The unstable branch of TW is indicated in doted curve. The two isolas of localized structures are indicated by green and orange colors, respectively. Parameters are the same as in Fig. 5. (For interpretation of the references to color in this figure legend, the reader is referred to the web version of this article.)

a uniform stable condition of the spatiotemporal system (co-mobile). That is, the manifolds are the nonlinear extension of the eigenvectors associated with the equilibrium.

When the phase portrait's dimension is higher than two, the manifolds surrounding a hyperbolic point exhibit a complicated geometric structure typically referred to as *manifold entanglement* [79,80]. Poincaré first proposed that this entanglement would lead to chaotic behavior in regular temporal systems [81]. The coexistence of localized structures caused by the entangled manifolds in the portrait space of stationary systems is known as the homoclinic snaking bifurcation diagram [74,82]. This coexistence of solutions is characterized by the fact that the symmetrical localized states are connected with other ones with more or less one spatial oscillation. This process occurs through saddle–node bifurcations, generating a snake-like structure in the bifurcation diagram [74]. Experimental observation of this bifurcation diagram has been carried out for a liquid crystal light valve with optical feedback [83]. The ordered sequence of homoclinic curves (localized states) results from spatial reflection symmetry in the system ($\tau \rightarrow -\tau$), where Π represents the spatial reflection symmetry plane.

Then the unstable manifold intercepts the plane of symmetry Π. Due to the reflection symmetry, the stable manifold intercepts Π in a mirror image. This entanglement generates a sequence of symmetric localized states represented by the green dots in Fig. 8(a). The bifurcation diagram associated with LSs contains two intertwined snaking curves. This classical scenario is not expected in irreversible systems, i.e., systems devoid of reflection symmetry. In this case, asymmetrical solutions shown in Fig. 3(a) or in Fig. 8(b) are possible. Fig. 8(b) illustrates asymmetrical solutions indicated by black points. These are close to the homoclinic bifurcation diagram, but not connected with other LSs. This behavior is referred to as *isolas* [84–88]. Namely, the solutions only connect with other four asymmetric ones, forming a loop in the phase diagram, typically with the shape of a Lissajous curve (see Figs. 3 and 4(c)).

In the case that the system under study loses reflection symmetry ($\tau \nrightarrow -\tau$), the intersection of the stable and unstable manifolds does not coincide generically with the surface Π that initially accounted for the plane of symmetry [89]. Even both manifolds now are not symmetrical.

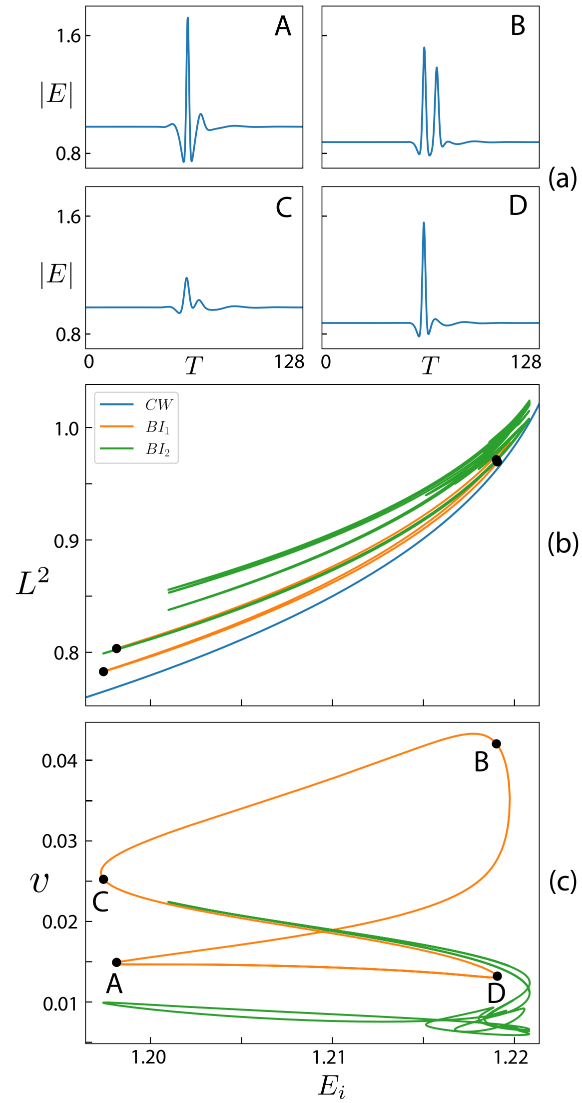

Fig. 7. (a) Profiles of localized structures at different values of the injected field intensity. (b) Zoom of Fig. 6(b) showing isola of solutions for the generalized LLE Eq. (1). (c) Speed of the localized structures as a function of the injected field intensity. Parameters are the same as in Fig. 6. (For interpretation of the references to color in this figure legend, the reader is referred to the web version of this article.)

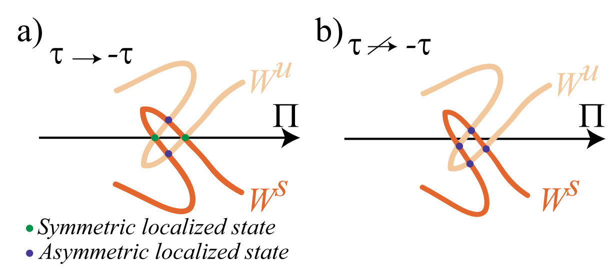

Fig. 8. Schematic representation of stable (W^s) and unstable (W^u) manifold in the phase portrait. Representation of intersection of stable and unstable manifolds in systems with reflection symmetry (a) and without symmetry (b). Π accounts for the spatial reflection symmetry plane. The colored dots represent the homoclinic curves (localized structures). (For interpretation of the references to color in this figure legend, the reader is referred to the web version of this article.)

Fig. 8(b) depicts the typical image of the intercepts of manifolds in systems without reflection symmetry. Then all localized structures become asymmetric since there is no ordered sequence imposed by reflection symmetry. Hence, the system transforms the homoclinic snaking into an isola stack (see Fig. 3) [86,87,89]. Namely the localized structures in the bifurcation diagram are connected by groups of four solutions generically.

In brief, the Swift–Hohenberg Eq. (2) without the effect of stimulated Raman scattering is known to exhibit a homoclinic snaking bifurcation diagram [89]. When taking into account the odd-order of dispersion, the reflexion symmetry is broken. For instance, in the presence of third-order dispersion, bright and dark dissipative solitons become asymmetric and acquire an additional group velocity shift associated with this asymmetry [90]. In this case, isolas of localized structures have been reported [90]. Incorporating the stimulated Raman scattering breaks the reflection symmetry and induces an isola stack. In this case, the homoclinic snaking bifurcation structure breaks up.

5. Conclusions

To sum up, we have investigated the confinement of light in driven nonlinear ring cavities containing a micro-structured photonic crystal fiber. The effects of the Kerr effect, stimulated Raman scattering, and high orders of dispersion on the formation of temporal localized structures have been theoretically examined. In the spectrum domain, these nonlinear solutions correspond to combs.

We performed a real order parameter description leading to the derivation of a Swift–Hohenberg type of equation with a nonlocal delayed response. Due to the presence of stimulated Raman scattering, the resultant Swift–Hohenberg equation is nonvariational, which means that there is no potential or Lyapunov functional to minimize. We show that this equation supports traveling waves solutions. We have characterized them in the supercritical regime. The threshold as well as the speed are estimated.

In the subcritical regime where periodic traveling solutions coexist with stable background (CW solution), both bright and dark moving localized structures are stabilized. These structures are asymmetric and direct numerical simulations have indicated that both structures have an overlapping domain of coexistence. By using a continuation algorithm, we have established their bifurcation diagram and estimated their velocity. More importantly, the stimulated Raman scattering breaks the reflection symmetry and destroys the homoclinic snaking bifurcation structure, allowing for isola stacks of dark localized states to form. This is in contrast with reversible systems that possess the reflection symmetry where the bifurcation diagram consists of two intertwined snaking curves.

The full LLE has been numerically simulated to demonstrate proof of isolas branches of solutions. As a function of the injected field strength, single peak and bounded states of localized branches of solutions have been constructed. Note that there have been reports of other type of localized structures with varying width [37,39,40]. These solutions arise from front interaction, need bistability between CWs for their formation, and exhibit a collapsed snaking type of bifurcation in their bifurcation structure. Contrastingly, the localized states described here are distinct in a number of ways: they have a finite size determined by the frequency that is the most unstable; their formation does not necessitate bistability; and their bifurcation diagram exhibits behavior akin to an isola stack. Finally, we have provided a geometrical interpretation of the impact of broken reflection symmetry mediated by the stimulated Raman scattering on the formation of isola stacks.

Declaration of competing interest

The authors declare that they have no known competing financial interests or personal relationships that could have appeared to influence the work reported in this paper.

Data availability

Data will be made available on request.

Acknowledgments

M.G.C. acknowledges the financial support of ANID– Millennium Science Initiative Program–ICN17-012 (MIRO) and FONDECYT project 1210353. K.P. acknowledges the support by the Fonds Wetenschappelijk Onderzoek-Vlaanderen FWO (G0E5819N) and the Methusalem Foundation. M.T acknowledges financial support from the Fonds de la Recherche Scientifique FNRS under Grant CDR no. 35333527 "Semiconductor optical comb generator". A part of this work was supported by the "Laboratoire Associé International" University of Lille - ULB on "Self-organisation of light and extreme events" (LAI-ALLURE)".

Compliance with ethics requirements

This article does not contain any studies with human or animal subjects.

Appendix

A.1. Derivation of the Swift–Hohenberg equation with delayed nonlocal response

The purpose of this section is to present the derivation of a Swift–Hohenberg with a delayed nonlocal response, i.e., the stimulated Raman scattering. To do that, we explore the fast-slow time dynamics of the generalized LLE Eq. (1), in the neighborhood of the critical point associated with nascent bistability. At this second-order critical point that marks the onset of a hysteresis loop, the output versus input characteristics have an infinite slope, i.e., $\partial E_i/\partial |E_s| = \partial^2 E_i/\partial |E_s|^2 = 0$ where $|E_s|$ is the CW solutions of Eq. (1) that satisfy $E_i^2 = |E_s|^2[1+(\Delta-|E_s|^2)^2]$. The coordinates of the critical point associated with bistability are [45]

$$E_c = (3-i\sqrt{3})\frac{E_{ic}}{4},\ E_{ic}^2 = \frac{8\sqrt{3}}{9},\ \text{and}\ \Delta_c = \sqrt{3}. \tag{10}$$

To explore the vicinity of the second-order critical point, we define a small parameter ϵ which measures the distance from the critical point associated with the bistability as

$$\Delta = \Delta_c + \delta\epsilon^2. \tag{11}$$

We then expand the input field amplitude, and the slowly varying intracavity electric field in terms of ϵ as

$$E_i = E_{ic} + s_1\epsilon + s_2\epsilon^2 + s\epsilon^3 + \cdots, \tag{12}$$

$$E = E_c + \epsilon(u_0, v_0) + \epsilon^2(u_1, v_1) + \epsilon^3(u_2, v_2) + \cdots \tag{13}$$

where u_i and v_i denote the real and the imaginary parts of the intracavity field. Our goal is to derive a slow time and slow space amplitude equation. A preliminary analysis indicates that we need to consider a small second-order dispersion coefficient $\beta_2 \equiv \epsilon\beta$ to have bounded solutions in both slow and fast time. We seek corrections to the steady states at criticality that depend on slow variables $t = \epsilon^2\zeta$ and $\tau = 3^{1/4}\epsilon T$. We assume in addition that the strength of the delayed Raman effect is small, i.e., $f_r \to f\epsilon^2$, and we set the β_4 value to one. Replacing the above expansions in the generalized Lugiato–Lefever Eq. (1), we obtain at the leading order in ϵ: $s_1 = 0$ and $u_0 = \sqrt{3}v_0$. At the next order ϵ^2, we obtain $s_2 = \sqrt{\delta/2\sqrt{3}}$. Finally at ϵ^3, we get

$$\frac{\partial u_0}{\partial t} = s + \left(\frac{\delta}{\sqrt{3}} - \frac{2f}{3}\right)u_0 - \frac{4}{3\sqrt{3}}u_0^3 \tag{14}$$

$$+ \frac{\beta}{\sqrt{3}}\frac{\partial^2 u_0}{\partial \tau^2} - \frac{1}{\sqrt{3}}\frac{\partial^4 u_0}{\partial \tau^4}$$
$$+ \frac{2af}{3}\int_{-\infty}^{\tau} e^{-\frac{\tau_0(\tau-\tau')}{\tau_2}}$$
$$\sin\left[\tau_0(\tau-\tau')/\tau_1\right] u_0(\tau')d\tau',$$

With the following changes of parameters $t \to 3^{3/2}t/4$, $\eta = (3^{3/2}/4)s$, $\mu = \sqrt{3}(\sqrt{3}\delta - 2f)/4$, and $\beta \to 3/4\beta$, we obtain the Swift–Hohenberg equation with stimulated Raman scattering Eq. (2), where the new kernel function is defined as $\phi(\tau) = \sqrt{3}/2af\exp^{-\tau_0(\tau-\tau')/\tau_2}\sin(\tau_0(\tau-\tau')/\tau_1)$.

References

[1] Jones DJ, Diddams SA, Ranka JK, Stentz A, Windeler RS, Hall JL, et al. Carrier-envelope phase control of femtosecond mode-locked lasers and direct optical frequency synthesis. Science 2000;288:635.

[2] Udem T, Holzwarth R, Hänsch TW. Optical frequency metrology. Nature 2002;416:233.

[3] Fortier T, Baumann E. 20 Years of developments in optical frequency comb technology and applications. Commun Phys 2019;2:1.

[4] Picqué N, Hänsch TW. Frequency comb spectroscopy. Nature Photon 2019;13:146.

[5] Herr T, Brasch V, Jost JD, Wang CY, Kondratiev NM, Gorodetsky ML, et al. Temporal solitons in optical microresonators. Nature Photon 2014;8:145.

[6] Kippenberg TJ, Gaeta AL, Lipson M, Gorodetsky ML. Dissipative Kerr solitons in optical microresonators. Science 2018;361:6402.

[7] Scroggie AJ, Firth WJ, McDonald GS, Tlidi M, Lefever R, Lugiato LA. Pattern formation in a passive Kerr cavity. Chaos Solitons Fractals 1994;4:1323.

[8] Tlidi M, Mandel P, Lefever R. Localized structures and localized patterns in optical bistability. Phys Rev Lett 1994;73:640.

[9] Nozaki K, Bekki N. Low-dimensional chaos in a driven damped nonlinear Schrödinger equation. Physica D 1986;21:381.

[10] Wabnitz S. Suppression of interactions in a phase-locked soliton optical memory. Opt Lett 1993;18:601.

[11] Matsko AB, Savchenkov AA, Liang W, Ilchenko VS, Seidel D, Maleki L. Mode-locked Kerr frequency combs. Opt Lett 2011;36:2845.

[12] Coen S, Randle HG, Sylvestre T, Erkintalo M. Modeling of octave-spanning Kerr frequency combs using a generalized mean-field Lugiato–Lefever model. Opt Lett 2013;38:37.

[13] Lugiato LA, Prati F, Gorodetsky M, Kippenberg TJ. From the Lugiato–Lefever equation to microresonator-based soliton Kerr frequency combs. Phil Trans R Soc A 2018;376:20180113.

[14] Bao H, Olivier L, Rowley M, Chu ST, Little BE, Morandotti R, et al. Turing patterns in a fiber laser with a nested microresonator: Robust and controllable microcomb generation. Phys Rev Res 2020;2:023395.

[15] Soto-Crespo JM, Akhmediev N, Grelu P, Belhache F. Quantized separations of phase-locked soliton pairs in fiber lasers. Opt Lett 2003;28:1757.

[16] Olivier M, Roy V, Piché M. Third-order dispersion and bound states of pulses in a fiber laser. Opt Lett 2006;31:580.

[17] Berrios-Caro E, Clerc MG, Leon AO. Flaming 2π kinks in parametrically driven systems. Phys Rev E 2016;94:052217.

[18] Tlidi M, Gelens L. High-order dispersion stabilizes dark dissipative solitons in all-fiber cavities. Opt Lett 2010;35:306.

[19] Tlidi M, Bahloul L, Cherbi L, Hariz A, Coulibaly S. Drift of dark cavity solitons in a photonic-crystal fiber resonator. Phys Rev A 2013;88:035802.

[20] Milian C, Skryabin DV. Soliton families and resonant radiation in a micro-ring resonator near zero group-velocity dispersion. Opt Express 2014;22:3732.

[21] Bahloul L, Cherbi L, Hariz A, Tlidi M. Temporal localized structures in photonic crystal fibre resonators and their spontaneous symmetry-breaking instability. Phil Trans R Soc A 2014;372:20140020.

[22] Turaev D, Vladimirov AG, Zelik S. Long-range interaction and synchronization of oscillating dissipative solitons. Phys Rev Lett 2012;108:263906.

[23] Akhmediev N, Karlsson M. Cherenkov radiation emitted by solitons in optical fibers. Phys Rev A 1995;51:2602.

[24] Skryabin DV, Gorbach AV. Colloquium: Looking at a soliton through the prism of optical supercontinuum. Rev Modern Phys 2010;82:1287.

[25] Vladimirov AG, Gurevich SV, Tlidi M. Effect of Cherenkov radiation on localized-state interaction. Phys Rev A 2018;97:013816.

[26] Vladimirov AG, Tlidi M, Taki M. Dissipative soliton interaction in Kerr resonators with high-order dispersion. Phys Rev A 2021;103:063505.

[27] Brasch V, Geiselmann M, Herr T, Lihachev G, Pfeiffer MHP, Gorodetsky ML, et al. Photonic chip–based optical frequency comb using soliton Cherenkov radiation. Science 2016;351:357.

[28] Spillane SM, Kippenberg TJ, Vahala KJ. Ultralow-threshold Raman laser using a spherical dielectric microcavity. Nature 2002;415:621.

[29] Lin G, Coillet A, Chembo YK. Nonlinear photonics with high- whispering-gallery-mode resonators. Adv Opt Photonics 2017;9:828.

[30] Min B, Yang L, Vahala K. Controlled transition between parametric and Raman oscillations in ultrahigh-Q silica toroidal microcavities. Appl Phys Lett 2005;87:181109.

[31] Liang W, Ilchenko V, Savchenkov A, Matsko A, Seidel D, Maleki L. Passively mode-locked Raman laser. Phys Rev Lett 2010;105:143903.

[32] Karpov M, Guo H, Kordts A, Brasch V, Pfeiffer MHP, Zervas M, et al. Raman self-frequency shift of dissipative Kerr solitons in an optical microresonator. Phys Rev Lett 2016;116:103902.

[33] Liu X, Sun C, Xiong B, Wang L, Wang J, Han Y, et al. Integrated high-Q crystalline AlN microresonators for broadband Kerr and Raman frequency combs. ACS Photonics 2018;5:1943.

[34] Chen-Jinnai A, Kato T, Fujii S, Nagano T, Kobatake T, Tanabe T. Broad bandwidth third-harmonic generation via four-wave mixing and stimulated Raman scattering in a microcavity. Opt Express 2016;24:26322.

[35] Zhu S, Shi L, Ren L, Zhao Y, Jiang B, Xiao B, Zhang X. Controllable Kerr and Raman-Kerr frequency combs in functionalized microsphere resonators. Nanophotonics 2019;8:2321.

[36] Cherenkov AV, Kondratiev NM, Lobanov VE, Shitikov AE, Skryabin DV, Gorodetsky ML. Raman-Kerr frequency combs in microresonators with normal dispersion. Opt Express 2017;25:31148.

[37] Clerc MG, Coulibaly S, Tlidi M. Time-delayed nonlocal response inducing traveling temporal localized structures. Phys Rev Res 2020;2:013024.

[38] Yao S, Bao C, Wang P, Yang C. Generation of stable and breathing flat-top solitons via Raman assisted four wave mixing in microresonators. Phys Rev A 2020;101:023833.

[39] Clerc MG, Coulibaly S, Parra-Rivas P, Tlidi M. Non-local Raman response in Kerr resonators: Moving temporal localized structures and bifurcation structure. Chaos 2020;30:083111.

[40] Parra-Rivas P, Coulibaly S, Clerc MG, Tlidi M. Influence of stimulated Raman scattering on Kerr domain walls and localized structures. Phys Rev A 2021;103:013507.

[41] Coen S, Tlidi M, Emplit P, Haelterman M. Convection versus dispersion in optical bistability. Phys Rev Lett 1999;83:2328.

[42] Odent V, Tlidi M, Clerc MG, Glorieux P, Louvergneaux E. Experimental observation of front propagation in a negatively diffractive inhomogeneous Kerr cavity. Phys Rev A 2014;90. 011806(R).

[43] Xue X, Xuan Y, Liu Y, Wang P-H, Chen S, Wang J, et al. Mode-locked dark pulse Kerr combs in normal-dispersion microresonators. Nat Photon 2015;9:594.

[44] Garbin B, Wang Y, Murdoch SG, Oppo G-L, Coen S, Erkintalo M. Experimental and numerical investigations of switching wave dynamics in a normally dispersive fibre ring resonator. Eur Phys J D 2017;71:240.

[45] Lugiato LA, Lefever R. Spatial dissipative structures in passive optical systems. Phys Rev Lett 1987;58:2209.

[46] Parra-Rivas P, Knobloch E, Gomila D, Gelens L. Dark solitons in the Lugiato–Lefever equation with normal dispersion. Phys Rev A 2016;93:063839.

[47] Parra-Rivas P, Gomila D, Knobloch E, Coen S, Gelens L. Origin and stability of dark pulse Kerr combs in normal dispersion resonators. Opt Lett 2016;41:2402.

[48] Kostet B, Gopalakrishnan S, Averlant E, Soupart Y, Panajotov K, Tlidi M. Vectorial dark dissipative solitons in Kerr resonators. OSA Continuum 2021;4:1564.

[49] Kostet B, Soupart Y, Panajotov K, Tlidi M. Coexistence of dark vector soliton Kerr combs in normal dispersion resonators. Phys Rev A 2021;104:053530.

[50] Yulin AV, Skryabin DV, J. Russell P St. Four-wave mixing of linear waves and solitons in fibers with higher-order dispersion. Opt Lett 2004;29:2411.

[51] Demircan A, Bandelow U. Supercontinuum generation by the modulation instability. Opt Commun 2005;244:181.

[52] Dudley JM, Genty G, Coen S. Supercontinuum generation in photonic crystal fiber. Rev Modern Phys 2006;78:1135.

[53] Dudley JM, Taylor JR, editors. Supercontinuum generation in optical fibers. Cambridge University Press; 2010.

[54] Milian C, Gorbach AV, Taki M, Yulin AV, Skryabin DV. Solitons and frequency combs in silica microring resonators: Interplay of the Raman and higher-order dispersion effects. Phys Rev A 2015;92:033851.

[55] Chembo YK, Grudinin IS, Yu N. Spatiotemporal dynamics of Kerr-Raman optical frequency combs. Phys Rev A 2015;92:043818.

[56] Lin G, Chembo YK. Phase-locking transition in Raman combs generated with whispering gallery mode resonators. Opt Lett 2016;41:3718.

[57] Cherenkov A, Kondratiev N, Lobanov V, Shitikov A, Skryabin D, Gorodetsky M. Raman-Kerr frequency combs in microresonators with normal dispersion. Opt Express 2017;25:31148.

[58] Liu K, Yao S, Yang C. Raman pure quartic solitons in Kerr microresonators. Opt Lett 2021;46:993.

[59] Liu M, Huang H, Lu Z, Wang Y, Cai Y, Zhao W. Dynamics of dark breathers and Raman-Kerr frequency combs influenced by high-order dispersion. Opt Express 2021;29:18095.

[60] Liu M, Huang H, Lu Z, Zhou W, Wang Y, Cai Y, et al. Stimulated Raman scattering induced dark pulse and microcomb generation in the mid-infrared. New J Phys 2022;24:053003.

[61] Blow KJ, Wood D. Theoretical description of transient stimulated Raman scattering in optical fibers. IEEE J Quantum Electron 1989;25:2665.
[62] Lin Q, Agrawal GP. Raman response function for silica fibers. Opt Lett 2006;31:3086.
[63] Tlidi M, Mussot A, Louvergneaux E, Kozyreff K, Vladimirov AG, Taki M. Control and removal of modulational instabilities in low-dispersion photonic crystal fiber cavities. Opt Lett 2007;32:662.
[64] Parra-Rivas P, Gomila D, Gelens L. Coexistence of stable dark- and bright-soliton Kerr combs in normal-dispersion resonators. Phys Rev A 2017;95:053863.
[65] Vladimirov AG, Gurevich SV, Tlidi M. Effect of cherenkov radiation on localized-state interaction. Phys Rev A 2018;97:013816.
[66] Hariz A, Bahloul L, Cherbi L, Panajotov K, Clerc M, Ferré MA, et al. Swift-Hohenberg equation with third-order dispersion for optical fiber resonators. Phys Rev A 2019;100:023816.
[67] Mandel P, Georgiou M, Erneux T. Transverse effects in coherently driven nonlinear cavities. Phys Rev A 1992;46:4252.
[68] Tlidi M, Georgiou M, Mandel P. Transverse patterns in nascent optical bistability. Phys Rev A 1993;48:4605.
[69] Tlidi M, Kockaert P, Gelens L. Dark localized structures in a cavity filled with a left-handed material. Phys Rev A 2011;84:013807.
[70] Parra-Rivas P, Gomila D, Matías MA, Coen S, Gelens L. Dynamics of localized and patterned structures in the Lugiato–Lefever equation determine the stability and shape of optical frequency combs. Phys Rev A 2014;89:043813.
[71] Parra-Rivas P, Knobloch E, Gelens L, Gomila D. Origin, bifurcation structure and stability of localized states in Kerr dispersive optical cavities. IMA J Appl Math 2021;86:856.
[72] Pomeau Y. Front motion, metastability and subcritical bifurcations in hydrodynamics. Physica D 1986;23:3.
[73] Champneys AR. Homoclinic orbits in reversible systems and their applications in mechanics, fluids and optics. Physica D 1998;112:158.
[74] Woods PD, Champneys AR. Heteroclinic tangles and homoclinic snaking in the unfolding of a degenerate reversible Hamiltonian Hopf bifurcation. Physica D 1999;129:147.
[75] Gomila D, Scroggie AJ, Firth WJ. Bifurcation structure of dissipative solitons. Physica D 2007;227:70.
[76] Keller HB. Numerical solution of bifurcation and nonlinear eigenvalue problem. In: Application of bifurcation theory. Academic Press; 1977.
[77] Vladimirov AG, McSloy JM, Skryabin DV, Firth WJ. Two-dimensional clusters of solitary structures in driven optical cavities. Phys Rev E 2002;65:046606.
[78] Coullet P. Localized patterns and fronts in nonequilibrium systems. Int J Bifurcation Chaos 2002;12:2445.
[79] Jackson EA. Perspectives of nonlinear dynamics: Volume 1. Cambridge: Cambridge University Press; 1989.
[80] Wiggins S. Normally hyperbolic invariant manifolds in dynamical systems. Springer Science & Business Media; 1994.
[81] Poincaré H. Les Methodes Nouvelles de la Mecanique Celeste. Vol. III, Paris, 1899 reprint. New York: Dover; 1957.
[82] Coullet P, Riera C, Tresser C. Stable static localized structures in one dimension. Phys Rev Lett 2000;84:3069.
[83] Haudin F, Rojas RG, Bortolozzo U, Residori S, Clerc MG. Homoclinic snaking of localized patterns in a spatially forced system. Phys Rev Lett 2011;107:264101.
[84] Wadee MK, Coman CD, Bassom AP. Solitary wave interaction phenomena in a strut buckling model incorporating restabilisation. Physica D 2002;163:26.
[85] Beck M, Knobloch J, Lloyd DJ, Sandstede B, Wagenknecht T. Snakes, ladders, and isolas of localized patterns. SIAM J Math Anal 2009;41:936.
[86] Knobloch J, Lloyd DJ, Sandstede B, Wagenknecht T. Isolas of 2-pulse solutions in homoclinic snaking scenarios. J Dynam Differential Equations 23:93, 52011.
[87] Makrides E, Sandstede B. Predicting the bifurcation structure of localized snaking patterns. Physica D 2014;268:59.
[88] Nishiura Y, Watanabe T. Traveling pulses with oscillatory tails, figure-eight-like stack of isolas, and dynamics in heterogeneous media. Physica D 2022;440:133448.
[89] Burke J, Houghton SM, Knobloch E. Swift-Hohenberg equation with broken reflection symmetry. Phys Rev E 2009;80:036202.
[90] Parra-Rivas P, Gomila D, Leo F, Coen S, Gelens L. Third-order chromatic dispersion stabilizes Kerr frequency combs. Opt Lett 2014;39:2971.

4.1 Perspectives

In this work, we have performed a detailed numerical analysis of the formation of bright and dark solitons in a reduced non-local Swift-Hohenberg equation. More specifically, the effect of a reflection symmetry-breaking term was investigated: the Raman effect on the LSs. Additionally, these results have been represented in a detailed bifurcation diagram. Nevertheless, not all of the bifurcations present in the diagram were completely characterized. For instance, the traveling wave and most LSs lose stability before the saddle-node bifurcation at an unidentified bifurcation point. Thus, further work is needed in this direction. On the other hand, although the main results have been successfully confirmed on the original model, a more complete bifurcation diagram, showing the stability and all of the LSs, remains to be produced.

Chapter 5

Dissipative Soliton Combs with Spectral Filtering. (submitted to Physical Review A)

The previous chapter focused on the formation of dissipative solitons in optical resonators when a non-local term due to Raman scattering is incorporated into the Lugiato-Lefever equation. The integral form of this additional term poses several analytical and numerical difficulties. For instance, in the case of the numerical continuation, where a large system of equations needs to be solved, the addition of the integral term transforms the extremely sparse system into a dense system, increasing the computational cost in terms of both memory and time by orders of magnitude.

An alternative approach to deal with the integral form of a non-local operator is to represent it by an infinite Taylor series, also referred to as a gradient expansion [105]. Moreover, assuming that the kernel function is sufficiently localized, the expansion can be safely truncated and only the first few relevant terms can be kept. This way, the integral operator can be approximated by a few differential operators with coefficients that depend on the kernel. Consequently, the representation in terms of differential operators allows for a much easier analytical investigation and numerical characterization of the system. For this reason, this gradient approximation to a nonlocal operator has been widely preferred in studies of vegetation patterns [16, 106–108].

In what follows, we apply the alternative approach stated above to investigate the formation of solitons and patterns in a fiber ring resonator with a spectral filter. To justify the use of a truncated gradient expansion, the case of a large-bandwidth filter (or equivalently, a localized temporal filter) is considered. Starting from an infinite-dimensional Ikeda map, a partial differential equation is derived in the form of a Lugiato-Lefever equation with additional first and second derivative terms from the gradient approximation. Similarly, as in the previous chapter, a forced reflection symmetry breaking takes place, leading to the drift of both localized and periodic states. Furthermore, it is observed that, in the presence of the filter, the stability region of LSs is significantly reduced and, the Andronov-Hopf bifurcation point that gives rise to breathing solitons is shifted towards a larger pumping. Lastly, through numerical continuation, the persistence of the snaking bifurcation scenario in the presence of the diffusive term is revealed along with its destruction upon the addition of the reflection symmetry-breaking term.

Dissipative Soliton Combs with Spectral Filtering

M. Bataille-Gonzalez[a], M.G. Clerc[a], B. Kostet[b], Y. Soupart[b], and M. Tlidi[b]
[a]Departamento de Física and Millennium Institute for Research in Optics, Facultad de Ciencias Físicas y Matemáticas, Universidad de Chile, Casilla 487-3, Santiago, Chile
[b]Faculté des Sciences, Département de Physique, Université libre de Bruxelles (U.L.B.), C.P. 231, Campus Plaine, B-1050 Bruxelles, Belgium

***Abstract*—The paradigmatic Lugiato–Lefever model describes the electric field envelope in a ring cavity filled with a Kerr medium and driven by a coherent injected laser beam. This model is applied to the formation of frequency combs associated with localized structures in micro- and macro-driven resonators. Including temporal filtering, we derive, in the mean field limit, a generalized Lugiato–Lefever equation. Theoretically, we investigated the formation of periodic and localized structures resulting from the combined action of temporal spectral filtering effect together with Kerr nonlinearity, pumping, dissipation, and frequency detuning. We show that spectral filtering reduces the intensity of the output field and increases the period of traveling solutions. Similarly, the maximum intensity of moving localized structures, often called dissipative solitons, is reduced. In addition, we show that the threshold associated with breathers is shifted toward large input intensities and that the associated domain of existence is significatively reduced. Finally, we analyze the homoclinic bifurcation associated with the formation of localized structures.**

***Index Terms*—Modulational instability, dissipative solitons, Kerr combs, temporal spectral filtering**

I. Introduction

FREQUENCY combs generated by continuous-wave (CW) laser output in microcavity Kerr resonators have revolutionized many fields of science and technology [1]–[3]. Hänsch is credited with being the first to introduce and develop optical frequency combs. These are equally spaced coherent spectral lines [4]. Much attention has been paid to the formation of frequency combs associated with forming Kerr dissipative solitons (DS) of light that maintain their shape during propagation in optical microcavities [5], [6]. This simple optical device has a compact size, a high-quality factor, and allows for chip-scale production of frequency combs [7]–[10]. Kerr–Raman optical frequency combs were also experimentally observed [11]–[16].

From a fundamental point of view, the Lugiato–Lefever equation (LLE) [17] has led to the prediction and analysis of various phenomena, including the theoretical study of Kerr optical frequency comb generation using whispering gallery mode cavities or integrated ring resonators [18]. In particular, frequency combs as the spectral content of localized light structures were theoretically predicted in driven Kerr resonators before their invention [19], [20]. The link between these two objects in micro- and macro-resonators has been established in [21], [22] (See the review [23] in the theme issue [24]). Dissipative solitons are not necessarily stationary. They can exhibit temporal motion or oscillation. In particular, several mechanisms leading to their movement have been described in the literature. It has been shown that uniform soliton motion can be induced by Raman scattering [25]–[27], odd orders of dispersion [28], delayed feedback [29], or spectral filtering [30]–[34].

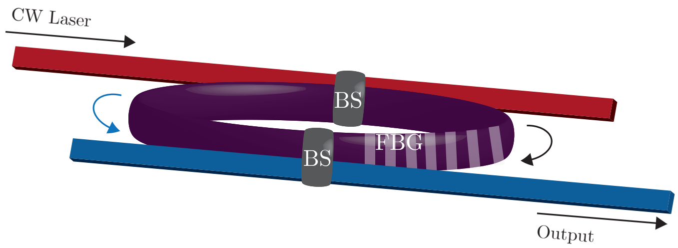

Fig. 1. Schematic setup of a driven ring resonator filled with Kerr media with the filter and driven by a coherent injected field. BS denotes a beam splitter, FBG is a fiber Bragg grating. The arrows account for the direction of light propagation.

The aim is to study the generation of dissipative soliton Kerr-combs under the influence of spectral filtering. We consider an optical cavity filled with a Kerr medium, driven by a coherent injected field, and with the inclusion of a temporal spectral filter (see Fig. I). Using a mean-field approximation, we reduce an infinite discrete map (Ikeda map) to the well-known Lugiato–Lefever equation with spectral filtering. A general filter transfer function is used for this derivation. We show that spectral filtering not only affects the coefficient of the second derivative but also produces a first derivative, whose coefficient is purely imaginary. In the second part, we study frequency combs, which are the spectral content of moving dissipative solitons. These solutions are generated due to the subcritical nature of the modulation instability. In this regime, the system undergoes a hysteresis loop involving the periodic moving and stable CW solutions. Moving dissipative solitons do not require bistability between the CW solutions and can be formed in the monostable regime (coexistence regime). We show that spectral filtering reduces the stability domain of the dissipative solitons. In the bistable regime, as the injected field increases, the system transitions from regular moving solitons to moving breathing ones We show that the spectral filtering shifts this transition towards large input intensities and hence stabilizes a regular motion of moving dissipative solitons. Finally, using a continuation algorithm, we show that the dissipative solitons form an isola that is not associated with a modulational instability threshold. This effect is attributed to spectral filtering, which breaks the reflection symmetry.

This paper is organized as follows. After briefly presenting a driven Kerr ring resonator with spectral filtering, we derive the mean field model, the generalized LLE (Sec. II). We present the linear stability analysis of the CW solutions and the temporal periodic structures that emerge from the modulational instability (Sec III). Regular moving dissipative structures are then evidenced in the subcritical modulational instability regime, along with their bifurcation diagrams for the monostable and bistable regimes (Sec. IV. A). The results of the continuation algorithm, which captures the homoclinic snaking bifurcation and isolas associated with dissipative solitons, are presented in Sec. IV. B. We conclude in Sec. V.

II. Lugiato–Lefever Equation with spectral filtering

A. *Integro-differential Lugiato–Lefever model*

We consider an optical cavity filled with a Kerr dispersive medium and driven by a coherent plane wave field, cf. Fig. I. Considering the Kerr effect and chromatic dispersion, light propagation in the cavity is governed by the nonlinear Schrodinger equation (NLSE)

$$\frac{\partial F}{\partial z} = i\beta_2 \frac{\partial^2 F}{\partial \tau^2} + i\gamma |F|^2 F, \tag{1}$$

where F is the slowly varying electric field envelope, z is the longitudinal coordinate along the propagation axis, τ is the time in a reference frame traveling at the group velocity of light in the Kerr material. We assume that the cavity operates with anomalous dispersion, assuming that the dispersion coefficient β_2 is positive. The nonlinear coefficient $\gamma = 2\pi n_2/\lambda_0$ with n_2 the nonlinear refractive index and λ_0 is the light wavelength in the vacuum.

In addition to the effects of dispersion and non-linearity, the field propagating inside the cavity undergoes coherent superposition with the input light beam at the cavity's input beam splitter. The cavity boundary conditions describe this process

$$F^{p+1}(0, z) = \theta F_i + \rho \exp(i\phi) h \otimes F^p(l, z), \tag{2}$$

where ρ and θ are the reflection and transmission coefficients at the output and the input beam splitter. The above equation provides a relation between the intracavity field envelope F^{p+1} at the input of the cavity after the $p+1$-th round-trip and the field $F^p(l, z)$ at the output after the p-th pass in the cavity, where l is the cavity length. The phase $\phi = 2\pi n l/\lambda_0$ represents the linear phase accumulated by the field during a round-trip time, t_r, with n as the refractive index. The evolution of the intracavity field is thus slow over the time scale of the order t_r. In Eq. (2), the symbol $\otimes$ denotes the convolution between the intracavity field F^p after p round-trip and the filter transfer function h.

The nonlinear Schrödinger Eq. (1) supplemented by the cavity boundary conditions, Eq. (2), constitutes an infinite dimensional map. To simplify the theoretical analysis of the problem, it is convenient to reduce this map to a single integrodifferential equation.

The temporal evolution can be considered continuous by replacing the map index p with a slow time scale t to model the evolution of the field envelope at the cavity entrance, i.e., the point $z = 0$. This can be achieved by defining the continuous variable $F(t, \tau)$ as the intracavity field envelope at $z = 0$, and continuous slow time $t = pt_r$ as

$$F(t = pt_r, \tau) = F(t, \tau) = F^p(z = 0, \tau), \tag{3}$$

where p is a positive integer number. The time t describes the slow evolution of the intracavity field from one round trip to another, while the structure of the intracavity field changes at the fast time scale τ. The slow-time derivative can be defined as

$$t_r \frac{\partial F(t = pt_r, \tau)}{\partial t} = F^{p+1}(z = 0, \tau) - F^p(z = 0, \tau). \tag{4}$$

The injected field is coupled to the cavity only if the system is close to resonance. This means that the intracavity field does not vanish when the system operates close to resonance where the phase shift ϕ is close to 2π.

By averaging the right-hand side of the NLSE Eq. (1) over one cavity length, we get

$$\begin{aligned} F^p(l, \tau) &= F^p(0, \tau) + i\frac{\beta_2 l}{2} \frac{\partial^2 F^p(0, \tau)}{\partial \tau^2} \\ &+ i\gamma l |F^p(0, \tau)|^2 F^p(0, \tau). \end{aligned} \tag{5}$$

By taking into account both continuous-time Eq. (3), i.e., $F^p(0, \tau) = F(t, \tau)$ and its derivative Eq. (4), i.e., $\partial_t F(t = pt_r, \tau) = \partial_t F(t, \tau)$, and by replacing the field amplitude $F^p(l, \tau)$ that appear in Eq. (5) in the boundary conditions Eq. (4), we obtain

$$\begin{aligned} t_r \frac{\partial F(t, \tau)}{\partial t} &= \theta F_i - F(t, \tau) + \rho \exp(i\phi) \Big[h \otimes F(t, \tau) \\ &+ \frac{i\beta_2 l}{2} h \otimes \frac{\partial^2 F(t, \tau)}{\partial \tau^2} \\ &+ i\gamma l h \otimes |F(t, \tau)|^2 F(t, \tau) \Big]. \end{aligned} \tag{6}$$

This equation is an integrodifferential equation containing three convolution terms obtained from an infinite-dimensional map Eqs. (1, 2) by averaging over a cavity length and by introducing a continuous time and its derivative.

B. *Mean-field approximation: the Lugiato–Lefever model with spectral filtering*

To describe the evolution of the intracavity field, we use the mean-field approach to further simplify the integrodifferential equation Eq. (6) into a partial differential equation. Before applying the mean-field approximation, let us first evaluate the three convolutions that appear in Eq. (6). The term $h \otimes F(l, \tau)$ is given by

$$h \otimes F = \int \mathcal{F}[h_r + ih_i] F(t - \tau) d\tau, \tag{7}$$

where the complex filter transfer function in the frequency space $h = h_r + ih_i$, and $\mathcal{F}$ is the Fourier transform

$$\mathcal{F}[h_r + ih_i] = \frac{1}{2\pi}\int \exp\left(-i\omega\tau\right)[h_r(\omega) + ih_i(\omega)]d\omega. \quad (8)$$

Expanding the term $F(t-\tau)$ in a Taylor series, one gets

$$\begin{aligned} h \otimes F &= \int \left(\mathcal{F}[h_r] + i\mathcal{F}[h_i]\right) \sum_{n=0}^{\infty} (-1)^n \frac{\tau^n}{n!}\frac{\partial^n F(t)}{\partial \tau^n} d\tau, \\ &= \sum_{n=0}^{\infty} a_n \frac{\partial^n F}{\partial \tau^n} + i \sum_{n=0}^{\infty} b_n \frac{\partial^n F}{\partial \tau^n}, \end{aligned} \quad (9)$$

the coefficients a_n and b_n are

$$a_n = (-1)^n \int \mathcal{F}[h_r(\tau)]\frac{\tau^n}{n!}d\tau, \quad (10)$$

$$b_n = (-1)^n \int \mathcal{F}[h_i(\tau)]\frac{\tau^n}{n!}d\tau. \quad (11)$$

The above coefficients are well-defined for functions $\mathcal{F}[h(\tau)]$ that decay faster than a polynomial. Our analysis until now is general; we do not specify the temporal shape of the filter transfer function. If we assume that the real and imaginary parts of h are an odd and even function of frequency, then $a_{2n+1} = 0$ and $b_{2n} = 0$. Given this restriction, the first-order expansion in n yields

$$h \otimes F = (h_r + ih_i) \otimes F \approx a_0 F + a_2 \frac{\partial^2 F}{\partial \tau^2} + ib_1 \frac{\partial F}{\partial \tau}. \quad (12)$$

A similar calculation leads to the evaluation of the two other convolutions in the integrodifferential Eq. (6), namely

$$h(\omega) \otimes \frac{\partial^2 F}{\partial \tau^2} \approx c_0 \frac{\partial^2 F}{\partial \tau^2} + ic_1 \frac{\partial^3 F}{\partial \tau^3}, \quad (13)$$

$$h(\omega) \otimes |F|^2 F \approx d_0 |F|^2 F + id_1 \frac{\partial |F|^2 F}{\partial \tau}. \quad (14)$$

By replacing the three convolution terms Eqs. (12,13,14) in the integrodifferential equation Eq. (6), and applying the mean-field approximation consisting of the following assumptions: (i) We restrict our analysis to high-finesse cavities. This means that the transmission coefficient θ is assumed to be much smaller than unity $\theta \ll 1$, so that the reflection coefficient is $\rho \approx 1 - \theta^2/2$, (ii) the linear phase shift acquired by the light is small $\phi \ll 1$ over length l, so that $\exp(i\phi) \approx (1 + i\phi)$, (iii) the nonlinear phase shift must be smaller than unity, i.e., $\gamma l |F|^2 \ll 1$. (iv) The cavity length is much shorter than the characteristic dispersion length of the field. Under these approximations, the integrodifferential equation (6) leads to a partial-differential equation often referred to as the generalized Lugiato–Lefever equation (GLLE):

$$\begin{aligned} t_r \frac{\partial F}{\partial t} &= \theta F_i - F + (1 - \frac{\theta^2}{2} - i\phi) a_0 F \\ &+ \frac{a_2}{2}\frac{\partial^2 F}{\partial \tau^2} + ib_1 \frac{\partial F}{\partial \tau} + \frac{i\beta_2 l}{2}\Big[c_0 \frac{\partial^2 F}{\partial \tau^2} + ic_1 \frac{\partial^3 F}{\partial \tau^3}\Big] \\ &+ i\gamma l \Big[d_0 |F|^2 F + id_1 \frac{\partial |F|^2 F}{\partial \tau}\Big]. \end{aligned} \quad (15)$$

This mean-field equation is quite general in that we do not explicitly specify the form of the transfer function of the filter; we simply require that the real part of the $h(\omega)$ function be an odd function and the imaginary part an even function of frequency. More specifically, let us consider the higher-order Lorentzian filter [30], [31]

$$h_r(\omega) = \frac{ba^4}{(\omega - \omega_f)^4 + a^4}, \quad (16)$$

$$h_i(\omega) = \frac{ab(\omega - \omega_f)[(\omega - \omega_f)^2 + a^2]}{(\omega - \omega_f)^4 + a^4}, \quad (17)$$

where the parameters a and b are linked to the filter bandwidth and the filter strength, respectively. ω_f denotes the frequency of the filter. We can further simplify the generalized mean-field LLE by assuming that the filter bandwidth is large $a \gg 1$, then the coefficient associated with the imaginary part of the filter transfer function in Eq. (15) appears in the second order, namely $c_1 \ll 1$ and $d_1 \ll 1$. Under these approximations, the Eq. (15) becomes

$$\begin{aligned} t_r \frac{\partial F}{\partial t} &= \theta F_i - (1 - a_0 + \frac{\theta^2}{2} + i\phi a_0)F + i\gamma l d_0 |F|^2 F \\ &+ ib_1 \frac{\partial F}{\partial \tau} + \left(a_2 + \frac{i\beta_2 l c_0}{2}\right)\frac{\partial^2 F}{\partial \tau^2} \end{aligned} \quad (18)$$

To reduce the number of parameters describing the time evolution of the intracavity field, we introduce the following scaling and renormalization:

$$\begin{aligned} (E, E_i) &= (F, \theta F_i)\frac{\gamma l d_0}{1 - a_0}, \quad t \to \frac{\kappa}{t_r} t, \\ (\delta, \beta, \alpha_1, \alpha_2) &= (2a_0\phi, \beta_2 l c_0, 2b_1, a_2)/2\kappa, \\ \kappa &= 1 - a_0 + \theta^2/2. \end{aligned} \quad (19)$$

Under these changes, the generalized LLE Eq. (18) takes its dimensionless form

$$\begin{aligned} \partial_t E &= E_i - (1 + i\delta)E + i|E|^2 E \\ &+ i\alpha_1 \frac{\partial E}{\partial \tau} + (\alpha_2 + i\beta)\frac{\partial^2 E}{\partial \tau^2}, \end{aligned} \quad (20)$$

Taking into account the temporal or spatial filters associated with gain dispersion or diffusion, respectively, in the modeling of the ring cavity filled with Kerr media implies considering not only a diffusive term; $\alpha_2 \partial_\tau^2 E$; as in [32], [33], [35], but also the first derivative whose coefficient is complex; $i\alpha_1 \partial_\tau E$.

III. Linear stability analysis and modulational instability

A. Linear stability analysis

The homogeneous stable states (HSS) of Eq. (20) are $E_i^2 = |E_s|^2[1 + (|E_s|^2 - \delta)^2]$. They are independent of the parameters $\alpha_{1,2}$, and the HSS are therefore unaffected by the spectral filtering effect. For $\delta < \sqrt{3}$ ($\delta > \sqrt{3}$), the transmitted intensity as a function of the input intensity E_i^2 is monostable (bistable). With periodic boundaries, we consider small fluctuations $\exp(\lambda_\omega t + i\omega\tau)$ around the homogeneous steady state E_s, where the frequency ω verifies the relation $(\partial_\omega^2 + \omega^2)\exp(i\omega\tau) = 0$. This formulation leads to a characteristic equation which is quadratic in λ and whose coefficients are functions of ω^2 and the system parameters:

$$\begin{aligned} \lambda^2 &+ 2(1 + \alpha_1\omega + \alpha_2\omega^2)\lambda + (1 + \alpha_1\omega + \alpha_2\omega^2)^2 \\ &+ (2I_s - \delta - \beta\omega^2)^2 - I_s^2 = 0, \end{aligned} \quad (21)$$

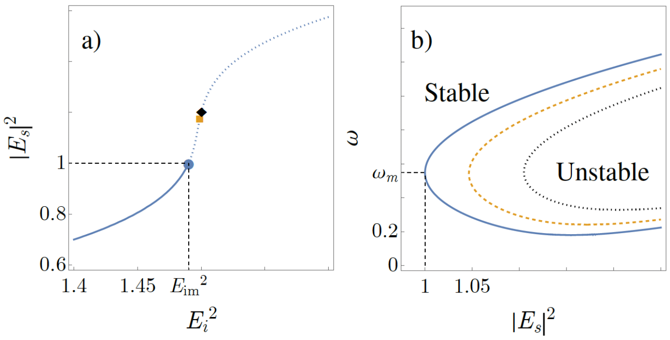

Fig. 2. a) Homogeneous steady states of Eq. (20) in the monostable case for anomalous dispersion where the threshold of the modulational instability is shown with markers for different values of $\alpha_1 = \alpha_2 = \alpha$. The blue dot corresponds to $\alpha = 0$, the orange square to $\alpha = 0.05$, and the black diamond to $\alpha = 0.1$. b) Marginal stability curve for the frequency as a function of the homogeneous steady state intensity. The blue full line corresponds to $\alpha = 0$; the orange dashed to $\alpha = 0.05$, and the black dotted line to $\alpha = 0.1$. Other parameters are $\delta = 1.7$, $\beta = 1$.

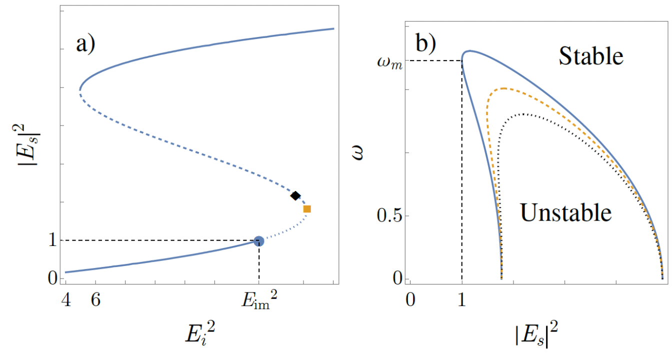

Fig. 3. a) Homogeneous steady states of Eq. (20) in the bistable case for normal dispersion where the threshold of the modulational instability is shown with markers for different values of $\alpha_1 = \alpha_2 = \alpha$. The blue dot corresponds to $\alpha = 0$, the orange square to $\alpha = 0.05$, and the black diamond to $\alpha = 0.1$. b) Marginal stability curve for the frequency as a function of the homogeneous steady state intensity. The blue full line corresponds to $\alpha = 0$; the orange dashed line to $\alpha = 0.05$, and the black dotted line to $\alpha = 0.1$. Other parameters are $\delta = 5$, $\beta = -1$.

where $I_s = |E_s|^2$. The solutions of this equation reads

$$\lambda_{1,2} = -\left(1 + \alpha_1\omega + \alpha_2\omega^2\right) \pm \sqrt{I_s^2 - (2I_s - \delta - \beta\omega^2)^2}. \tag{22}$$

In the Fourier space, unstable modes are characterized by a finite range of frequencies excluding the origin. This range must exclude all large periods (small frequency) corresponding to quasi-uniform distributions and very short periods (large frequency). They ensure that temporal fluctuations of arbitrarily small and large frequencies are damped. The well-known temporal modulational instability occurs when the eigenvalue corresponding to ω_m changes sign and becomes positive. This dispersion relation determines the critical point associated with modulational instability provided that $\lambda_\omega(\omega_m) = 0$ and $\partial_\omega\lambda_\omega(\omega_m) = 0$. The first condition leads to the marginal stability curve

$$(1 + \alpha_1\omega + \alpha_2\omega^2)^2 + (2I_s - \delta - \beta\omega^2)^2 = I_s^2. \tag{23}$$

In the absence of spectral filtering, i.e., $\alpha_1 = \alpha_2 = 0$, we recover the well-known critical frequency and threshold for the modulational instability: $|E_m|^2 = 1$ and $\omega_m^2 = 2 - \delta$ obtained for $\beta = 1$ [17]. When $\alpha_1 \neq 0$ and $\alpha_2 \neq 0$, the threshold and critical frequency expressions at the modulation instability threshold are cumbersome. In the particular case, $\alpha_1 = 0$

$$\omega_m^2 = \frac{\beta(2|E_m|^2 - \delta) - \alpha_2}{\alpha_2^2 + \beta^2}, \tag{24}$$

where $|E_m|^2$ is the critical intensity at the onset of the bifurcation and is given by

$$|E_m|^2 = \frac{2\alpha_2 \pm (\alpha_2\delta - \beta)\sqrt{\alpha_2^2 + \beta^2}}{3\alpha_2^2 - \beta^2}. \tag{25}$$

Let us first consider the anomalous dispersion regime where the chromatic dispersion coefficient is positive, i.e., $\beta > 0$ and focus on the monostable case where the output is a single-valued function of the injected field amplitude, i.e., $\delta < \sqrt{3}$. Fig. 2 shows the input-output characteristics and the marginal stability curves for different values of α_1 and α_2. The threshold associated with modulational instability is shifted towards a higher injected field strength, indicating that the spectral filter tends to stabilize the homogeneous steady states as shown in Fig. 2a).

The most unstable frequency becomes smaller as the α_2 parameter is increased, and obviously, the period of temporal structures emerging from the modulatory instability increases with the α_2 parameter, as shown in Fig. 2. In the monostable regime i.e., $\delta < \sqrt{3}$, we see the threshold associated to the modulational instability is increased with the spectral filtering coefficients.

In the bistable regime, two intervals of the frequency detuning parameter are considered:

- When $\sqrt{3} < \delta < -\alpha_2 + 2(\alpha_2^2 + 1)^{1/2}$, a small portion of the lower homogeneous steady states is affected by the modulational instability (MI), namely in the range

  $$|E_m|^2 < |E_s|^2 < \frac{\delta + \alpha_2}{2}, \tag{26}$$

  For $\delta = -\alpha_2 + 2(\alpha_2^2 + 1)^{1/2}$, the MI threshold coincides with the lower limit point associated with bistability. The lower homogeneous state is unstable for all values of the input injection. Note that in the absence of spectral filtering, i.e., when $\alpha_1 = \alpha_2 = \alpha = 0$, we recover the frequency range for which a portion of unstable mode falls in the range $\sqrt{3} < \delta < 2$.
- When $\delta > -\alpha_2 + 2(\alpha_2^2 + 1)^{1/2}$, the lower homogeneous solution is stable, and the upper homogeneous steady state is always stable with respect to the modulational instability. Figure 3b) shows the marginal stability curve for this regime.

In the normal dispersion regime where the chromatic dispersion coefficient is negative , i.e., $\beta < 0$, the MI does not affect the monostable regime. However, in the bistable case, a small portion of the lower homogeneous steady states becomes modulationally unstable. When increasing the strength of spectral

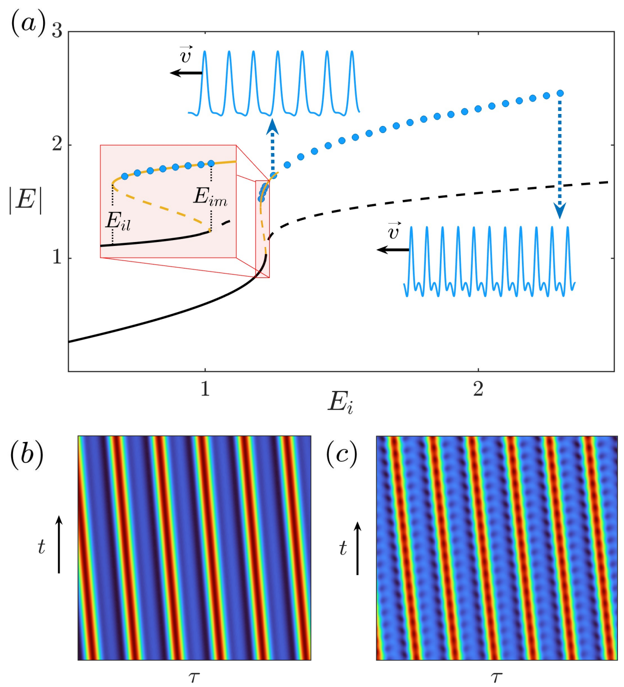

Fig. 4. Bifurcation diagram obtained in the monostable case. (a) The amplitude of the intracavity field as a function of the amplitude of the injected field. The black curve represents the CW solutions. The solid (dashed) line indicates stable (unstable) with respect to modulational instability. The blue dots indicate the maximum amplitude of moving periodic structures. The modulational instability appears to be subcritical. A hysteresis loop exists in the range $E_{il} < E_i < E_{im}$ between stable CW solutions and moving periodic structures. A continuation algorithm generates the unstable and stable mustard curves resulting from the modulation instability, while the blue dots correspond to direct numerical simulations of Eq. (20). (b,c) The $\tau - t$ maps obtained for $E_i = 2.3$ and $E_i = 2.39$, respectively, associated with regular moving periodic structures and breathing structures. Other parameters are $\delta = 1.7$, $\beta = 1$, $\alpha_1 = 0.1$ and $\alpha_2 = 0.1$.

filtering, both states forming the hysteresis loop of the bistable output-input characteristics become modulationally stable, as shown in Fig. 3.

B. Temporal periodic structures

As the input field increases, the flat solution becomes modulationally unstable, and the output field spontaneously develops a periodic structure with a well-defined frequency or period. This solution is of finite amplitude and is represented by full points in Fig. 4a). Using the implicit Euler algorithm scheme, they are obtained from numerical simulations of the mean-field model Eq. (20). Numerically, this is done using periodic boundary conditions compatible with the resonator geometry in Fig. I. The grid size is 500 with a temporal step integration size of 0.1. We consider the monostable regime where the homogeneous steady state solutions (CW solution) is a single-valued function of the injection beam [see the black curve of Fig. 4a)]. This solution is stable until the threshold denoted by $E_i = E_{im}$. Above this threshold, the CW solutions become unstable and develop spontaneously moving periodic structures. An example of this solution is plotted in the $\tau - t$ map in Fig. 4b). The amplitude of regular moving periodic solutions as a function of the input amplitude is indicated by blue dots in the bifurcation diagram of Fig. 4a). When the input field intensity is decreased, the periodic solution remains stable even for $E_i < E_{im}$. These traveling solutions are stable in the subcritical domain, typically in the range of $E_{il} < E_i < E_{im}$ as shown in Fig. 4a). The branch of moving periodic solution emerges from the modulational instability and is connected to the CW solution by unstable solutions represented by a dashed line as shown in the zoom of Fig. 4a). These unstable and stable branches of solutions are obtained by the pseudo-arclength continuation method, which allows the plotting of both stable and unstable periodic traveling solutions (mustard curves). As the input field is increased beyond the threshold of modulational instability, the output of the resonator evolves from regular to breathing self-pulsating structures. These solutions are moving with speed v. The $\tau - t$ map in Fig. 4c) shows examples of the temporal profiles of the breathing solutions. These solutions are moving with speed v, and their temporal profiles are shown in Fig. 4a). The motion is directly attributed to the presence of spectral filtering, which generates through mean-field modeling a term $i\alpha_1\partial_\tau E$ in the generalized LLE model Eq. (20). From dynamical system theory, the presence of this term breaks the reflection symmetry $\tau \to -\tau$ and makes the solution obviously moving. The existence of a parameter regime in which CW solutions coexist with a moving train of periodic solutions is a prerequisite for the formation of stable light confinement in optical resonators [36], which will be discussed in the next section.

IV. Dissipative Soliton Combs with Filtering

A. Moving and Breathing Dissipative Soliton

Kerr micro- and macro-resonators support temporal dissipative solitons in the normal dispersion regime where the modulational instability appears subcritically. Their formation does not require a bistability between CW solutions. They can be generated in the monostable regime in the range $\delta < \sqrt{3}$. We consider the input field amplitude domain $E_{il} < E_i < E_{im}$, which gives rise to a hysteresis loop involving the CW solution and the traveling periodic solutions (see the zoom of Fig. 4a). As we shall see, different types of localized solutions exist as stable solutions associated with this domain. Numerical simulations of the generalized LLE model Eq. (20) show evidence of dissipative solitons. The results are summarized in Fig. 5. When $\alpha = 0$, LSs are stationary and symmetric solutions [see Fig. 5b)]. Their range of existence as stable solutions, indicated by full squares, is rather large, as shown in Fig. 5a). From this chart, we see that as the spectral filter parameters increase, the dissipative solitons stability range is reduced. In addition, we plot together with the points corresponding to the localized states for $\alpha_1 = 0.1$, the branch of the periodic solutions moving that connects to the CW solution by an unstable solution represented by a dotted line as shown in Fig. 5a). The branches of the periodic solutions in motion for $\alpha = 0$ and $\alpha = 0.05$ are not shown in Fig. 5a) for readability. The unstable and stable branches of the periodic solutions are obtained using the pseudo-arclength continuation method. The stable branch of the moving periodic

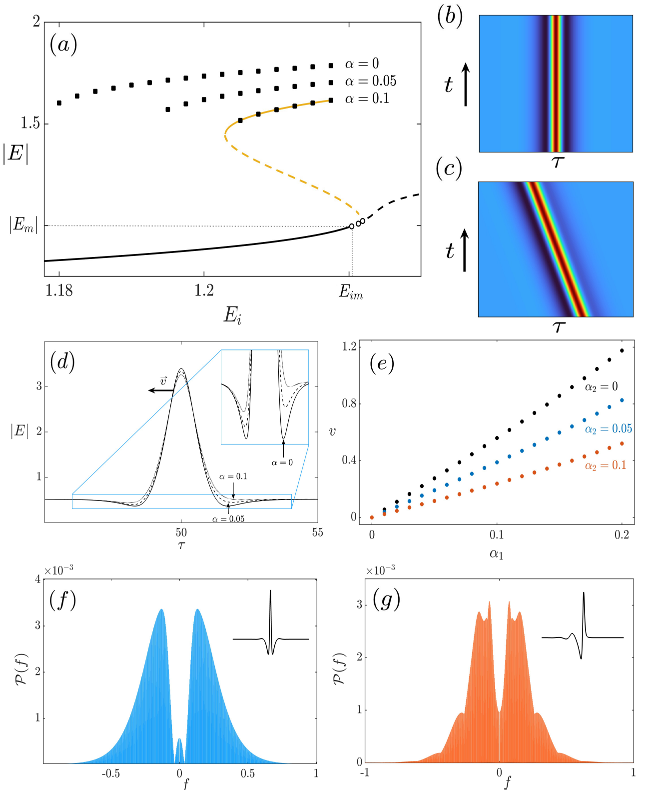

Fig. 5. Moving dissipative solitons obtained in the monostable case. (a)The maximum amplitude of the intracavity field associated with dissipative solitons as a function of the amplitude of the injected field. The black curve represents the CW solutions. As the input field increases, the CW solutions become unstable with respect to modulational instability. The black circles on this curve represent the threshold associated with modulational instability for $\alpha = 0$, $\alpha = 0.05$, and $\alpha = 0.1$. The solid (dashed) line indicates stable (unstable) with respect to modulational instability. The three curves formed by black squares obtained for $\alpha = 0$, $\alpha = 0.05$ and $\alpha = 0.1$ show the maximum amplitude of moving dissipative structures. (b) The $\tau - t$ maps obtained for $E_i = 1.21$, $\alpha_1 = 0$, and $\alpha_2 = 0.1$ associated with stationary dissipative soliton. (b) The $\tau - t$ maps obtained for $E_i = 1.21$, $\alpha_1 = 0.2$, and $\alpha_2 = 0.1$ associated with moving dissipative soliton. (d) A zoom-in on the dissipative solitons profile shows the deformation of the soliton tails for different values of the filter parameters. (e) The speed of dissipative solitons for a fixed amplitude of the injected field amplitude as a function of the parameter α_1. (f,g) The combs associated with the stationary and moving dissipative solitons shown in (b) and (c), respectively. Other parameters are $\delta = 1.7$, and $\beta = 1$.

solution coincides with the localized branch of the solutions represented by the black dots. However, as we shall see, unlike the periodic solutions, the localized solutions branch is not connected to the CW solution.

In addition, when $\alpha_1 \neq 0$, the localized peaks become asymmetric and begin to exhibit regular motion, as shown in the $\tau - t$ map in Fig. 5c). The profile of a single peak dissipative soliton is shown in Fig. 5d). The dissipative soliton has an exponentially decaying tail. As the parameter α_1 increases, the tail of the dissipative solitons becomes asymmetric due to the breaking of the $\tau \rightarrow -\tau$ reflection symmetry of the system, as shown in the zoom of Fig. 5d). The motion is then due to the presence of temporal spectral filtering inside the cavity. The speed of single peak dissipative solitons as a function of the parameter α_1 is plotted in Fig. 5e). The speed increases with the parameter α_1 and decreases with α_2. The Fourier transform

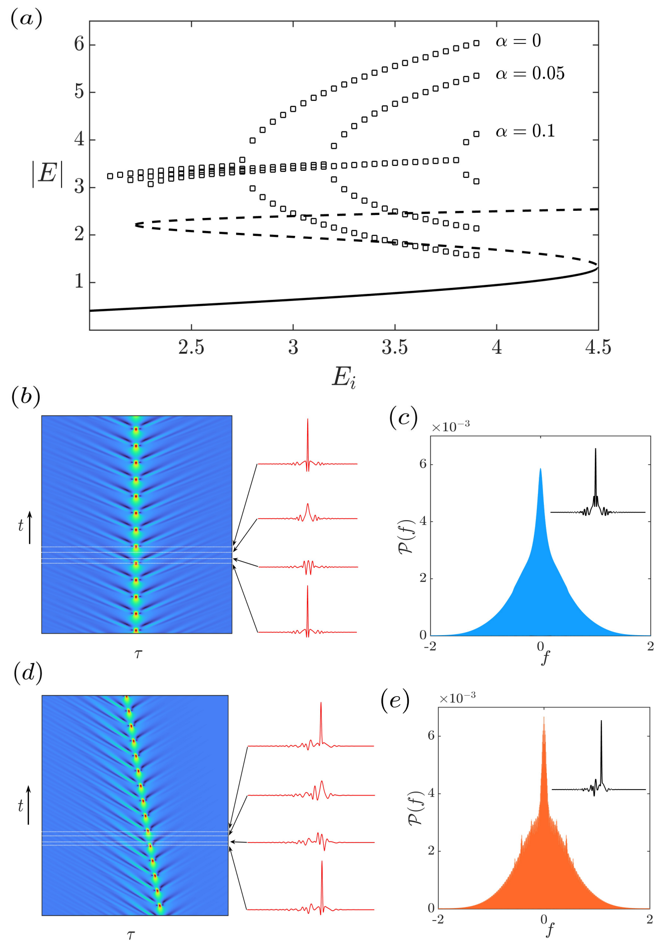

Fig. 6. Moving and breathing dissipative solitons obtained in the bistable case. (a) The maximum amplitude of the intracavity field associated with dissipative solitons as a function of the amplitude of the injected field. The black curve represents the CW solutions. The lower branch shown is always stable for $\delta = 5$, and the upper CW solution denoted by the dotted line is always unstable. The three curves formed by black squares obtained for $\alpha_{1,2} = 0$, $\alpha_{1,2} = 0.05$ and $\alpha_{1,2} = 0.1$ show the maximum amplitude of moving dissipative structures. As the injected field amplitude is increased, the moving dissipative soliton branch exhibits a pitchfork bifurcation. Above this bifurcation, the DSs begin to breathe. The two branches emerging from this bifurcation represent the maximum and minimum amplitudes associated with the breathing dissipative solitons. (b) The $\tau - t$ maps obtained for $E_i = 3.9$, $\alpha_{1,2} = 0$. associated with breathing dissipative soliton. (d) The $\tau - t$ maps obtained for $E_i = 3.9$, $\alpha_1 = 0.2$, and $\alpha_2 = 0.03$ associated with moving breathing dissipative soliton. (c,e) The combs associated with stationary and moving dissipative solitons are shown in (b) and (d), respectively. Parameters are $\delta = 5$ and $\beta = 1$.

of the train of localized structures corresponding to Fig. 5b) and exiting the resonator is plotted in Fig. 5f). Similarly, the Fourier transform of the moving localized structures shown in 5c) is plotted in Fig. 5e). When the amplitude of the input field is increased in the monostable regime, localized breathing solutions are unstable because the background, the CW solution, becomes modulationally unstable.

We now consider the bistable regime $\delta > \sqrt{3}$. The linear stability analysis shows that the lower CW solutions become stable when considering spectral filtering. We fix the detuning parameter to $\delta = 5$, and we vary the input field amplitude. In the absence of spectral filtering $\alpha_{1,2} = 0$, numerical

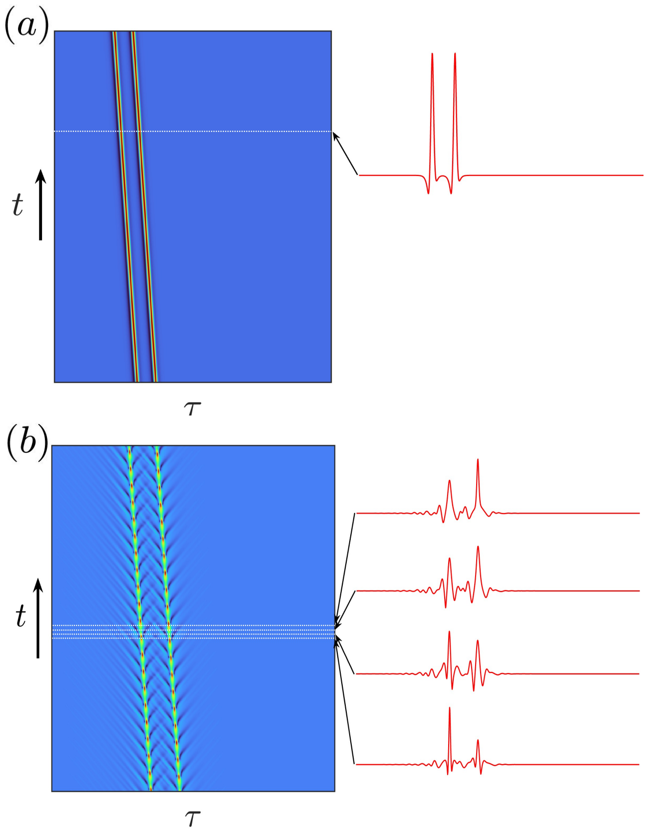

Fig. 7. Bounded dissipative solitons in the presence of spectral filtering. (a)bounded moving dissipative solitons and (b) bounded moving and breathing dissipative solitons obtained for the same parameters of Fig. 6b) and Fig. 6d), respectively.

simulations of the generalized LLE Eq. (20) show stationary dissipative solitons (the branch of open black squares in Fig. 6a). These regular dissipative solitons are stationary solutions similar to those shown in the monostable case [see Fig. 5b)]. When the input field is increased, DSs start to exhibit breathing behavior. An example is shown in Fig. 6b). The corresponding comb is plotted in Fig. 6c). When taking into account spectral filtering, $\alpha \neq 0$, the breathing solitons start to move with a constant speed as shown in Fig. 6d), and the corresponding combs are plotted in 6e).

Kerr micro- and macro-resonators can host bounded moving solutions. Fig. 7a) shows an example of two bounded moving dissipative solitons. Breathing and moving bounded dissipative solitons are also stable solutions of the generalized LLE model Eq. (20). This solution is shown in Fig. 7b). Dissipative solitons interact via their exponentially decaying tails and form bounded states. This weak interaction can be strongly affected by various perturbations, such as periodic modulation [37], [38] and high-order dispersions [28], [39]. These perturbations lead to the appearance of the so-called soliton Cherenkov radiation at the soliton tails [40], [41]. A deeper investigation of interaction in the presence of filtering will be the subjet of future publication.

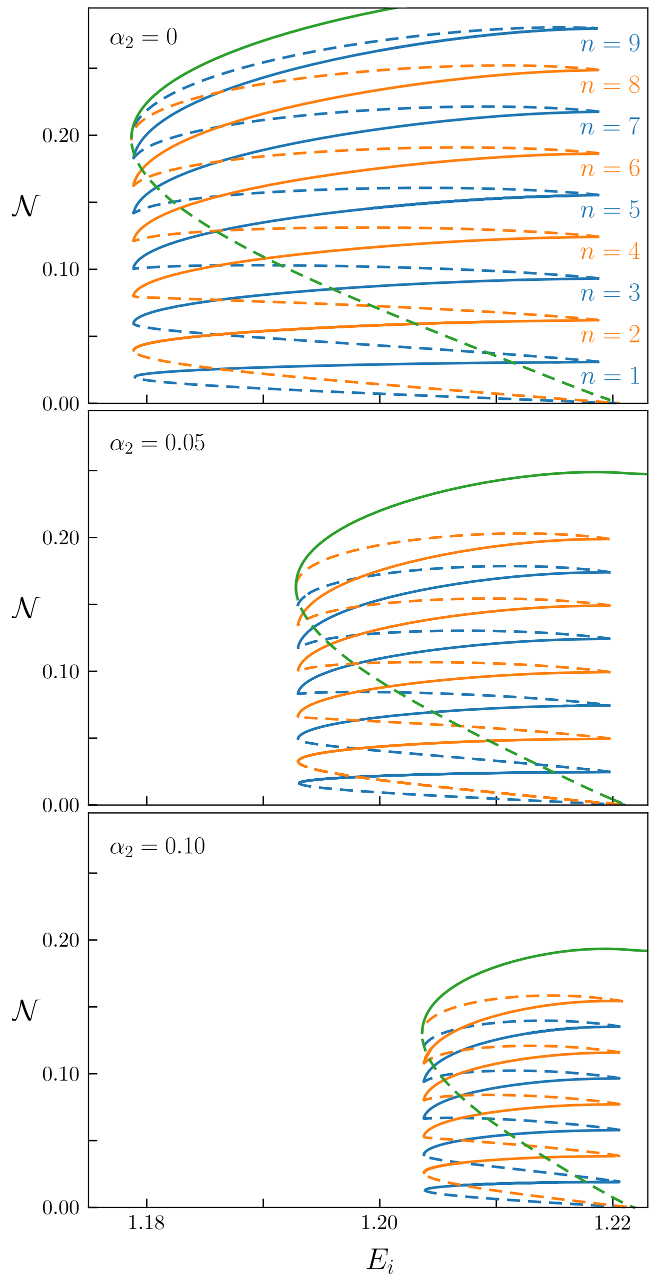

Fig. 8. Bifurcation diagram showing the L2-norm $\mathcal{N} = \int d\tau |E - E_s|^2$ as a function of the injection amplitude E_i. Green lines indicate periodic solutions, while (orange) blue lines indicate (even) odd numbers of peaks in localized states. Full (dashed) lines correspond to stable (unstable) states, respectively. Parameters are $\delta = 1.7$, $\beta = 1$, $\alpha_1 = 0$.

B. Homoclinic snaking bifurcation and isolas of dissipative solitons

Kerr resonator exhibits a high degree of multistability over a finite range of injected field amplitude values, often referred to as the pinning region [42]. More precisely, the generalized LLE model Eq. (20) supports not only two peaks solutions bounded together but an infinite set of odd and even localized peaks. Let us first assume that $\alpha_1 = 0$, in this case, Eq. (20) admits a set of stationary solutions characterized by $2n+1$ and $2n$ peaks, where n is a positive integer. They are motionless solutions when $\alpha_1 = 0$ because the generalized LLE model Eq. (20) conserves the reflection symmetry $\tau \to -\tau$. Dissipative solitons exhibit a well-known homoclinic snaking type of bifurcation within the subcritical modulational instability range. In the time domain, their bifurcation diagram consists of two snaking curves that are connected and emerge from the modulational instability threshold [43], [44]. Since the maximum amplitudes of DSs with different numbers of peaks are close to each other, it is more convenient to plot the L2-norm

$$\mathcal{N} = \int d\tau |E - E_s|^2 \tag{27}$$

as a function of injected field amplitude. The homoclinic snaking bifurcation is shown in Fig. 8. The two snaking curves associated with odd and even numbers of localized peaks are intertwined. They correspond with the back-and-forth oscillations across the pinning region. This feature has been abundantly addressed for the Lugiato–Lefever model without spatial filtering. However, when $\alpha_1 \neq 0$, the classic homoclinic snaking type of bifurcation is broken, and a branch of one or more localized peaks forms an isolated stack. This means that the unstable branch associated with the dissipative soliton is not connected to the modulational instability threshold. This property is inherent to all irreversible systems in which the reflection symmetry is broken, i.e., ($\tau \not\to -\tau$). The summary of this analysis is shown in Fig. 9). The bifurcation diagram for moving periodic solutions and a dissipative soliton with a single peak is shown in Fig. 9a). The speed of a dissipative soliton is shown in Fig. 9b). Profiles corresponding to the points A-D along the isola branch shown in Fig. 9c) are indicated in the bottom left corner.

LLE Eq. (20) without the effect of spectral filtering is known to present a homoclinic snaking bifurcation diagram. However, taking spectral filtering into account, the first $i\alpha_1\partial_\tau E$ derivative term in Eq. (20) is unavoidable, leading the homoclinic snaking bifurcation to be broken and the dissipative solitons to become asymmetric and exhibit motion. According to dynamical systems theory, this behavior is similar to the situation where considering the odd order of dispersion of Raman scattering leads to isolas [45], [46].

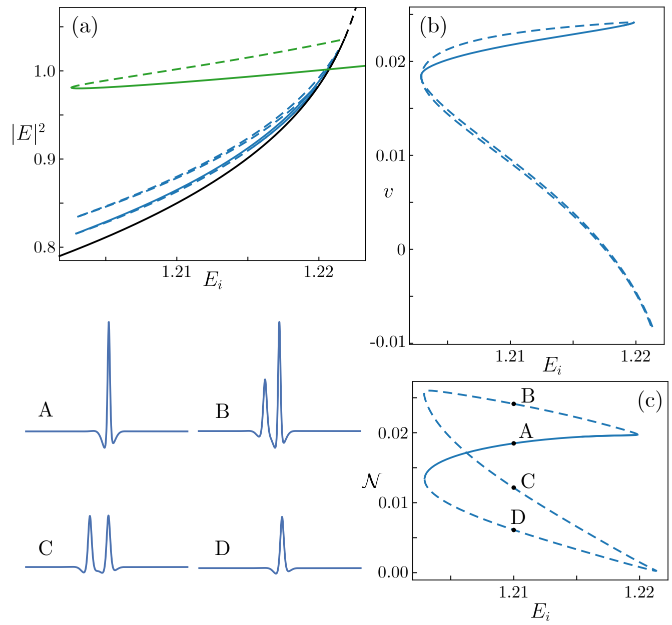

Fig. 9. Dissipative solitons isolas. (a) Bifurcation diagram showing the intensity of the intracavity field as a function of the injected field amplitude E_i. Black lines indicate the homogeneous steady state, green lines indicate the intensity of moving periodic solutions, and blue lines indicate the one-peak dissipative soliton. (b) Velocity of moving dissipative solitons isolas as a function of the injected field amplitude E_i. Full (dashed) lines correspond to stable (unstable) states, respectively. (c) L2-norm of the dissipative soliton branch as a function of the injected field amplitude. Insets A-D on the left show the profiles along the soliton branch. Parameters are $\delta = 1.7$, $\beta = 1$, and $\alpha_1 = \alpha_2 = \alpha = 0.1$.

V. Conclusions

We have studied the temporal formation of dissipative solitons and the corresponding combs generation in driven resonators under the combined influence of the Kerr effect, dispersion, dissipation, and spectral filtering. We have generalized the well-known mean-field Lugiato–Lefever model. The equation was derived from the infinite-dimensional Ikeda map with a general filter transfer function. It has been shown that in addition to the second-order derivative with a fast response time associated with the gain dispersion, an additional first-order derivative with a purely imaginary coefficient is necessary for the modeling. This term has a significant impact on the dynamics and results in the following consequences.

- The CW solutions stabilize the modulational instability by shifting it to higher intensity. Numerical simulations generate moving and breathing patterns. A branch of moving solutions connecting these periodic solutions to the modulational instability has been constructed using a continuation algorithm.
- It has been shown that the simple first derivative term not only breaks the reflection symmetry that causes dissipative solitons to move but also stabilizes the formation of moving dissipative solitons. In the monostable regime, where the CW solutions are single-valued functions of the injection field, we have shown that the stability domain of moving dissipative solitons is reduced by the spectral filtering.
- In the bistable regime, it has been demonstrated that spectral filtering increases the stability domain of regular moving dissipative solitons and moves the transition to breathing dissipative solitons to higher injected field amplitude. Numerical simulations have revealed the existence of moving-bounded dissipative solitons, including moving-breathing bounded dissipative solitons.
- The system's reflection symmetry is broken, which permits the formation of isolas dissipative solitons. In the absence of the first derivative, the system possesses reflection symmetry, and the bifurcation diagram comprises two snaking curves that are intertwined. These curves correspond to different numbers of peaks that are bound together.

Acknowledgments

M.B.G and M.G.C. acknowledge the financial support of ANID-Millennium Science Initiative Program-ICN17_012 (MIRO) and FONDECYT project 1210353. M.T. is a Research Director at Fonds de la Recherche Scientifique FNRS.

VI. References Section

References

[1] A. Pasquazi et al., Micro-combs: A novel generation of optical sources, Physics Reports, 729, 1, (2018).
[2] T. Fortier, E. Baumann, 20 years of developments in optical frequency comb technology and applications. Commun. Phys. 2019, 2, 153 (2019).
[3] N. Picqué, T.H. Hänsch. Frequency comb spectroscopy, *Nat. Photon.*, **13**, 146 (2019).
[4] T.H. Hänsch, Nobel lecture: passion for precision, Reviews of Modern Physics, 78, 1297 (2006).
[5] Herr, T., Brasch, V., Jost, J. D., Wang, C. Y., Kondratiev, N. M., Gorodetsky, M. L., Kippenberg, T. J. Temporal solitons in optical microresonators. *Nat. Photon.* **8**, 145 (2014).
[6] Kippenberg, T. J., Gaeta, A. L., Lipson, M. Gorodetsky, M. L. Dissipative Kerr solitons in optical microresonators. *Science* **361**, 6402 (2018).
[7] P. Del'Haye, A. Schliesser, O. Arcizet, T. Wilken, R. Holzwarth, T.G. Kippenberg. Optical frequency comb generation from a monolithic microresonator. Nature, 450(7173), 1214 (2007).
[8] S.B. Papp, K. Beha, P. Del'Haye, F. Quinlan, H. Lee, K.J. Vahala, S. A. Diddams. Microresonator frequency comb optical clock. Optica, 1(1), 10(2014).
[9] M.G. Suh, K.J. Vahala. Soliton microcomb range measurement. Science, 359(6378), 884 (2018).
[10] Spencer et al. An optical-frequency synthesizer using integrated photonics. Nature, 557(7703), 81 (2018).
[11] B. Min L. Yang, K. Vahala. Controlled transition between parametric and Raman oscillations in ultrahigh-Q silica toroidal microcavities. *Appl. Phys. Lett.* **87**, 181109 (2005).
[12] W. Liang, V. Ilchenko, A. Savchenkov, A. Matsko, D. Seidel, L. Maleki. Passively Mode-Locked Raman Laser. *Phys. Rev. Lett.* **105**, 143903 (2010).
[13] M. Karpov, H. Guo, A. Kordts, V. Brasch, M.H.P. Pfeiffer, M. Zervas, M. Geiselmann, T.J. Kippenberg. Raman self-frequency shift of dissipative Kerr solitons in an optical microresonator. *Phys. Rev. Lett.* **116**, 103902 (2016).
[14] X. Liu, C. Sun, B. Xiong, L. Wang, J. Wang, Y. Han, Z. Hao, H. Li, Y. Luo, J. Yan, H.X. Tang. Integrated High-Q Crystalline AlN Microresonators for Broadband Kerr and Raman Frequency Combs. *ACS Photonics* **5**, 1943 (2018).
[15] A. Chen-Jinnai, T. Kato, S. Fujii, T. Nagano, T. Kobatake, T. Tanabe. Broad bandwidth third-harmonic generation via four-wave mixing and stimulated Raman scattering in a microcavity. *Opt. Express* **24**, 26322 (2016).
[16] S. Zhu, L. Shi, L. Ren, Y. Zhao, B. Jiang, B. Xiao, X. Zhang. Controllable Kerr and Raman-Kerr frequency combs in functionalized microsphere resonators. *Nanophotonics*, **8**, 2321 (2019).
[17] L. A. Lugiato and R. Lefever, Phys. Rev. Lett. 58, 2209 (1987).
[18] Y. K. Chembo, D. Gomila, M. Tlidi, and C. R. Menyuk, The European Physical Journal D 71, 198 (2017).
[19] Scroggie, A. J., Firth, W. J., McDonald, G. S., Tlidi, M., Lefever, R., Lugiato, L. A. Pattern formation in a passive Kerr cavity. *Chaos, Solitons & Fractals* **4**, 1323 (1994).
[20] Tlidi, M., Mandel P. & Lefever, R. Localized structures and localized patterns in optical bistability. *Phys. Rev. Lett.* **73**, 640 (1994).
[21] A.B. Matsko, A. A. Savchenkov, W., Liang, V. Ilchenko, D. Seidel, L. Maleki, Mode-locked Kerr frequency combs. Opt. Lett. 36, 2845 (2011).
[22] S. Coen, H.G. Randle, T. Sylvestre, M. Erkintalo. Modeling of octave-spanning kerr frequency combs using a generalized mean-field Lugiato–Lefever model. Opt. Lett. 38, 37 (2013).
[23] L.A. Lugiato, F. Prati, M. Gorodetsky, T.J. Kippenberg. From the Lugiato–Lefever equation to microresonator-based soliton Kerr frequency combs. Phil. Trans. R. Soc. A 376, 20180113 (2018).
[24] M. Tlidi, M. Clerc, and K. Panajotov, Dissipative structures in matter out of equilibrium: from chemistry, photonics and biology, the legacy of ilya prigogine (part 1), Philos. Trans. R. Soc., A 376, 20180114 (2018).
[25] M.G. Clerc, S. Coulibaly, M. Tlidi. Time-delayed nonlocal response inducing traveling temporal localized structures. *Phys. Rev. Research* **2**, 013024 (2020).
[26] M.G. Clerc, S. Coulibaly, P. Parra-Rivas, M. Tlidi. Non-local Raman response in Kerr resonators: Moving temporal localized structures and bifurcation structure, *Chaos* **30**, 083111 (2020).
[27] P. Parra-Rivas, S. Coulibaly, M.G. Clerc, M. Tlidi. Influence of stimulated Raman scattering on Kerr domain walls and localized structures. *Phys. Rev. A* **103**, 013507 (2021).
[28] M. Tlidi, L. Bahloul, L. Cherbi, A. Hariz, and S. Coulibaly, Drift of dark cavity solitons in a photonic-crystal fiber resonator, Phys. Rev. A 88, 035802 (2013).
[29] M. Tlidi, A.G. Vladimirov, P. Pieroux, D. Turaev. Spontaneous motion of cavity solitons induced by a delayed feedback, Phys. Rev. lett. 103, 103904 (2009).
[30] F. Bessin, A.M. Perego, K. Staliunas, S.K. Turitsyn, A. Kudlinski, M. Conforti, A. Mussot, Gain-through-filtering enables tuneable frequency comb generation in passive optical resonators. Nature communications, 10, 4489 (2019).
[31] A.M. Perego, A. Mussot, M. Conforti, Phys. Rev. A 58, 2209 (2021).
[32] X. Dong , S. Christopher, V.G. Bucklew, H.W. Renninger, Chirped-pulsed Kerr solitons in the Lugiato-Lefever equation with spectral filtering Phys. Rev. Research 3, 033252 (2021).
[33] A. Pimenov, A.G. Vladimirov, Temporal solitons in an optically injected Kerr cavity with two spectral filters, Optics 3.4, 364 (2022).
[34] A. G. Vladimirov and D. A. Dolinina. Neutral delay differential equation model of an optically injected Kerr cavity, Phys. Rev. E 109, 024206 (2024).
[35] D. Turaev, A. G. Vladimirov, and S. Zelik. Long Range Interaction and Synchronization of Oscillating Dissipative Solitons, Phys. Rev. Lett. 108, 263906 (2012).
[36] U. Bortolozzo, M. G. Clerc, and S Residori. Solitary localized structures in a liquid crystal light-valve experiment, New J. Phys. 11, 093037 (2009).
[37] J. M. Soto-Crespo, N. N. Akhmediev, P. Grelu, and F. Belhache. Quantized separations of phase-locked soliton pairs in fiber lasers. Opt. Lett. 28, 1757 (2003).
[38] M. Olivier, V. Roy, and M. Piché, Opt. Lett. 31, 580 (2006).
[39] A. G. Vladimirov, M. Tlidi, and M. Taki, Dissipative soliton interaction in Kerr resonators with high-order dispersion Phys. Rev. A 103, 063505 (2021)
[40] N. N. Akhmediev and M. Karlsson, Cherenkov radiation emitted by solitons in optical fibers. Phys. Rev. A 51, 2602 (1995).
[41] A. G. Vladimirov, S. V. Gurevich, and M. Tlidi, Effect of Cherenkov radiation on localized-state interaction, Phys. Rev. A 97, 013816 (2018).
[42] Y. Pomeau, Physica D 23, 3 (1986).
[43] M. Tlidi, L. Gelens, High-order dispersion stabilizes dark dissipative solitons in all-fiber cavities, Opt. Lett., 35, 306 (2010).
[44] P. Parra-Rivas, D. Gomila, M.A. Matias, S. Coen, L. Gelens. Dynamics of localized and patterned structures in the Lugiato-Lefever equation determine the stability and shape of optical frequency combs, Phys. Rev. A 89 (4), 043813 (2014).
[45] P. Parra-Rivas, D. Gomila, F. Leo, S. Coen, S., L. Gelens, L. Third-order chromatic dispersion stabilizes Kerr frequency combs. Opt. Lett. 39, 2971 (2014).
[46] M Tlidi, M Bataille-Gonzalez, MG Clerc, L Bahloul, S Coulibaly, B Kostet, C. Casillo-Pinto, K. Panajotov, Isolas of localized structures and Raman–Kerr frequency combs in micro-structured resonators. Chaos, Solitons & Fractals 174, 113808 (2023).

5.1 Perspectives

In this article, we showed that, under the addition of a spectral filter, a series of derivative terms must be incorporated into the LLE. Then, assuming a sufficiently localized filter, we justified a second-order truncation of the series and studied the effects of the additional terms with coefficients α_1, α_2 on the stability and dynamics of both localized and periodic structures. However, a more extensive exploration of the system's parameters remains to be performed. In this direction, a phase diagram showing the stability boundaries in terms of these two coefficients would provide a more complete description and be especially helpful for experimentalists. On this note, it would also be interesting to compute the coefficients corresponding to previous experimental studies [109] and test whether our approximation is still valid in a real experiment. If this is not the case, then a detailed numerical analysis via continuation of the integrodifferential equation deserves to be performed and compared with the results shown in this chapter.

Chapter 6

Moving spiral wave chimeras (Physical Review E, 104(2), L022203)

So far, this investigation has focused on drifting one-dimensional localized states in two non-local optical systems. In these two cases, the motion itself was expected since a reflection symmetry-breaking term was present. Nevertheless, such a term is not always necessary to set localized states in motion. Indeed, this chapter exposes that motion can arise spontaneously in an isotropic system of coupled phase oscillators.

In section 2.4.1, the importance and universality of phase oscillators have been emphasized, as they offer a comprehensive description of self-sustained oscillators at the cost of neglecting amplitude dynamics. Such oscillators are ubiquitous, appearing in flashing fireflies, lasers, neurons, and even pacemaker cells in the heart. The dynamics of an individual oscillator represent a profound research challenge, as exemplified by the seminal work of Hodgkin and Huxley, which earned them the Nobel Prize for their model of neuronal activity [110]. Extending this complexity, the dynamics of a population of coupled phase oscillators exhibit even greater richness. A fundamental question in such systems is whether the oscillators will synchronize and, if so, to what degree.

One of the most outstanding contributions to the field of synchronization was made by Kuramoto who provided a simple yet powerful model for describing coupled oscillators several decades ago [69]. Remarkably, when Kuramoto and Battogtokh extended the model considering non-local coupling instead of the original global coupling, they observed an incongruous state of partial synchrony where coherent (synchronized) and incoherent (desynchronized) domains coexisted [75]. It could be expected that coupling identical oscillators would only yield a completely coherent state, yet they showed that the symmetry could be spontaneously broken and the system would self-organize into two different and coexisting domains, what we now call a chimera state [76].

Even more surprisingly, two-dimensional simulations of the Kuramoto-Battogtokh model revealed a planar chimera state in the form of a spiral wave [111, 112]. This spiral wave chimera, characterized by an incoherent core at the tip of the spiral where oscillators were desynchronized, stood in contrast to the synchronized oscillators forming the spiral arms. Unlike previously observed spiral patterns in reaction-diffusion systems [113], these chimeras exhibited a unique feature: the phase singularity at the tip was replaced by an incoherent core. Since their discovery, spiral chimeras have been extensively studied in various systems, and their existence has been experimentally confirmed, particularly in chemical systems [84, 85].

In this chapter, we investigate the dynamics of a bound state of two counter-rotating spiral wave chimeras in a two-dimensional array of coupled non-identical phase oscillators. To eliminate the finite-size noise, the continuum limit of infinitely many oscillators is studied in detail by numerically simulating the associated Ott-Antonsen equation. Although a symmetric and isotropic coupling function is considered, the top-hat function, a spontaneous symmetry breaking arises which causes the two-core spiral chimeras to develop a permanent motion. Consequently, the formation of a crescent-shaped filamentary pattern is observed in the incoherent core of the spirals, and is oriented towards the direction of motion. Moreover, 3 different two-core spiral chimeras are identified according to their motion, namely symmetric, asymmetric and meandering spirals, and their corresponding stability region is determined.

Letter

Moving spiral wave chimeras

Martin Bataille-Gonzalez,[1] Marcel G. Clerc,[1] and Oleh E. Omel'chenko[2,*]

[1]*Departamento de Física and Millenium Institute for Research in Optics, Facultad de Ciencias Físicas y Matemáticas, Universidad de Chile, Casilla 487-3, Santiago, Chile*

[2]*Institute of Physics and Astronomy, University of Potsdam, Karl-Liebknecht-Straße 24/25, 14476 Potsdam, Germany*

(Received 29 March 2021; accepted 4 August 2021; published 20 August 2021)

We consider a two-dimensional array of heterogeneous nonlocally coupled phase oscillators on a flat torus and study the bound states of two counter-rotating spiral chimeras, shortly two-core spiral chimeras, observed in this system. In contrast to other known spiral chimeras with motionless incoherent cores, the two-core spiral chimeras typically show a drift motion. Due to this drift, their incoherent cores become spatially modulated and develop specific fingerprint patterns of varying synchrony levels. In the continuum limit of infinitely many oscillators, the two-core spiral chimeras can be studied using the Ott-Antonsen equation. Numerical analysis of this equation allows us to reveal the stability region of different spiral chimeras, which we group into three main classes—symmetric, asymmetric, and meandering spiral chimeras.

DOI: 10.1103/PhysRevE.104.L022203

Spiral waves are ubiquitous in nature [1]. They can be found in various biological and chemical systems, including cardiac [2] and epithelial [3] tissues, mammalian neocortex [4,5], spatially distributed cell populations [6,7], and oscillatory chemical reactions [8–12]. From a functional point of view, rotating spiral waves are often associated with cardiac arrhythmia and fibrillation [13]. Moreover, such waves have also been observed in two-dimensional cilia arrays [14,15], where they may be related to the transport function of the corresponding tissue or cell colony [16].

Until recently, the mathematical description of spiral waves was mainly based on multicomponent reaction-diffusion systems [17,18] with excitable or oscillatory local dynamics. The effect of diffusion, in this case, guarantees that the spiral wave profile is smooth everywhere, except the phase defect at the tip of the spiral arms. However, is this a correct assumption for biological systems that consist of individual cells and are therefore inherently discrete? In general, these systems can show more complicated dynamical patterns that differ qualitatively from those in continuous media. A wide variety of such unusual patterns has been recently discovered in systems with nonlocal coupling [19–22]. For example, in 2003, Kuramoto and Shima reported the existence of strange spiral waves in two-dimensional arrays of nonlocally coupled limit-cycle oscillators [23,24]. The spiral arms of these waves consist of synchronized/coherent oscillators and resemble the spiral arms of usual spiral waves in continuous media. But the dynamics of the oscillators close to the spiral defect (in the so called spiral core) turns out to be spatially randomized and incoherent such that it masks the position of the phase defect. Similar coexistence of coherent and incoherent dynamics in a homogeneous oscillatory medium is currently known as the *chimera state* (see Refs. [19–22] and references therein), therefore spiral waves with coherent spiral arms and incoherent cores were called *spiral wave chimeras* [25] or simply *spiral chimeras*.

So far, spiral chimeras have been observed as motionless patterns with fixed positions of their incoherent cores and uniformly rotating coherent spiral arms. In particular, one-core and multicore spiral chimeras were reported in two-dimensional arrays with open boundary conditions [23–25] and periodic boundary conditions representing a flat torus [26–31] or a sphere [32,33]. Beyond phase oscillator models, the existence of spiral chimeras was also confirmed for many realistic systems consisting of limit-cycle oscillators [23,24,34–38], integrate-and-fire neurons [39,40], or even locally chaotic dynamical units [41]. Moreover, recently spiral chimeras were observed in laboratory experiments with the discrete Belousov-Zhabotinsky (BZ) chemical oscillators [42–44].

In this Letter, we show that spiral wave chimeras, in general, do not need to be motionless. Even in translationally invariant systems with isotropic nonlocal coupling, they can move along straight lines or more complicated twisted trajectories. Similarly to moving spiral pairs in oscillatory continuous media [45], the simplest moving spiral chimera looks like a bound state of two reflection-symmetric counter-rotating spirals that move perpendicular to the line connecting their cores. However, due to nonlocal coupling, these chimera states acquire several remarkable properties. First, their core regions are typically spatially modulated. Second, the symmetry breaking in spiral chimeras occurs quite differently than in continuous media [46,47]: Even if the two spiral cores are nonidentical, they continue to drift together. Moreover, in some cases, the direction of the chimera's movement turns out to depend smoothly on system parameters. As a result, asymmetric spiral chimeras can move in arbitrary direction, even along the line connecting their cores.

*Corresponding author: omelchenko@uni-potsdam.de

Model. We consider a two-dimensional array of phase oscillators $\{\theta_{jk}(t)\}_{j,k=1}^{N}$ evolving according to

$$\frac{d\theta_{jk}}{dt} = \omega_{jk} - \frac{1}{|B_\sigma(j,k)|} \sum_{(m,n)\in B_\sigma(j,k)} \sin(\theta_{jk} - \theta_{mn} + \alpha). \tag{1}$$

Here ω_{jk} are natural frequencies of the oscillators drawn randomly and independently from a Lorentzian distribution $g(\omega) = \gamma/[\pi(\omega^2 + \gamma^2)]$, with width $\gamma > 0$, $\alpha \in (0, \pi/2)$ is the phase lag parameter, $\sigma \in (0, 1/2)$ is the relative coupling radius, and

$$B_\sigma(j,k) = \{(m,n) : (m-j)^2 + (n-k)^2 \leqslant \sigma^2 N^2\}$$

denotes the circular neighborhood of the point (j,k) where the distances $m-j$ and $n-k$ are considered $\bmod N$. The interaction term in Eq. (1) is referred to as nonlocal coupling and is normalized by the number of points $|B_\sigma(j,k)|$ in the neighborhood $B_\sigma(j,k)$.

It is well known [30] that Eq. (1) supports different motionless chimera patterns, including stripe and spot chimera states as well as four-core spiral chimeras. This Letter demonstrates that the same equation also supports a qualitatively different type of chimera states, called *moving spiral chimeras*. Figure 1 provides several examples of such states in the array of 1024×1024 oscillators (see also Ref. [48] for their movies). The left column shows the phase snapshots, while the right column shows the corresponding local order parameters calculated by

$$z_{jk}(t) = \frac{1}{|B_\delta(j,k)|} \sum_{(m,n)\in B_\delta(j,k)} e^{i\theta_{mn}(t)}, \tag{2}$$

with $\delta = 1/(2\sqrt{N})$. By definition, the absolute value $|z_{jk}(t)|$ measures the degree of synchronization between the neighbors of the oscillator $\theta_{jk}(t)$. In particular, $|z_{jk}(t)| = 1$ corresponds to perfect synchrony of the phases, whereas $|z_{jk}(t)| \approx 0$ stands for their complete disorder. Thus a chimera state is characterized by the coexistence of nearly unit values $|z_{jk}(t)|$ in the coherent region with relatively small values of $|z_{jk}(t)|$ in the incoherent region. Notice that to find the positions of incoherent cores it is convenient to use not the local order parameter $z_{jk}(t)$, but a mean field $w_{jk}(t)$ computed by the formula (2) with $\delta = \sigma$. The modulus $|w_{jk}(t)|$ has pronounced minima at the sites, which can be identified with the phase defects of the corresponding spirals.

In our numerical simulations performed with a fixed-step fourth order Runge-Kutta integrator, we have observed three main types of moving two-core spiral chimeras:

(a) Symmetric spiral chimeras. These chimeras have incoherent cores of nearly the same shape and size. In the graph of the local order parameter $z_{jk}(t)$ each incoherent core looks either as a circle with a phase defect in the middle, or as a specific fingerprint pattern composed of curved stripes corresponding to higher and lower local synchrony of the oscillators. Symmetric spiral chimeras move strictly vertically or horizontally.

(b) Asymmetric spiral chimeras. These chimeras have incoherent cores of different shapes and sizes. The cores move along straight lines in a direction, which in general is neither vertical nor horizontal.

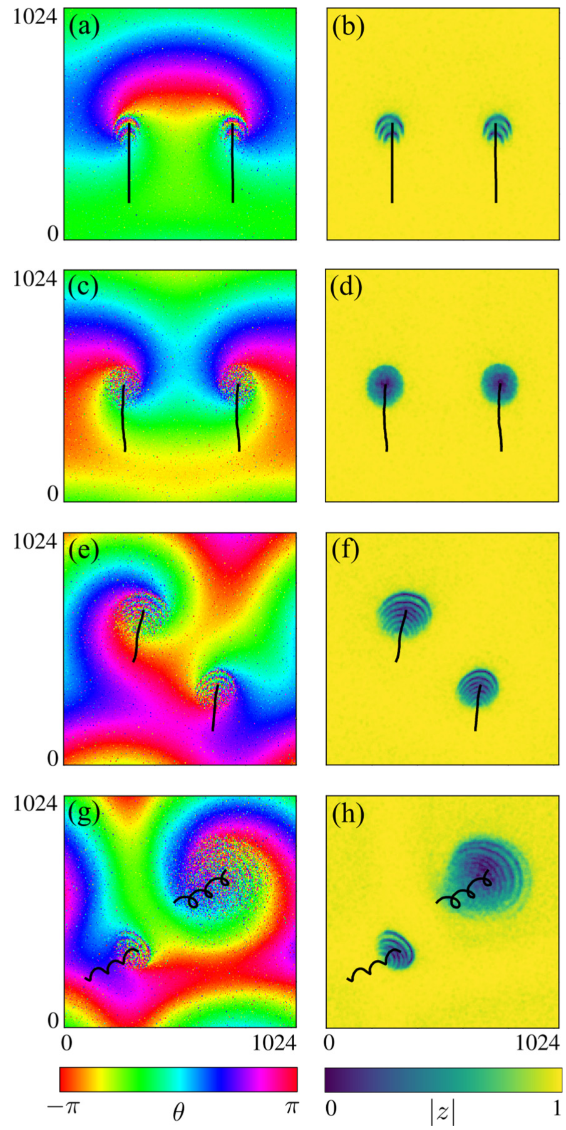

FIG. 1. Moving spiral chimeras in Eq. (1) with $\alpha = 0.6$ [(a) and (b)], $\alpha = 0.7$ [(c) and (d)], $\alpha = 0.8$ [(e) and (f)], and $\alpha = 1.01$ [(g) and (h)]. Other parameters: $N = 1024$, $\sigma = 0.25$, and $\gamma = 0.01$. The left and right columns show snapshots $\theta_{jk}(t)$ and the local order parameters $|z_{jk}(t)|$ computed by (2). The black curves show movement trajectories of the incoherent cores.

(c) Meandering spiral chimeras. These are nonstationary versions of asymmetric spiral chimeras. They move not as a rigid body but rather as a periodically breathing pattern. Their movement trajectories are not straight lines, but twisted curves which can be thought of as a superposition of a uniform drift and oscillatory motion.

In the following, we outline the stability regions in the parameter plane (α, σ) for each of the above moving spiral chimeras.

Methods. For every trajectory of Eq. (1), we can define a piecewise-linear function $Z_N(x, y, t)$ on the flat torus $(x, y) \in$

$[-\pi, \pi]^2$ such that

$$Z_N(-\pi + 2\pi j/N, -\pi + 2\pi k/N, t) = z_{jk}(t).$$

It is well known that in the continuum limit case, i.e., when $N \to \infty$, the long-term dynamics of $Z_N(x, y, t)$ is asymptotically close to a solution $z(x, y, t)$ of the Ott-Antonsen equation

$$\frac{dz}{dt} = -\gamma z + \frac{1}{2}e^{-i\alpha}\mathcal{G}z - \frac{1}{2}e^{i\alpha}z^2\mathcal{G}\bar{z}, \tag{3}$$

where $\bar{z}$ denotes the complex conjugate of z, and $\mathcal{G}z$ is a convolution term of the form

$$(\mathcal{G}z)(x, y, t) = \frac{1}{\pi^3\sigma^2} \iint_{|x-x'|^2+|y-y'|^2\leqslant\pi^2\sigma^2} z(x', y', t)dx'dy'.$$

Note that the distance $|x - x'|^2 + |y - y'|^2$ in the above integral has to be computed accounting for periodic boundary conditions in the x and y directions. The derivation of Eq. (3) is based on the invariant manifold reduction technique suggested in Ref. [49] and its details can be found in Refs. [21,50]. Thus, the existence and stability of moving spiral chimeras in Eq. (1) can be studied using Eq. (3).

We discretize Eq. (3) on a uniform grid with 256×256 nodes, replace all integrals by trapezoid rule and carry out direct numerical simulations of the resulting ordinary differential equations using the Python *RK45* solver from the SciPy package with adaptive or fixed ($dt = 0.1$) time step. We keep $\gamma = 0.01$ fixed and change parameters σ and α. For every chosen pair (α, σ) we integrate the discretized version of Eq. (3) over 2×10^4 time units. The initial part of the trajectory of the length 10^4 is discarded as a transient and the remaining part of the length 10^4 is analyzed in the following way.

We compute a mean field $w(x, y, t) = (\mathcal{G}z)(x, y, t)$. In the case of a two-core spiral chimera, this complex function has exactly two phase defects where $|w(x, y, t)| = 0$. This allows us to trace the trajectory of each defect and compute its instantaneous velocity $\mathbf{v}(t) = (v_x(t), v_y(t))$. Though the trajectories of two phase defects can be different, the long-time averages $\langle v_x\rangle$ and $\langle v_y\rangle$ calculated along one of the trajectories are the same as those calculated along the other trajectory, therefore we can define two scalars characterizing the spiral chimera motion:

(i) the mean drift velocity $s = |\langle v_x\rangle + i\langle v_y\rangle|$, and

(ii) the direction of drift motion

$$\psi = \arg(\langle v_x\rangle + i\langle v_y\rangle).$$

Obviously, for a symmetric spiral chimera, we must obtain $\psi = 0, \pm\pi/2, \pi$, whereas all other values ψ are indications of asymmetric spiral chimeras.

It turns out that all solutions of Eq. (3) corresponding to two-core spiral chimeras assume one of the following two forms. Symmetric and asymmetric spiral chimeras are described by an ansatz

$$z(x, y, t) = a(x - s_x t, y - s_y t)e^{i\Omega t}, \tag{4}$$

where $a(x, y)$ is a complex amplitude and s_x, s_y, and Ω are real constants. A symmetric spiral chimera is obtained if $s_x = 0$ and $a(-x, y) = a(x, y)$ or if $s_y = 0$ and $a(x, -y) = a(x, y)$. Otherwise the spiral chimera is asymmetric. The second ansatz representing meandering spiral chimeras reads

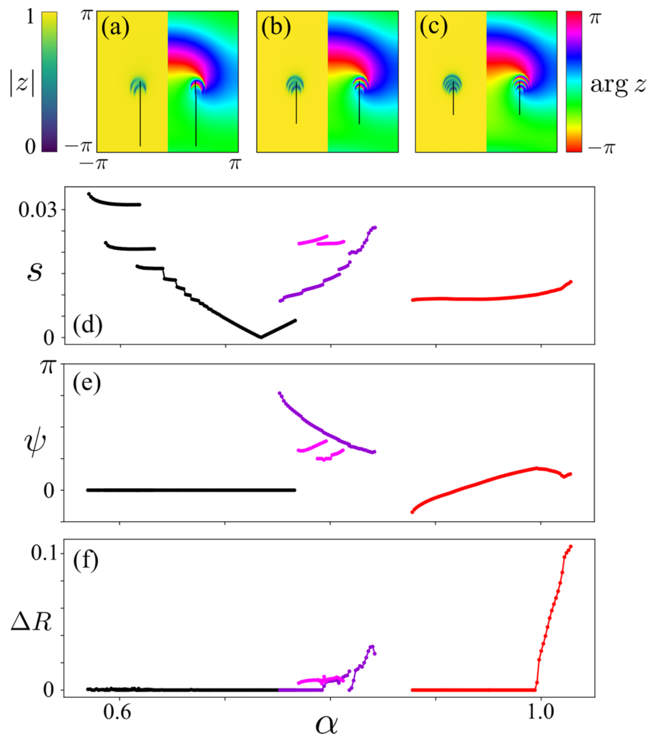

FIG. 2. Mean drift velocity s (d), direction of drift motion ψ (e) and variance of the global order parameter ΔR (f) for two-core spiral chimeras in Eq. (3) with $\sigma = 0.25$ and $\gamma = 0.01$. The black and color dots in (d)–(f) correspond to symmetric and asymmetric spiral chimeras, respectively. Three top panels exemplify solutions $z(x, y, t)$ for $\alpha = 0.58$ (a), $\alpha = 0.60$ (b), and $\alpha = 0.63$ (c). The black curves in these panels show the trajectories of incoherent cores.

$$z(x, y, t) = a(x - s_x t, y - s_y t, t)e^{i\Omega t}, \tag{5}$$

where the amplitude $a(x, y, t)$ depends explicitly on time. (Typically this dependence is periodic.) In order to distinguish between cases (4) and (5) numerically one can compute the difference $\Delta R = \max_t R(t) - \min_t R(t)$, where

$$R(t) = \left| \frac{1}{4\pi^2} \int_{-\pi}^{\pi} \int_{-\pi}^{\pi} z(x, y, t)dxdy \right|$$

is the global order parameter. Then in the former case, one obtains $\Delta R = 0$, while in the latter case one gets $\Delta R > 0$. Therefore spiral chimeras described by formulas (4) and (5) can be called stationary and nonstationary spiral chimeras, respectively.

Results. Using the local order parameters from Fig. 1 as initial conditions and performing forward and backward α-sweeps with the step $d\alpha = 0.002$ for fixed coupling radius $\sigma = 0.25$, we obtained a diagram shown in Fig. 2. Note that two adjacent points were connected by a line only in the case if the right point was obtained in the forward sweep starting from the left point and vice versa. Moreover, each sweep was stopped at the value α for which stable two-core spiral chimeras ceased to exist. Figure 2 reveals that stable symmetric spiral chimeras can be found for $\alpha \in$

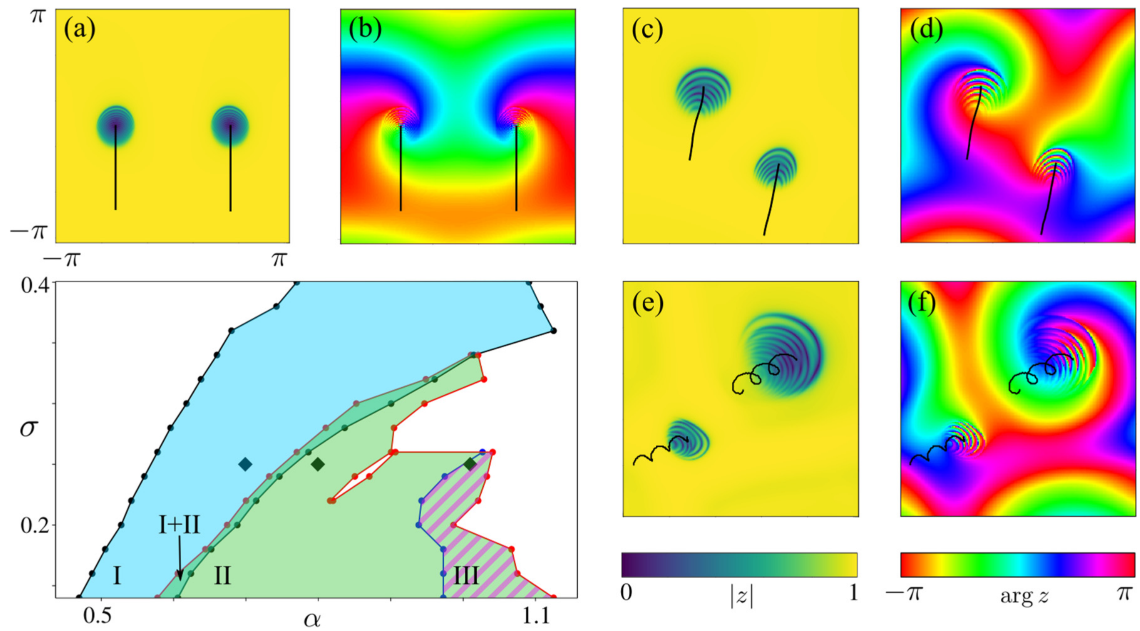

FIG. 3. The main panel (bottom left) shows the stability regions of the symmetric (I), stationary asymmetric (II), and meandering (III) two-core spiral chimeras in the Eq. (3) with $\gamma = 0.01$. The boundaries of these regions consist of the dots, for which α sweeps were carried out, and the interpolating lines. Additional panels exemplify solutions $z(x, y, t)$ for $(\alpha, \sigma) = (0.7, 0.25)$ [(a) and (b)], (0.8,0.25) [(c) and (d)], and (1.01,0.25) [(e) and (f)]. These parameters are indicated by diamonds in the stability diagram. The black curves in the panels (a)–(f) show movement trajectories of the incoherent cores.

[0.57, 0.766], whereas stable asymmetric spiral chimeras can be found in two disjoint intervals $\alpha \in [0.752, 0.852]$ and $\alpha \in [0.878, 1.028]$. Note that the ranges of symmetric and asymmetric chimeras have a small overlap where both of them coexist stably. Moreover, several other bi- and tristability ranges can be found in the left and middle parts of the diagram.

The branch of symmetric spiral chimeras consists of several disconnected curves. The chimeras on the leftmost curve are the fastest. Their core regions are simple patterns consisting of two curved stripes corresponding to small values of $|z(x, y, t)|$. On the second and third curves from above we find spiral chimeras with core regions composed of three and four stripes, respectively. The general rule is that for α increasing from 0.57 to 0.734 the motion of spiral chimeras slows down, while the number of stripes in their core regions grows. As a result, these regions begin to look as intricate fingerprint patterns. However, for $\alpha \approx 0.734$ the incoherent stripes merge together and the core regions become circular-shaped, which is typical for motionless spiral chimeras [27].

The branch of asymmetric spiral chimeras also consists of several disconnected curves. All these spiral chimeras have nonvanishing mean velocities $s > 0.008$ and their core regions typically look as fingerprint patterns composed of many incoherent stripes. The most prominent feature of asymmetric spiral chimeras is that for sufficiently large values α they become nonstationary and transform into meandering spiral chimeras. For example, Fig. 2 indicates that asymmetric spiral chimeras are stationary ($\Delta R = 0$) for $\alpha \in [0.752, 0.792]$ (on the slowest part of the branch only) and for $\alpha \in [0.996, 1.028]$. For all other phase lags these chimeras do not behave as rigidly moving patterns, but breathe periodically on top of the uniform drift motion.

Parameter sweeps similar to Fig. 2 were also performed for other coupling radii σ varying from 0.14 to 0.4 with the step $d\sigma = 0.02$. Thus we obtained a stability diagram shown in Fig. 3. Our general observations can be summarized as follows. The branch of symmetric spiral chimeras has a similar shape for all values σ, though it shifts to larger values α for increasing coupling radius. Regarding the asymmetric spiral chimeras, we found that their stability range has the maximal size for small values σ and shrinks gradually for increasing coupling radius until it eventually vanishes for $\sigma > 0.34$. We also found that the size of the core region of a spiral chimera typically increases with increasing parameters α and σ. However, the mean drift velocity s turns out to be more sensitive to the changes of the coupling radius σ than to the changes of the phase lag α. Notice that two-core spiral chimeras can also be found for coupling radii smaller than 0.14, but in this case their drift velocity decreases significantly and almost vanishes for $\sigma \leqslant 0.1$ such that they appear as pinned spiral waves or spiral waves moving along closed circular orbits.

Conclusions. Discrete two-dimensional media made up of oscillatory or excitable active units are found in many biological systems. Above, we have shown that under the influence of nonlocal coupling, these media can support moving spiral wave chimeras with a complex distribution of synchronous and asynchronous regions. Using the Ott-Antonsen equation (3), we computed stability diagrams for these chimera states and found how the speed and the direction of their drift depend on system parameters. This information can be used to search for moving spiral chimeras in experiments similar to Refs. [42–44] or in the cilia carpet system studied theoretically in Ref. [14].

Several interesting questions about the nature of moving spiral chimeras still remain open. First, it seems likely that the distinct solution curves in Fig. 2 are connected by unstable solution branches. Moreover, it is unclear whether there is a branch that connects the moving spiral chimeras with their motionless counterparts. To answer these questions, one needs to perform a more detailed analysis of traveling wave solutions (4) in Eq. (3) by analogy with Refs. [51,52]. The same approach can also be used to study the behavior of moving spiral chimeras for small values of the coupling radius σ, which we have not addressed in this Letter. Another challenging problem is the rigorous mathematical description of moving spiral chimeras in Eq. (1) with identical oscillators. It is known [53,54] that in this case, Eq. (3) becomes singular and can no longer be used. Finally, we emphasize that Eq. (1) can show more complex moving spiral chimeras, see Fig. 4, which also deserve consideration. We hope that further research in the field will answer the above questions and, therefore, improve our understanding of pattern formation in discrete active media with nonlocal coupling.

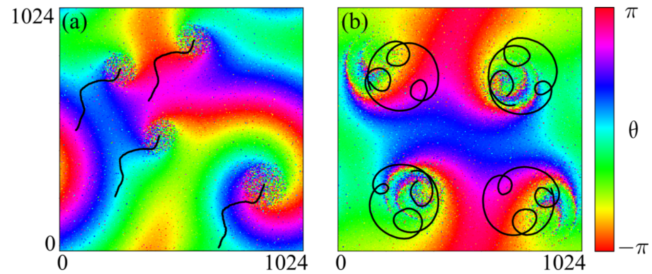

FIG. 4. Four-core moving spiral chimeras in Eq. (1) with $\alpha = 0.8$, $\sigma = 0.2$ (a) and $\alpha = 0.9$, $\sigma = 0.25$ (b). For other parameters and notations see Fig. 1.

Acknowledgment. The work of O.E.O. was supported by the Deutsche Forschungsgemeinschaft under Grant No. OM 99/2-1. M.B.G. acknowledges the hospitality of the University of Potsdam during his research internship. M.G.C. thanks for the financial support ANID-Millenium Science Initiative Program–ICN17_012.

[1] K. Tsuji and S. C. Müller (eds.), *Spirals and Vortices* (Springer, Cham, 2019).
[2] J. M. Davidenko, A. M. Pertsov, R. Salomonsz, W. Baxter, and J. Jalife, Nature (London) **355**, 349 (1992).
[3] G. Seiden and S. Curland, New J. Phys. **17**, 033049 (2015).
[4] X. Huang, W. C. Troy, Q. Yang, H. Ma, C. R. Laing, S. J. Schiff, and J.-Y. Wu, J. Neurosci. **24**, 9897 (2004).
[5] X. Huang, W. Xu, J. Liang, K. Takagaki, X. Gao, and J.-Y. Wu, Neuron **68**, 978 (2010).
[6] J. Lechleiter, S. Girard, E. Peralta, and D. Clapham, Science **252**, 123 (1997).
[7] J. Lauzeral, J. Halloy, and A. Goldbeter, Proc. Natl. Acad. Sci. USA **94**, 9153 (1997).
[8] A. M. Zhabotinsky and A. N. Zaikin, J. Theor. Biol. **40**, 45 (1973).
[9] A. T. Winfree, Science **175**, 634 (1972).
[10] A. S. Mikhailov and K. Showalter, Phys. Rep. **425**, 79 (2006).
[11] V. K. Vanag and I. R. Epstein, in *Self-Organized Morphology in Nanostructured Materials*, edited by K. Al-Shamery and J. Parisi (Springer, Berlin, 2008), pp. 89–113.
[12] G. Ertl, Science **254**, 1750 (1991).
[13] R. A. Gray, A. M. Pertsov, and J. Jalife, Nature (London) **392**, 75 (1998).
[14] N. Uchida and R. Golestanian, Phys. Rev. Lett. **104**, 178103 (2010).
[15] R. Golestanian, J. M. Yeomans, and N. Uchida, Soft Matter **7**, 3074 (2011).
[16] W. Gilpin, M. S. Bull, and M. Prakash, Nat. Rev. Phys. **2**, 74 (2020).
[17] A. T. Winfree, Chaos **1**, 303 (1991).
[18] D. Barkley, Phys. Rev. Lett. **72**, 164 (1994).
[19] M. J. Panaggio and D. M. Abrams, Nonlinearity **28**, R67 (2015).
[20] E. Schöll, Eur. Phys. J. Spec. Top. **225**, 891 (2016).
[21] O. E. Omel'chenko, Nonlinearity **31**, R121 (2018).
[22] S. Majhi, B. K. Bera, D. Ghosh, and M. Perc, Phys. Life Rev. **28**, 100 (2019).
[23] Y. Kuramoto and S. Shima, Prog. Theor. Phys. Suppl. **150**, 115 (2003).
[24] S. I. Shima and Y. Kuramoto, Phys. Rev. E **69**, 036213 (2004).
[25] E. A. Martens, C. R. Laing, and S. H. Strogatz, Phys. Rev. Lett. **104**, 044101 (2010).
[26] P.-J. Kim, T.-W. Ko, H. Jeong, and H.-T. Moon, Phys. Rev. E **70**, 065201(R) (2004).
[27] O. E. Omel'chenko, M. Wolfrum, S. Yanchuk, Y. L. Maistrenko, and O. Sudakov, Phys. Rev. E **85**, 036210 (2012).
[28] M. J. Panaggio and D. M. Abrams, Phys. Rev. Lett. **110**, 094102 (2013).
[29] J. Xie, E. Knobloch, and H.-C. Kao, Phys. Rev. E **92**, 042921 (2015).
[30] C. R. Laing, SIAM J. Appl. Dyn. Syst. **16**, 974 (2017).
[31] O. E. Omel'chenko, M. Wolfrum, and E. Knobloch, SIAM J. Appl. Dyn. Syst. **17**, 97 (2018).
[32] M. J. Panaggio and D. M. Abrams, Phys. Rev. E **91**, 022909 (2015).
[33] R.-S. Kim and C.-U. Choe, Phys. Rev. E **98**, 042207 (2018).
[34] X. Tang, T. Yang, I. R. Epstein, Y. Liu, Y. Zhao, and Q. Gao, J. Chem. Phys. **141**, 024110 (2014).
[35] B.-W. Li and H. Dierckx, Phys. Rev. E **93**, 020202(R) (2016).
[36] A. V. Bukh and V. S. Anishchenko, Chaos Solitons Fract. **131**, 109492 (2020).
[37] I. A. Shepelev, A. V. Bukh, S. S. Muni, and V. S. Anishchenko, Regul. Chaotic Dynam. **25**, 597 (2020).
[38] V. Maistrenko, O. Sudakov, and Y. Maistrenko, Eur. Phys. J. Spec. Top. **229**, 2327 (2020).
[39] A. Schmidt, T. Kasimatis, J. Hizanidis, A. Provata, and P. Hövel, Phys. Rev. E **95**, 032224 (2017).
[40] G. Argyropoulos and A. Provata, Front. Appl. Math. Stat. **5**, 35 (2019).

[41] C. Gu, G. St-Yves, and J. Davidsen, Phys. Rev. Lett. **111**, 134101 (2013).
[42] S. Nkomo, M. R. Tinsley, and K. Showalter, Phys. Rev. Lett. **110**, 244102 (2013).
[43] J. F. Totz, J. Rode, M. R. Tinsley, K. Showalter, and H. Engel, Nat. Phys. **14**, 282 (2017).
[44] J. F. Totz, M. R. Tinsley, H. Engel, and K. Showalter, Sci. Rep. **10**, 7821 (2020).
[45] I. S. Aranson, L. Kramer, and A. Weber, Phys. Rev. E **47**, 3231 (1993).
[46] I. S. Aranson, L. Kramer, and A. Weber, Phys. Rev. E **48**, R9(R) (1993).
[47] I. Schebesch and H. Engel, Phys. Rev. E **60**, 6429 (1999).
[48] See the Supplemental Material http://link.aps.org/supplemental/10.1103/PhysRevE.104.L022203 for movies showing the dynamics of spiral wave chimeras in Figs. 1(a), 1(e), and 1(g).
[49] E. Ott and T. M. Antonsen, Chaos **18**, 037113 (2008).
[50] C. R. Laing, Physica D **238**, 1569 (2009).
[51] O. E. Omel'chenko, Nonlinearity **33**, 611 (2020).
[52] C. R. Laing and O. E. Omel'chenko, Chaos **30**, 043117 (2020).
[53] O. E. Omel'chenko, J. Phys. A: Math. Theor. **52**, 104001 (2019).
[54] J. Xie, E. Knobloch, and H.-C. Kao, Phys. Rev. E **90**, 022919 (2014).

6.1 Perspectives

In this work, we have shown that even in a symmetric system, two-core spiral chimeras move in three different ways. Furthermore, the stability region of symmetric, asymmetric and meandering spirals has been identified and presented in a phase diagram. Nevertheless, a more in-depth numerical analysis is still needed to find not only stable but also unstable states. This information will be fundamental to indentify the various bifurcations that lead to the emergence of two-core spiral chimeras from a homogeneous state, as well as the transition between symmetric and asymmetric spirals. On the other hand, we have examined the effect of a top-hat coupling function which has numerical advantages but may not be experimentally relevant. Therefore, the extent to which these results apply to more realistic couplings remains to be determined.

Chapter 7

Traveling spiral wave chimeras in coupled oscillator systems: emergence, dynamics, and transitions (New Journal of Physics 25, 103023)

Previously, we demonstrated that even with a symmetric coupling kernel, two-core spiral chimeras develop different types of sustained motion. However, the fundamental question of their emergence remained unresolved due to two main challenges. Firstly, the analytical results for the model proved extremely difficult to obtain, necessitating the use of numerical methods, which leads to the second issue. The computational cost, in both time and memory, of performing numerical continuation in a two-dimensional non-local model is exceedingly high.

This chapter addresses the previously stated question regarding the emergence of two-core spirals by analyzing two distinct coupling kernels: a top-hat and a sinusoidal kernel. In the case of the top-hat coupling, a complete bifurcation diagram of symmetric two-core spirals is provided via numerical continuation. Conversely, the sinusoidal kernel permits a semi-analytical approach [114–116], which allows for a detailed characterization of the stability of the solutions and their bifurcations. Notably, we expose here that the emergence of spirals is explained by a series of bifurcations from a homogeneous state. Furthermore, it is observed that the transition from static to moving spiral chimeras triggers the formation of filaments within their incoherent core, through a sequence of saddle-node bifurcations, similar to the slanted snaking bifurcation observed in other non-local systems [41, 117–119].

IOP Publishing New J. Phys. 25 (2023) 103023 https://doi.org/10.1088/1367-2630/acfd4f

New Journal of Physics
The open access journal at the forefront of physics

Published in partnership with: Deutsche Physikalische Gesellschaft and the Institute of Physics

OPEN ACCESS

RECEIVED
14 June 2023

REVISED
16 September 2023

ACCEPTED FOR PUBLICATION
26 September 2023

PUBLISHED
13 October 2023

PAPER

Traveling spiral wave chimeras in coupled oscillator systems: emergence, dynamics, and transitions

M Bataille-Gonzalez[1], M G Clerc[1], E Knobloch[2] and O E Omel'chenko[3,*]

[1] Departamento de Física and Millennium Institute for Research in Optics, Facultad de Ciencias Físicas y Matemáticas, Universidad de Chile, Santiago, Chile
[2] Department of Physics, University of California at Berkeley, Berkeley, CA 94720, United States of America
[3] Institute of Physics and Astronomy, University of Potsdam, Karl-Liebknecht-Str. 24/25, 14476 Potsdam, Germany
[*] Author to whom any correspondence should be addressed.

E-mail: omelchenko@uni-potsdam.de

Keywords: coupled oscillators, chimera state, spiral wave, drift

Supplementary material for this article is available online

Abstract

Systems of coupled nonlinear oscillators often exhibit states of partial synchrony in which some of the oscillators oscillate coherently while the rest remain incoherent. If such a state emerges spontaneously, in other words, if it cannot be associated with any heterogeneity in the system, it is generally referred to as a chimera state. In planar oscillator arrays, these chimera states can take the form of rotating spiral waves surrounding an incoherent core, resembling those observed in oscillatory or excitable media, and may display complex dynamical behavior. To understand this behavior we study stationary and moving chimera states in planar phase oscillator arrays using a combination of direct numerical simulations and numerical continuation of solutions of the corresponding continuum limit, focusing on the existence and properties of traveling spiral wave chimeras as a function of the system parameters. The oscillators are coupled nonlocally and their frequencies are drawn from a Lorentzian distribution. Two cases are discussed in detail, that of a top-hat coupling function and a two-parameter truncated Fourier approximation to this function in Cartesian coordinates. The latter allows semi-analytical progress, including determination of stability properties, leading to a classification of possible behaviors of both static and moving chimera states. The transition from stationary to moving chimeras is shown to be accompanied by the appearance of complex filamentary structures within the incoherent spiral wave core representing secondary coherence regions associated with temporal resonances. As the parameters are varied the number of such filaments may grow, a process reflected in a series of folds in the corresponding bifurcation diagram showing the drift speed s as a function of the phase-lag parameter α.

1. Introduction

Coupled oscillator systems have played a fundamental role in our understanding and modeling of physical systems since the seminal work of Huygens [1, 2]. More recently, coupled oscillator systems have been used to model certain aspects of neural activity in the brain [3–5], collective dynamics of cilia carpets coupled by hydrodynamic interaction [6, 7], as well as oscillatory and excitable media such as those modeling chemical oscillations [8–11]. In all these examples the key question of interest is the extent of synchronization, both in frequency and in phase, within the oscillator population and its dependence on the oscillator properties and the nature of their coupling. Systems of two coupled oscillators are well described by the Adler equation [12] for the phase difference between the oscillators, but substantial progress is possible in the limit of an infinite number of oscillators, both with all-to-all coupling and with sparse coupling corresponding to different types of oscillator networks. The theory distinguishes between a phase description, in which the amplitude dynamics are adiabatically eliminated, and an amplitude-phase description that is required for highly nonlinear systems. In either case one tends to find clusters of synchronized oscillators, that is, states of partial synchrony. The theory has numerous key applications, ranging from coupled laser arrays [13] used to maximize power output to the working of the electrical power grid [14]. In each case the identification of the clusters, their number and extent, as well as their stability, represent a major challenge to our understanding of large arrays of coupled oscillators.

If the oscillators are identical and interact attractively, one may expect that all will ultimately oscillate in synchrony. That this is not inevitable was pointed out in 2002 by Kuramoto and Battogtokh [15], who discovered a remarkable state of partial synchrony in a system of coupled identical phase oscillators, in which a subset of the oscillators synchronizes but the remainder remains incoherent. Subsequently called chimera states [16], these states of partial synchrony have been studied by numerous authors in recent years [17–22]. In the simplest case, the oscillators are on a ring and coupled nonlocally via a periodic coupling function. In the presence of a phase lag α in the coupling, the resulting coherent region may drift through the system [23], with oscillators at the leading edge kicked into synchrony while those at the trailing edge fall out of synchrony, thereby maintaining, at least approximately, a constant size of the traveling coherent region. The dynamics of these synchronization and desynchronization fronts thus provide a key to the understanding of the formation of traveling chimera states and their stability properties.

Chimera states are also found in systems of nonidentical oscillators. While less surprising, the resulting states of partial synchrony exhibit similar properties, and in particular motion, whenever the parameter α is nonzero. We distinguish this type of system, in which motion arises spontaneously, from situations in which the motion is forced, for example, via an asymmetrical coupling function [24].

While studies of one-dimensional coupled oscillator arrays are common, similar studies of two- or even three-dimensional oscillator arrays are less frequent. In planar arrays of identical oscillators, one tends to find incoherent cores, surrounded by a rotating coherent spiral wave [25–27] somewhat reminiscent of the rotating spiral waves familiar from oscillatory or excitable media [28, 29]. One may also find coherent cores embedded in an incoherent background [30, 31], although stripe and spot patterns are also possible [32]. In some cases, these may become destabilized via a Hopf bifurcation, leading either to standing oscillating chimera states or to traveling structures as predicted by abstract theory [33]. Three-dimensional arrays support a greater variety of states, most of which are only known via direct numerical simulations [34]. Remarkably, in the special case of a sinusoidal coupling function it is possible to establish the existence and stability properties of such states *semi-analytically* [31, 35, 36], and in particular to predict the onset of spontaneous motion and even the *stability* of the resulting moving structures. This is so even though the transition from stationary to time-dependent chimeras is accompanied in general by the appearance of complex filamentary structures within the incoherent core representing secondary coherence regions associated with temporal resonances between the spiral wave frequency and the spatial translation. These structures, first observed in [35], are a property of quasiperiodic states as explained in [31], and form regardless of whether this state is a standing oscillation as in [31, 35] or, as shown here, a traveling chimera. We show here that the properties of these resonance structures are responsible for much of the remarkable complexity of the associated bifurcation diagram.

Most of the above results have been obtained using Kuramoto's model of phase-coupled oscillators, although some recent work has been devoted to more realistic oscillator systems, among which coupled Stuart-Landau oscillator systems are most popular [37]. However, arrays of both coupled van der Pol oscillators [38] and coupled FitzHugh–Nagumo oscillators [10] have also been studied from this point of view. These models extend the work on the Kuramoto model to include amplitude dynamics in addition to the phases, and in the case of the van der Pol oscillators, to coupled relaxation oscillators, i.e. to oscillators with a strongly nonlinear phase evolution, as well as to excitable systems.

From an experimental perspective, there is a great deal of evidence for the existence of chimera states in one-dimensional arrays of coupled oscillators [8, 11, 39–42], while two-dimensional oscillator arrays (not to mention three-dimensional arrays) remain poorly studied. To the best of our knowledge, the only example of their laboratory realization involves nonlocally coupled Belousov–Zhabotinsky chemical oscillators [8, 9]. In these experiments, spiral wave chimeras were indeed observed, but usually in the form of moving structures. In some cases, this motion resembles a two-dimensional random walk that may be associated with finite-size fluctuations by analogy with one-dimensional systems [43]. On the other hand, spiral wave chimeras with persistent drift motion were also reported. Motivated by the latter observation, we seek the simplest model for studying such drifting structures, and one that allows a detailed study of the emergence and stability properties of uniformly drifting spiral wave chimeras and their parameter dependence, as well as their relationship to other synchronization patterns in the system.

Since the mathematics behind traveling partially coherent states in more realistic systems involving both amplitude and phase dynamics remains largely beyond current reach, we revisit here the Kuramoto model, within which traveling structures can be simulated and, depending on the coupling function adopted, computed semi-analytically, at least in the continuum limit described by the Ott–Antonsen ansatz [44]. It is important to realize that for identical oscillators the Ott–Antonsen approach precludes a simple self-consistent description of traveling chimera states (see [45, lemma 2] and [46, section 4]). However, this is no longer the case when the oscillators are nonidentical, and in this paper we therefore assume that the oscillator frequencies are drawn from a Lorentzian frequency distribution of width γ. Thus γ becomes an additional (and key) parameter of the system that manifests itself as a damping term in the continuum description.

In recent work [47] we have studied a discrete two-dimensional oscillator system of this type with a nonlocal coupling function and showed that this system is able to support bound states of two counter-rotating spiral waves with incoherent cores that drift either rigidly or exhibit more complex meandering motion. The specific example considered in [47] was a two-dimensional array of phase oscillators $\{\theta_{jk}(t)\}_{j,k=1}^{N}$ evolving according to

$$\frac{\mathrm{d}\theta_{jk}}{\mathrm{d}t} = \omega_{jk} - \frac{1}{|B_\sigma(j,k)|} \sum_{(m,n)\in B_\sigma(j,k)} \sin\left(\theta_{jk} - \theta_{mn} + \alpha\right). \tag{1}$$

This equation implies that each oscillator (j,k) interacts only with its neighbors within the circular region

$$B_\sigma(j,k) = \left\{(m,n)\,:\,(m-j)^2 + (n-k)^2 \leqslant \sigma^2 N^2\right\},$$

where the distances $m-j$ and $n-k$ are considered mod N and $\sigma \in (0, 1/2)$ is the relative coupling radius. The interaction is normalized by the number of points $|B_\sigma(j,k)|$ in the region $B_\sigma(j,k)$ and involves a phase lag parameter $\alpha \in [0, \pi/2)$. In addition, it is assumed that the oscillators are heterogeneous in the sense that their natural frequencies ω_{jk} are drawn randomly and independently from a Lorentzian distribution

$$g(\omega) = \frac{\gamma}{\pi}\frac{1}{\gamma^2 + \omega^2} \tag{2}$$

of width $\gamma > 0$.

The system (1) was found to exhibit a large variety of different moving spiral wave chimeras associated with the complex spatial structure of their incoherent cores, as summarized in figure 1 for two different values of the phase lag parameter α. In particular, these states exhibit staggered coexistence as a function of α (see below), behavior that is associated with different numbers of crescent-shaped filaments in the core of a moving spiral, hereafter referred to as fingerprint patterns (see figure 1(b–d)). Similar slanted snaking bifurcation diagrams have been observed for spatially localized states in both fluid and optical systems [48–52] and are a consequence of the nonlocal nature of the system (1). As a result the relationship between the presence of stable, albeit moving chimera states and the system parameters is exceedingly intricate and remains to be elucidated.

In this paper we are able to identify, for the first time, the main prerequisites necessary for the emergence of moving spiral wave chimeras of different types and to establish their stability properties. To this end we formulate a version of problem (1) that is tractable semi-analytically, and employ extensive numerical continuation to follow distinct states through parameter space, together with their stability properties. This approach builds a picture of the parameter space of the problem, enables us to identify the different chimera states that are possible, and ultimately allows a detailed understanding of the system. Our results are corroborated using extensive direct numerical simulations of this system and provide a roadmap for understanding more realistic coupled oscillator systems.

2. Results

The model (1) is a particular case of a more general nonlocally coupled system

$$\frac{\mathrm{d}\theta_{jk}}{\mathrm{d}t} = \omega_{jk} - \left(\frac{2\pi}{N}\right)^2 \sum_{m,n=1}^{N} G_{jk;mn} \sin\left(\theta_{jk} - \theta_{mn} + \alpha\right) \tag{3}$$

with

$$G_{jk;mn} = G\left(\frac{2\pi(j-m)}{N}, \frac{2\pi(k-n)}{N}\right),$$

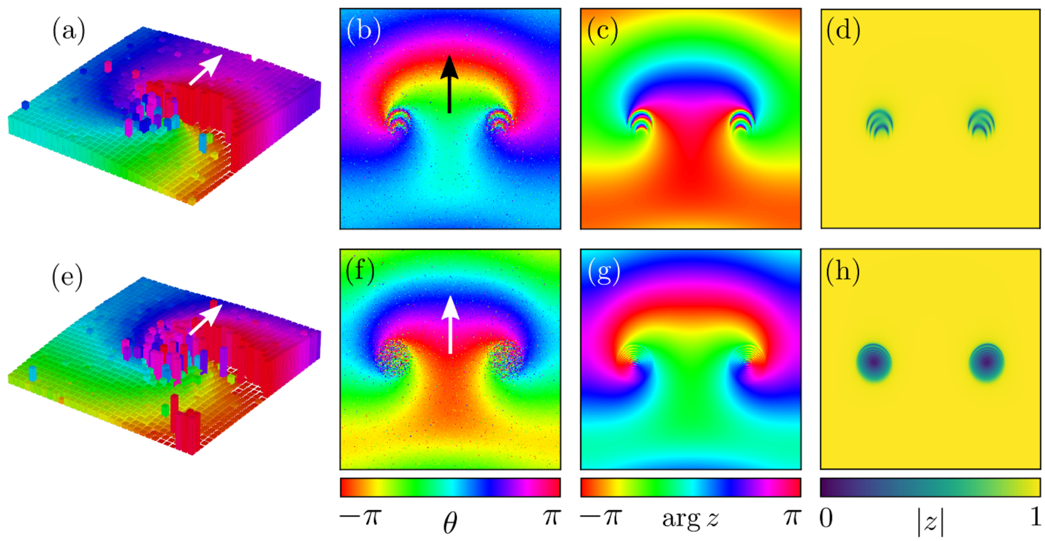

Figure 1. Moving spiral wave chimeras (two left columns) in the discrete oscillator array (1) and their continuum limit counterparts (two right columns) determined from equation (6). The arrows indicate the drift direction. Panels (a) and (e) focus on the behavior of the phase near a single spiral core while panels (b) and (f) present snapshots of the corresponding phase $\theta_{jk}(t)$ of the full array of oscillators, revealing the presence of a pair of incoherent spiral cores surrounded by a coherent region in the form of a rotating spiral. The pattern moves in the y direction at a constant speed. Under appropriate conditions, the incoherent cores break up into nested filamentary structures (panels (b) and (c)). Panels (c) and (g) show snapshots of $\arg z(x,y,t)$ while panels (d) and (h) show snapshots of $|z(x,y,t)|$, a representation that eliminates the global spiral wave frequency Ω and focuses on the fingerprint structure of their spiral cores. The continuum limit evidently provides an accurate description of the discrete system, even for a moderate number of oscillators. The supplementary material [53] provides an animation of the state in panels (c) and (g). Parameters: $N=128$, $\gamma=0.01$, $\sigma=0.25$ with $\alpha=0.6$ (top row) and $\alpha=0.7$ (bottom row).

where $G(x,y)$ is a non-constant coupling function, which is 2π-periodic with respect to x and y and satisfies the symmetry conditions

$$G(-x,y)=G(x,-y)=G(-x,-y)=G(x,y) \tag{4}$$

and the normalization condition

$$\int_{-\pi}^{\pi}\int_{-\pi}^{\pi} G(x,y)\,\mathrm{d}x\,\mathrm{d}y=1.$$

Indeed, if we assume

$$G(x,y)=\begin{cases} 1/\left(\pi^3\sigma^2\right) & \text{for} \quad x^2+y^2\leqslant \pi^2\sigma^2, \\ 0 & \text{for} \quad x^2+y^2>\pi^2\sigma^2 \end{cases} \tag{5}$$

in the square domain $(x,y)\in[-\pi,\pi]^2$, then equation (3) reduces to model (1). The resulting coupling function $G(x,y)$ is shown in figure 2(a).

It is well-known [19, 54, 55] that in the continuum limit $N\to\infty$ the long-term dynamics of equation (3) settle down on the Ott–Antonsen manifold parametrized by a complex-valued function $z(x,y,t)$. This function is the local order parameter at the position (x,y) at time t and quantifies the synchronization degree of oscillators $\theta_{jk}(t)$ with $(-\pi+2\pi j/N,-\pi+2\pi k/N)\approx(x,y)$. Importantly, in the case of Lorentzian-distributed natural frequencies ω_{jk} the evolution of $z(x,y,t)$ is described by the integro-differential equation

$$\frac{\mathrm{d}z}{\mathrm{d}t}=-\gamma z+\frac{1}{2}\mathrm{e}^{-\mathrm{i}\alpha}\mathcal{G}z-\frac{1}{2}\mathrm{e}^{\mathrm{i}\alpha}z^2\mathcal{G}\bar{z}, \tag{6}$$

where the damping parameter $\gamma>0$ is determined by the width of the distribution in equation (2) and

$$(\mathcal{G}z)(x,y,t)=\int_{-\pi}^{\pi}\mathrm{d}x'\int_{-\pi}^{\pi}G(x-x',y-y')\,z(x',y',t)\,dy'$$

is a convolution-type integral operator with the coupling function $G(x,y)$ from (3). The above observation allows us to use equation (6) as a mathematical tool for investigating the properties of moving spiral wave chimeras in the system (3).

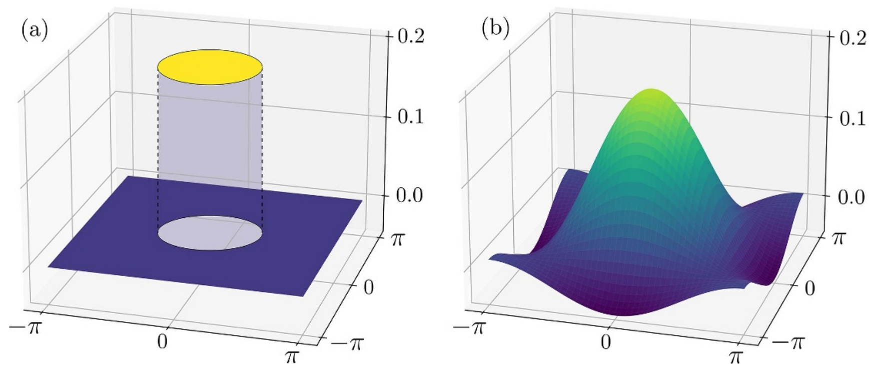

Figure 2. Two examples of coupling functions considered in this paper. (a) Top-hat function with $\sigma = 0.4$. (b) The trigonometric function (10) with $A = 1.63$ and $B = 2.62$, corresponding to the leading order Fourier approximation of the top-hat function with $\sigma = 0.4$.

The discrete system (3) is invariant under discrete translations in two directions, while the continuum description (6) is invariant under continuous translations. Both are in addition invariant with respect to the group D_4 of rotations and reflections of a square inherited from the coupling function. The problem (6) is therefore invariant under the group $T^2 \dot{+} D_4$, the semidirect product of the two-torus of translations and the discrete group D_4. The solutions of this problem may respect certain subgroups of this symmetry group or have no symmetry. This observation applies to both stationary and drifting states. In particular, every uniformly drifting state satisfying equation (6), including the simplest moving spiral wave chimeras, corresponds to a solution of the form

$$z(x,y,t) = a\left(x - s_x t, y - s_y t\right) \mathrm{e}^{\mathrm{i}\Omega t}, \tag{7}$$

where $(s_x, s_y)^\mathrm{T} \in \mathbb{R}^2$ is the velocity vector and $\Omega \in \mathbb{R}$ is the collective phase frequency. In the case $s_x = s_y = 0$, the pattern is called motionless or stationary. If, in addition, we also have $\Omega = 0$, the corresponding pattern is called static.

From the symmetry conditions (4) it follows that among all possible moving solutions (7) there are two special solution types related to these symmetries: solutions of the form

$$z(x,y,t) = a\left(x, y - st\right) \mathrm{e}^{\mathrm{i}\Omega t} \tag{8}$$

with $s \in \mathbb{R}$ and $a(-x,y) = a(x,y)$ (hereafter Z_2 symmetry) corresponding to uniform motion in the y direction, and solutions of the form

$$z(x,y,t) = a\left(x - st, y - st\right) \mathrm{e}^{\mathrm{i}\Omega t} \tag{9}$$

with $s \in \mathbb{R}$ and $a(y,x) = a(x,y)$ (hereafter $\tilde{Z}_2$ symmetry), corresponding to uniform motion along a diagonal. We refer to these solutions as *symmetric* spiral waves but distinguish them by their symmetries Z_2 and $\tilde{Z}_2$ under reflection. Note that rotations by 90° rotate a Z_2-symmetric state into another Z_2-symmetric state, and similarly for $\tilde{Z}_2$-symmetric states.

2.1. Top-hat coupling function

The bifurcation diagram for Z_2-symmetric spiral wave chimeras (8) with the top-hat coupling function (5) with $\sigma = 0.4$ is shown in figure 3. The diagram shows the speed s as a function of the phase lag parameter α, obtained by inserting ansatz (8) into equation (6), discretizing the resulting equation on a square grid with 128 nodes in x and y directions and using an arc-length continuation scheme and a standard Newton solver to follow the branch of equilibria of the resulting system of 128×64 nonlinear equations. (Note that owing to the reflection symmetry of $a(x,y)$, the number of equations is reduced by half.) This procedure allows us to compute both stable and unstable solutions; in all cases, the predictions of this approach were confirmed using direct numerical simulations of the discrete system (1).

Figure 3 identifies four key regions in this diagram with different behavior. Enlargements of regions I and II are included in the figure together with solution snapshots at the locations labeled in the bifurcation diagram. These depict $|z|$ in the left half of each panel and $\arg z$ in the right half and show that the sequence of folds in regions I and II is associated with an increasing number of filamentary structures in the spiral

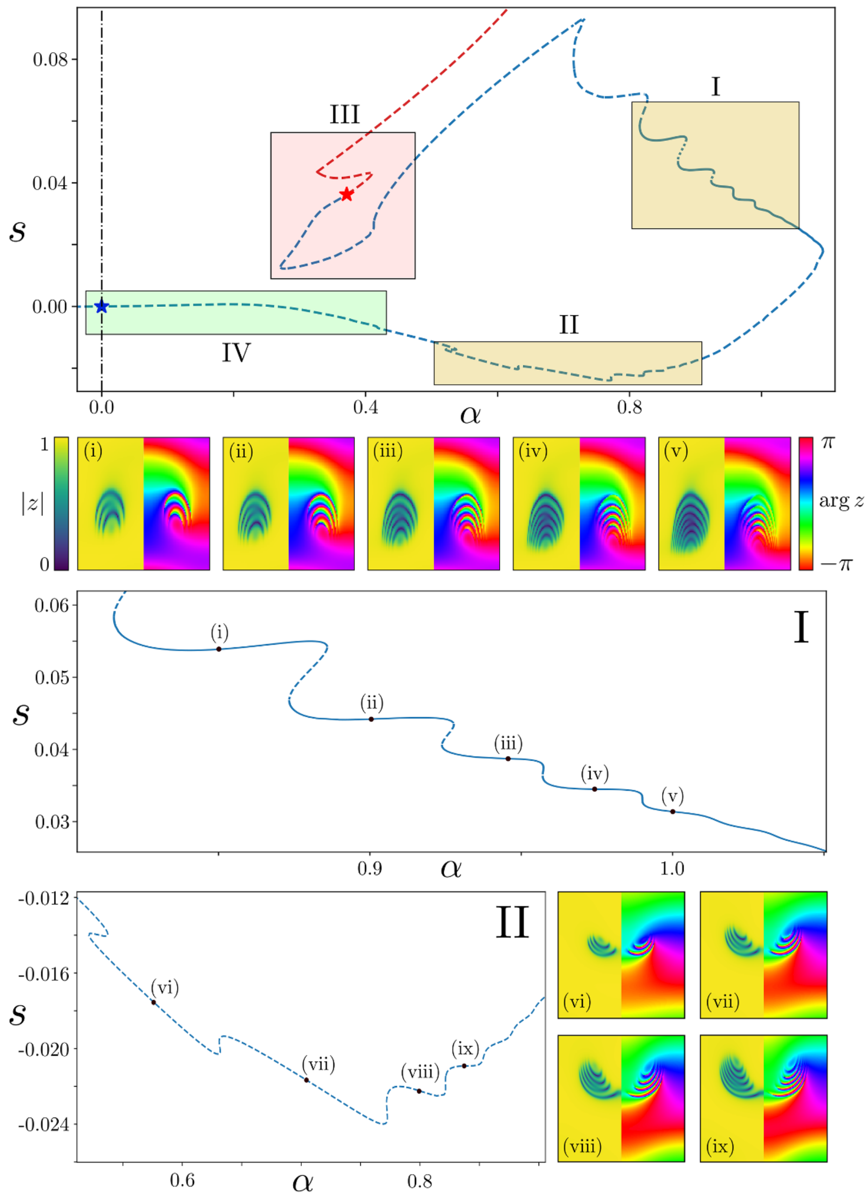

Figure 3. The speed s of symmetric spiral wave chimeras moving in the y direction versus the phase lag parameter α in equation (6) for the top-hat coupling function with $\sigma = 0.4$ and $\gamma = 0.01$. Four regions of distinct behavior are indicated, two of which are enlarged in the figure and accompanied by snapshots of the solutions at the locations indicated. The snapshots show the whole solution, with $|z|$ in the left half of each panel and arg z in the right half. The supplementary material [53] shows an animation indicating how the solution profile changes along the solution branch in the top panel starting from $\alpha = 0$ and confirms that the folds in regions I and II are associated with the successive addition of new filamentary structures in the spiral cores in a behavior that resembles slanted snaking. Solid (dashed) lines indicate stability (instability).

cores as α increases. In both regions the bifurcation diagram resembles slanted snaking [48–52]. As discussed below, these filamentary structures are a consequence of the two-frequency nature of the traveling chimera state: its global oscillation frequency Ω and its translation frequency determined by the speed s.

Figures 4 and 5 show the corresponding behavior in regions III and IV. The former shows the gradual approach of the two cores to one another along the branch, resulting in the presence of filaments that extend across the whole domain beyond the location indicated by the red star, while the latter shows the gradual onset of the translation motion from $\alpha = 0$ until $\alpha = 0.4$ where the speed s is large enough for prominent filaments to be present in the spiral cores. Finally, figure 6 shows the effects of decreasing the top-hat radius σ on the behavior in region I. We observe that as σ decreases so does the corresponding value of α resulting in smaller speed s and a smaller spiral core, all for a given number of core filaments. Overall, however, the behavior remains qualitatively unchanged.

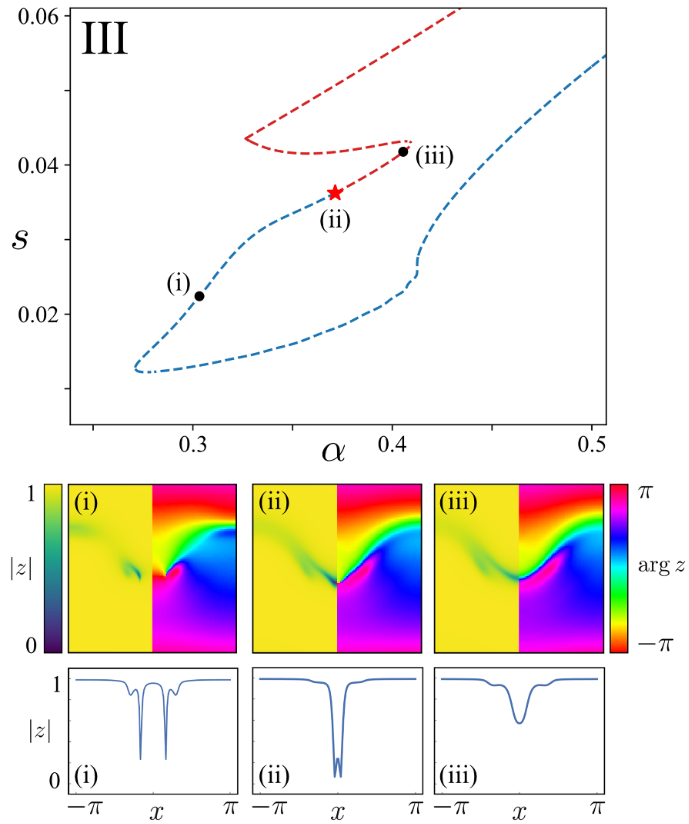

Figure 4. Detail of region III of figure 3 showing the coalescence of two spiral cores and the creation of an extended filament. The bottom panels present the cross section of $|z|$ at $y = 0$.

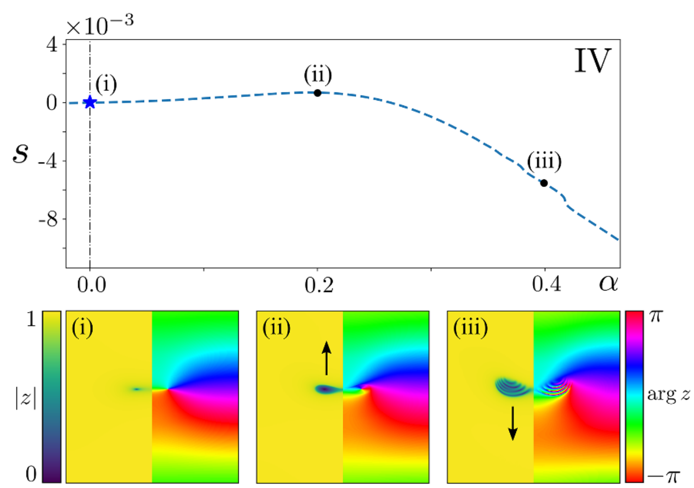

Figure 5. Detail of region IV of figure 3 showing the onset of motion for two-core spiral chimeras as α increases from zero and the subsequent development of filamentary structures in the spiral cores at larger speeds s. The black arrows indicate the direction of propagation.

We remark that even with a relatively small number of discretization points the time needed to calculate the diagram shown in figure 3 turned out to be extremely long (ca. 6 weeks on a dedicated computer with large RAM). In contrast, the results we are going to describe in the next section were obtained much more rapidly (ca. 3–4 days on a laptop with a double number of discretization points in each direction). This remarkable computational speed-up was achieved thanks to the use of a special analytical technique for

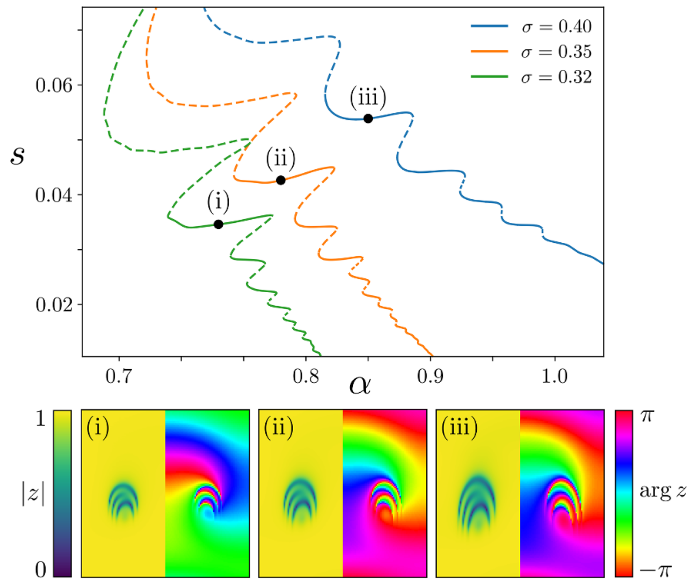

Figure 6. Detail of region I of figure 3 for different values of the coupling radius σ. Increasing σ displaces the branch to larger α resulting in larger speed s and a larger spiral core.

calculating periodic orbits in the Ott–Antonsen manifold proposed in [56] by one of the authors of this paper.

2.2. Trigonometric coupling function

The results for the top-hat coupling function (5) illustrate some of the complexities inherent in the present problem. Since our ultimate goal is to understand the properties of spiral wave chimeras in the case of general coupling functions $G(x,y)$, we need a deeper analytical approach to this problem. This becomes possible if we limit ourselves to a narrower class of D_4-symmetric functions of the form

$$G(x,y) = \frac{1}{(2\pi)^2}\left(1 + A(\cos x + \cos y) + B\cos x\cos y\right), \tag{10}$$

where A and B are real parameters such that $A^2 + B^2 \neq 0$. This expression arises as a truncation of a Fourier series representation of the coupling function $G(x,y)$, assumed to be an absolutely integrable 2π-periodic function:

$$G(x,y) = \sum_{n,m=-\infty}^{\infty} \hat{g}_{nm} \mathrm{e}^{\mathrm{i}(nx+my)}, \tag{11}$$

where

$$\hat{g}_{nm} = \frac{1}{(2\pi)^2}\int_{-\pi}^{\pi}\int_{-\pi}^{\pi} G(x,y)\,\mathrm{e}^{-\mathrm{i}(nx+my)}\,\mathrm{d}x\,\mathrm{d}y.$$

Moreover, if this function satisfies (4), then

$$\hat{g}_{-n,m} = \hat{g}_{n,-m} = \hat{g}_{-n,-m} = \hat{g}_{n,m}.$$

In addition, if its integral is normalized to the identity,

$$\int_{-\pi}^{\pi}\int_{-\pi}^{\pi} G(x,y)\,\mathrm{d}x\,\mathrm{d}y = 1,$$

then $\hat{g}_{0,0} = 1/(2\pi)^2$. The simplest non-constant truncation of (11) is obtained on keeping terms with indices $n, m = 0, \pm 1$ only, leading to (10) with

$$A = 8\pi^2\hat{g}_{1,0}, \qquad B = 16\pi^2\hat{g}_{1,1}.$$

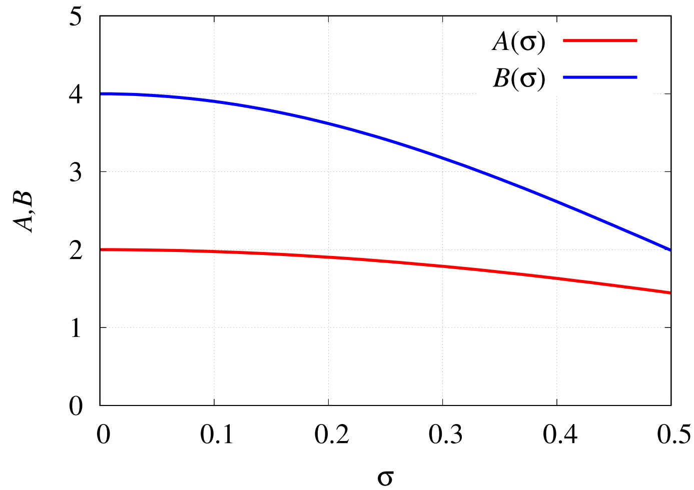

Figure 7. The parameters A and B in equation (10) corresponding to the leading order Fourier approximation to the top-hat coupling function (5) with different σ.

For example, if we calculate the Fourier coefficients $\hat{g}_{1,0}$ and $\hat{g}_{1,1}$ of the top-hat coupling function (5) and insert them in the above formulas, we obtain the fit $\sigma \mapsto (A(\sigma), B(\sigma))$ shown in figure 7.

In the following we study the resulting spiral chimeras as a function of the coefficients A and B in the relevant range revealed by figure 7, together with their stability properties, starting with stationary two-core chimeras for $\alpha = 0$. The damping parameter γ is fixed at $\gamma = 0.01$.

2.3. Static patterns

For $\alpha = 0$ equation (6) is variational and all chimera states are therefore time-independent and motionless, and correspond to equilibria of the form

$$z(x,y,t) = a(x,y).$$

In section 3.1 below, we construct the self-consistency equation determining these equilibria and explain how we solve it. In addition, we describe how the linear stability analysis of such equilibria can be performed. Using these mathematical tools, we calculate bifurcation diagrams for various values of the coupling parameters A and B. Specifically, we show that all static solutions of equation (6) with the coupling function (10) and $\alpha = 0$, including two-core chimeras, have the form

$$a(x,y) = \frac{w(x,y)}{\gamma + \sqrt{\gamma^2 + |w(x,y)|^2}}, \tag{12}$$

where

$$w(x,y) \in \mathrm{Span}\{1, \cos x, \cos y, \sin x, \sin y, \cos x \cos y, \cos x \sin y, \sin x \cos y, \sin x \sin y\}.$$

Patterns with symmetry under the reflection $x \to -x$, i.e. with $a(-x,y) = a(x,y)$, are Z_2-symmetric, and are described by a subset of the admissible functions $w(x,y)$, namely

$$w(x,y) \in \mathrm{Span}\{1, \cos x, \cos y, \sin y, \cos x \cos y, \cos x \sin y\},$$

while patterns satisfying $a(y,x) = a(x,y)$, i.e. with reflection symmetry in the diagonal, are $\tilde{Z}_2$-symmetric, and are described by functions $w(x,y)$ of the form

$$w(x,y) \in \mathrm{Span}\{1, \cos x + \cos y, \sin x + \sin y, \cos x \cos y, \sin x \sin y\}.$$

Among these states we distinguish between *fundamental* states that are independent of the parameter B in (10), and *compound* states that depend on B. The former include the following:

(a) Completely incoherent state

$$a(x,y) = 0.$$

(b) Partially coherent uniform state

$$a(x,y) = \sqrt{1-2\gamma}, \qquad \gamma < 1/2.$$

(c) Partially coherent splay state

$$a(x,y) = q\mathrm{e}^{\mathrm{i}y}, \qquad q \in (0,1).$$

(d) Generalized antiphase state

$$a(x,y) = \frac{p + \mathrm{i}q\sin y}{\gamma + \sqrt{\gamma^2 + p^2 + q^2\sin^2 y}}, \quad p \geqslant 0,\ q > 0,$$

called an antiphase state when $p = 0$.

(e) Planar state

$$a(x,y) = \frac{p + r\cos y + \mathrm{i}q\sin y}{\gamma + \sqrt{\gamma^2 + (p + r\cos y)^2 + q^2\sin^2 y}}$$

with $p, r, q > 0$.

(f) Four-core spiral pattern

$$a(x,y) = \frac{q(\cos x + \mathrm{i}\sin y)}{\gamma + \sqrt{\gamma^2 + q^2(\cos^2 x + \sin^2 y)}}, \qquad q > 0.$$

(g) Generalized four-core spiral pattern

$$a(x,y) = \frac{p\cos x + r\cos y + \mathrm{i}q\sin y}{\gamma + \sqrt{\gamma^2 + (p\cos x + r\cos y)^2 + q^2\sin^2 y}}$$

with $p, r, q > 0$.

The above states are all Z_2-symmetric, but similar expressions can be written for fundamental $\tilde{Z}_2$-symmetric states. This is a consequence of the following.

2.3.1. Equivalence of the cases $A = 0$ and $B = 0$

From the identity

$$\frac{1}{(2\pi)^2}(1 + B\cos x\cos y) = \frac{1}{(2\pi)^2}\left(1 + \frac{B}{2}(\cos(x-y) + \cos(x+y))\right)$$

it follows that every pattern observed for $(A,B) = (A_0, 0)$ has its counterpart rotated by the angle $\pi/4$ and observed for $(A,B) = (0, 2A_0)$. Therefore, the dynamics of equation (6) in the case $A = 0$ and in the case $B = 0$ are identical modulo the above spatial rotation and rescaling. This result is independent of the value of the phase lag parameter α.

2.4. Bifurcation diagrams for static patterns

Thanks to the simplicity of the above formulas, the existence and stability properties of the completely incoherent state, the partially coherent uniform state and the partially coherent splay state can be described comprehensively. In particular, in section 3.1 we show that:

(i) the completely incoherent state is linearly stable if $\gamma \geqslant \max(1/2, A/4, B/8)$ and unstable otherwise,
(ii) the partially coherent uniform state exists only for $\gamma < 1/2$ and is linearly stable if $A \leqslant 2$ and $B \leqslant 4$ and unstable otherwise.

The stability analysis of the partially coherent splay state can be performed by generalizing the analytical scheme proposed in [35, 57]; the stability analysis for four-core spiral patterns in the case $B = 0$ was performed in [31, 36].

To display our results, including stability results, we employ the global order parameter

$$R \equiv \frac{1}{(2\pi)^2}\left|\int_{-\pi}^{\pi}\int_{-\pi}^{\pi} a(x,y)\,\mathrm{d}x\,\mathrm{d}y\right|. \tag{13}$$

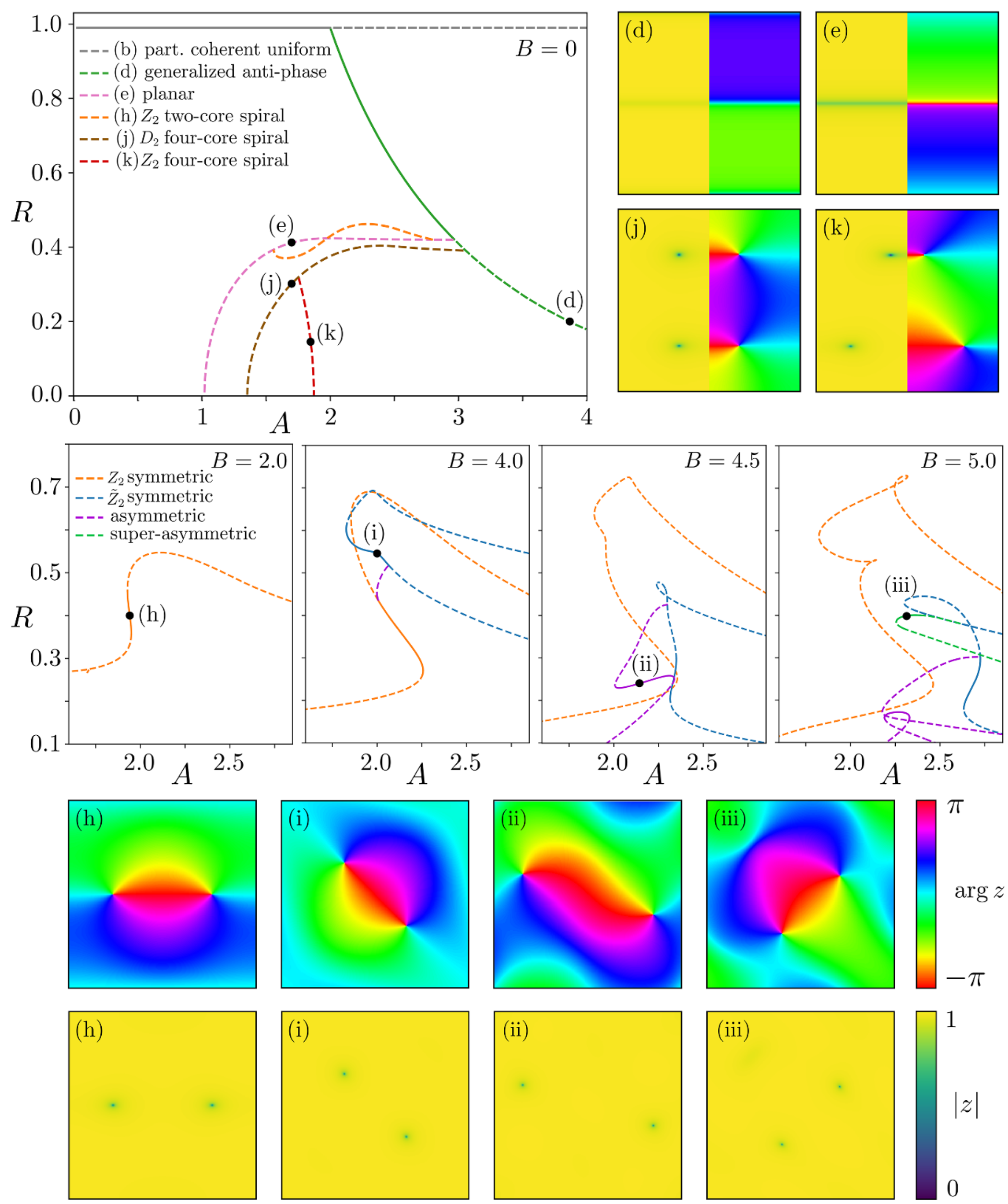

Figure 8. The $B = 0$ panel (top left) shows the global order parameter R for different static solutions of equation (6) with the trigonometric coupling function (10) and $\alpha = 0$ as a function of the parameter A. The four other panels with $B > 0$ show only two-core spiral chimeras, namely Z_2-symmetric chimera states (orange curves), $\tilde{Z}_2$-symmetric chimera states (blue curves), asymmetric chimera states (purple curves), and super-asymmetric chimera states (light green curve). Stable (unstable) states are shown in solid (dashed) lines. Snapshots at the top right and at the bottom show sample stable states in terms of arg z and $|z|$.

However, a number of the states listed above have the same global order parameter, $R = 0$, as the completely incoherent state. To distinguish among these states, we introduce the quantity

$$S = \frac{1}{(2\pi)^2} \left| \int_{-\pi}^{\pi} \int_{-\pi}^{\pi} a(x,y) \sin y \, dx \, dy \right| \tag{14}$$

measuring the contribution of $\sin y$ in the Fourier expansion of $a(x,y)$.

Figure 8, top panel, shows the global order parameter R for static states computed from equation (6) for different values of the parameter A in equation (10) when $B = 0$, $\alpha = 0$. We observe:

(i) $B = 0$: the partially coherent uniform state $R = \sqrt{1 - 2\gamma}$ (gray line, state (b)) becomes unstable through a pitchfork of revolution at $A = 2$. This bifurcation gives rise to fundamental Z_2-symmetric states

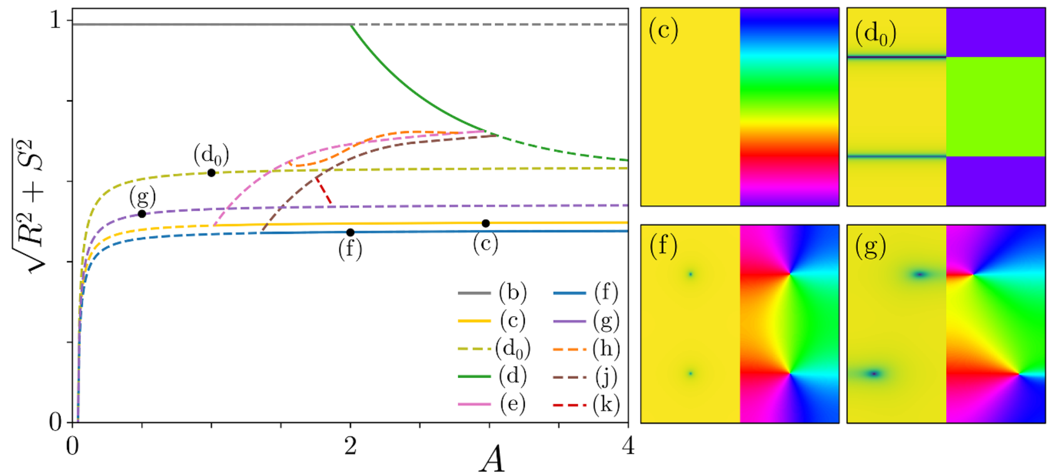

Figure 9. Static patterns $z = a(x,y)$ from equation (6) for different values of the parameter A in equation (10) when $B = 0$, $\alpha = 0$, shown in terms of the quantity $\sqrt{R^2+S^2}$ with R and S defined in equations (13) and (14) for comparison with figure 8, top panel. Corresponding branches are indicated by like colors, while stable (unstable) states are shown in solid (dashed) lines. The yellow branch shows the partially coherent splay state, while the blue line shows the D_4-symmetric four-core spiral chimera. Snapshots at the right show sample states in terms of $|z|$ and arg z.

(green curve, state (d)). For this state $|a(x,y)|$ has period π in the y direction. These states lose stability at a secondary pitchfork bifurcation creating a branch of fundamental Z_2-symmetric solutions with period 2π in $|a(x,y)|$ in the y direction (pink curve, state (e)). This new arc-shaped branch in figure 8(a) is everywhere unstable and connects the green branch of period π states with the branch of partially coherent splay states with $R = 0$.

Along the pink branch of period 2π states there are two tertiary pitchfork bifurcation points, with a S-shaped branch of Z_2-symmetric states modulated in both x and y directions in between (orange curve, state (h)). These states correspond to stationary compound Z_2-symmetric two-core spiral chimeras and so depend on the parameter B. At $B = 0$ these states are all unstable (dashed orange curve).

On the dashed brown branch we find unstable compound $D_2 = Z_2^2$-symmetric four-core chimeras (state (j)) described by the formula (12) with $w(x,y) \in \mathrm{Span}\{1, \cos x, \sin y, \cos x \sin y\}$. This branch connects the period π fundamental states with the fundamental D_4-symmetric four-core chimeras with $R = 0$. A tertiary branch of unstable compound states (dashed red curve, state (k)) bifurcates from the brown branch.

(ii) $B = 0$: to distinguish between the different states with $R = 0$ we show in figure 9 the same bifurcation diagram but showing the quantity $\sqrt{R^2+S^2}$ as a function of A instead of R. In this figure, the yellow line shows the partially coherent splay states (state (c)), while the blue line corresponds to D_4-symmetric four-core spiral chimeras (state (f)). We see that each of these states bifurcates from the completely incoherent state $a(x,y) = 0$ at $A = 4\gamma$ and loses stability with decreasing A in subcritical bifurcations, generating unstable states with $R > 0$. Moreover, two other unstable fundamental branches, a branch of anti-phase states (light green curve, state (d$_0$)) and a branch of generalized four-core patterns (dark purple curve, state (g)) also emerge at the same parameter value, $A = 4\gamma$, indicating the highly degenerate nature of this point.

(iii) $B > 0$: figure 8 shows how the behavior of the compound states changes with the coefficient B in the coupling function. The figure shows that while the fundamental Z_2-symmetric solution is independent of B its stability may change as B changes. A similar statement applies to fundamental $\tilde{Z}_2$-symmetric solutions. The stability of tertiary states may likewise change. In particular, at $B = 2$, there appears a narrow parameter range $A \approx (1.93, 1.95)$ with stable Z_2-symmetric two-core spiral chimeras. This range corresponds to the segment of the orange solution branch with negative slope.

(iv) At $B = 4$, the segment of the orange branch with negative slope is broader but the stability range of Z_2-symmetric spiral chimeras is limited by a (subcritical) quaternary bifurcation to (unstable) asymmetric two-core states (purple branch) that connect the states with Z_2 symmetry to similar states with $\tilde{Z}_2$ symmetry (blue branch, state (i)). By asymmetric we mean any state that is neither Z_2- nor

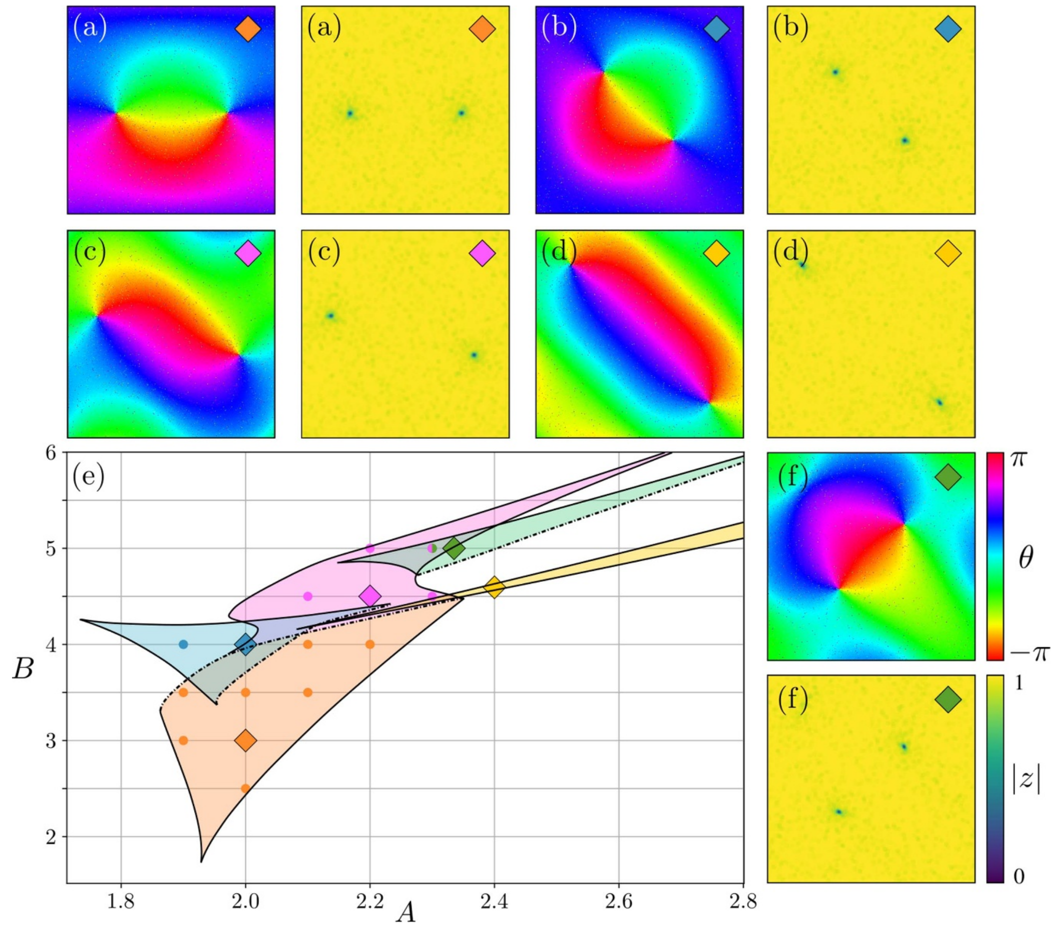

Figure 10. The (A, B) parameter plane (panel (e)) showing regions of stable (shaded) static spiral wave chimeras from the Ott–Antonsen equation (6) with $\alpha = 0$ together with solution snapshots corresponding to the color-coded diamond symbols, showing the phase θ and modulus $|z|$ of the complex order parameter z. Filled circles indicate the parameters of stable spiral wave chimeras found in direct numerical simulations of equation (3) with $N = 512$. The solid and dash-dotted stability boundaries correspond to fold and pitchfork bifurcations, respectively. (a) Z_2-symmetric chimera, (b) $\tilde{Z}_2$-symmetric chimera, (c) Z_2-asymmetric chimera, (d) $\tilde{Z}_2$-symmetric chimera and (f) $\tilde{Z}_2$-asymmetric (super-asymmetric) chimera. Profiles (b) and (d) correspond to different stability intervals on the same solution branch (see blue branch in figure 8).

$\tilde{Z}_2$-symmetric. Stability calculation points to a narrow region of bistability between the Z_2- and $\tilde{Z}_2$-symmetric states. Stable asymmetric states are present at larger values of B (purple branch, state (ii)).

(v) At $B = 5$, the Z_2-symmetric spiral chimeras are unstable, but $\tilde{Z}_2$-symmetric spiral chimeras can still be stable in a certain parameter range (blue branch, state (i)). A branch of $\tilde{Z}_2$-asymmetric spiral chimeras (light green branch, state (iii)) bifurcates from the $\tilde{Z}_2$-symmetric spiral chimeras and some of these may also be stable. We call the resulting states super-asymmetric to distinguish them from the other states previously called asymmetric. The reason for this terminology is the following. Every Z_2- or $\tilde{Z}_2$-symmetric state as well as every asymmetric state is represented by expression (12) with an appropriate function $w(x, y)$ in the nine-dimensional manifold determined by expressions (22) and (25) from section 3.1. In contrast, for super-asymmetric states such a representation is not possible. In this case, the corresponding function $w(x, y)$ is still given by (22) but with fully complex coefficients, except for those in the pinning conditions (24).

For every static two-core spiral chimera shown in figure 8 we performed continuation of its stability boundaries. As a result, we identified five partly overlapping stability regions in the (A, B) plane shown in figure 10. Each of these regions is bounded by two fold bifurcation curves (solid lines) and one pitchfork bifurcation curve (dash-dotted line).

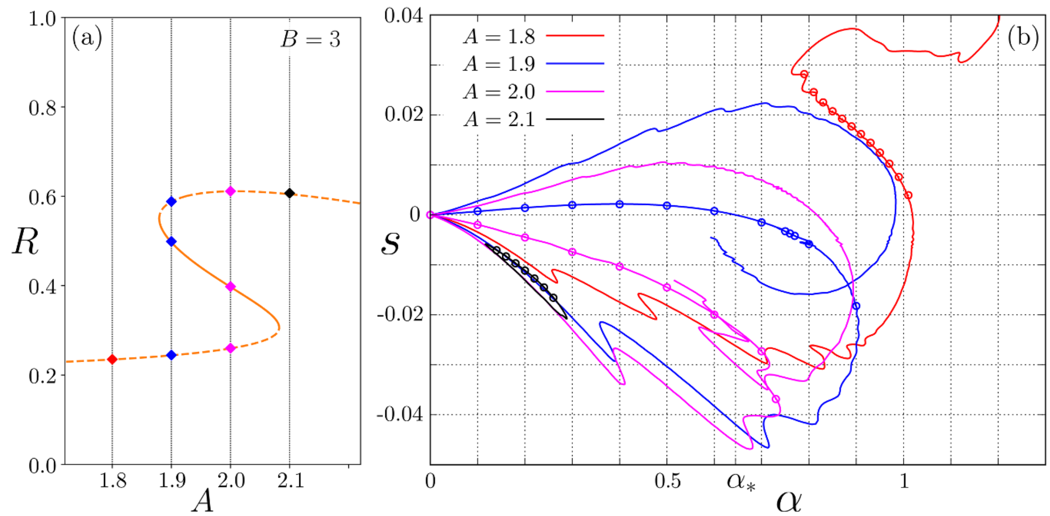

Figure 11. (a) The global order parameter R of Z_2-symmetric two-core spiral wave chimeras versus the parameter A of the trigonometric coupling function (10) when $B = 3$ and $\alpha = 0$. (b) The speed s of symmetric spiral wave chimeras moving in the y direction versus the phase lag parameter α computed from equation (6) with the trigonometric coupling function (10) with four different values A (color-coded) and $B = 3$. Open circles indicate the speed of stable spiral wave chimeras found in direct numerical simulations of equation (3) with the same coupling function (10) and $N = 512$.

2.5. Moving spiral wave chimeras

Moving spiral wave chimeras are observed in the non-variational case, i.e. for $\alpha \neq 0$. To continue such states in parameter space we used a numerical method based on the self-consistency equation from section 3.2 together with a non-iterative algorithm for calculating periodic orbits in the Ott–Antonsen manifold [56]. To describe typical bifurcation diagrams as the phase lag α changes, we consider the case $B = 3$. Figure 11(a) shows a diagram analogous to figure 8 that indicates that for $A = 2$ and $\alpha = 0$ there are three coexisting motionless Z_2-symmetric two-core spiral wave chimeras (pink diamonds). Only one, the one with an intermediate value of R, is stable. When α increases each of these spiral patterns persists as a moving spiral wave chimera and its stability remains unchanged for small α (pink curves in figure 11(b)). For larger α the dependence of the speed s on α becomes nonlinear (figure 11(b)) and the bottom and intermediate branches annihilate in a fold point at $\alpha \approx 0.74$ while the upper, $s > 0$ branch continues beyond this point.

If we take $A = 2.1$ the upper, $s > 0$ branch continues to exist (not shown) while a loop composed of the two $s < 0$ branches detaches from $\alpha = 0$ (black curves) but stable solutions continue to exist on the upper portion of the resulting isola. This loop shrinks rapidly with increasing A and disappears by $A = 2.2$, thereby eliminating stable two-core spiral chimera states.

A qualitatively different scenario occurs if we decrease the parameter A. For $A = 1.9$ the middle branch now corresponds to $s > 0$ forming part of a looped branch that grows in size and intersects the horizontal axis at some $\alpha_* \approx 0.645$ (blue curves). Thus the spiral wave chimeras travel in opposite directions for $\alpha < \alpha_*$ and $\alpha > \alpha_*$.

In contrast, for $A = 1.8$ and $\alpha = 0$ the remaining two-core spiral wave chimera (figure 11(a)) results in moving states with $s < 0$ (red curve in figure 11(b)) with the two upper branches detached from $\alpha = 0$ forming an S-shaped curve whose intermediate section corresponds to numerically stable two-core spiral wave chimeras. Snapshots of the solutions along this branch (figure 12) show that with increasing $|s|$ the incoherent regions around the phase defects develop internal structure in the form of crescent-shaped filaments. Along the bottom part of the branch, the development of each new filament corresponds to an S-shaped fold in the solution branch in the (α, s) plane reminiscent of slanted snaking of spatially localized states [48–52]. However, in other cases, especially when the number of filaments is large (more than 10 or so) or s is close to zero, the speed s evolves monotonically with α in a manner reminiscent of *smooth* snaking [51]. Both behaviors are characteristic of nonlocal systems.

Note that the shape of the solution branch for $A = 1.8$ resembles qualitatively the behavior of the solution curve in figure 3 calculated for the top-hat coupling function. Moreover, the changes in the profiles $a(x, y)$ along the curve are also reminiscent of those shown in figure 3.

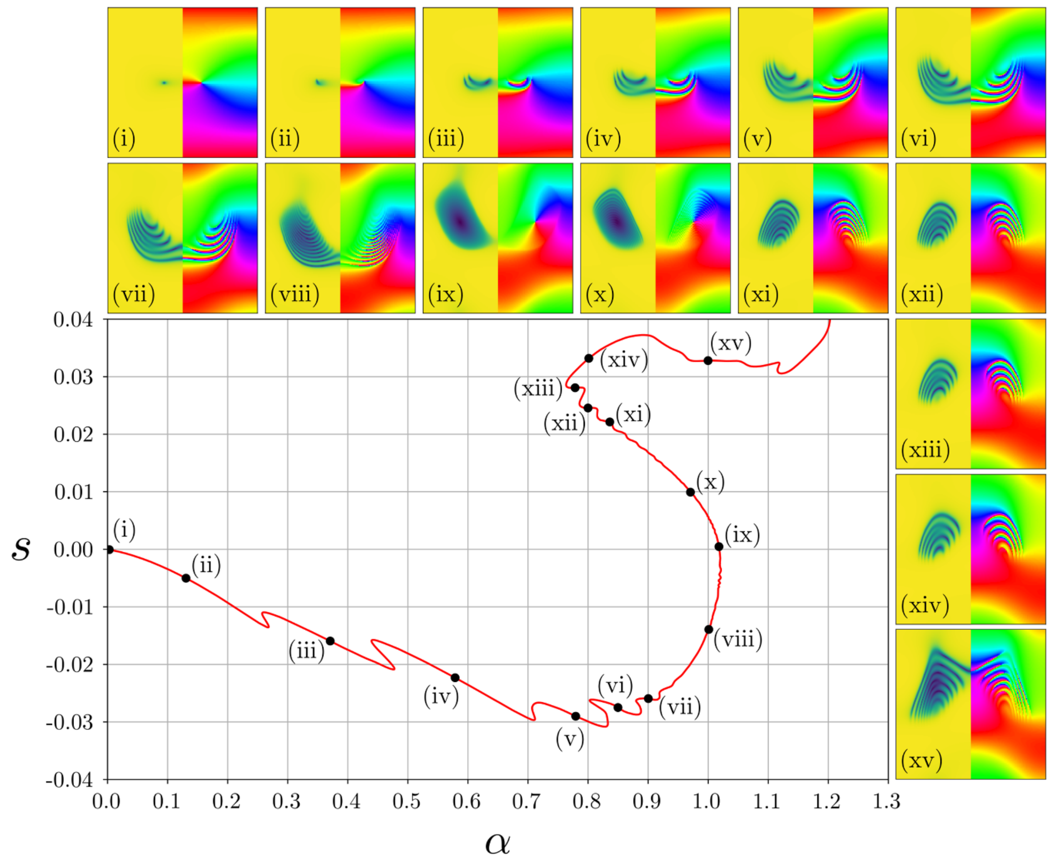

Figure 12. The solution branch for $A = 1.8$, $B = 3$ shown in red in figure 11(b) together with the corresponding fingerprint patterns at the locations labeled in the main panel.

3. Methods

3.1. Static patterns for equation (6) with $\alpha = 0$

In the case $\alpha = 0$, equation (6) is variational and its long-term dynamics therefore correspond to static patterns or equilibria of the form

$$z(x,y,t) = a(x,y). \tag{15}$$

All two-core spiral wave solutions of equation (6) shown in figure 8 have this form. Below we describe the mathematical methods used to carry out continuation and stability analysis of these states. For this, we adapt the techniques from [36, 45].

3.1.1. Self-consistency equation

Inserting ansatz (15) into equation (6) we obtain

$$0 = -\gamma a + \frac{1}{2}\mathcal{G}a - \frac{1}{2}a^2\mathcal{G}\overline{a}$$

or equivalently

$$\overline{w}(x,y)\,a^2 + 2\gamma a - w(x,y) = 0, \tag{16}$$

where

$$w(x,y) = (\mathcal{G}a)(x,y). \tag{17}$$

Solving equation (16) for a and choosing the square root branch that ensures the inequality $|a| \leqslant 1$, we obtain

$$\begin{aligned} a(x,y) &= \frac{-\gamma + \sqrt{\gamma^2 + |w(x,y)|^2}}{\overline{w}(x,y)} \\ &= \frac{w(x,y)}{\gamma + \sqrt{\gamma^2 + |w(x,y)|^2}}. \end{aligned} \tag{18}$$

Expressions (17) and (18) agrees with one another iff the function $w(x,y)$ satisfies the self-consistency equation

$$w(x,y) = \int_{-\pi}^{\pi}\int_{-\pi}^{\pi} G(x-x', y-y') H_\gamma(w(x',y'))\, \mathrm{d}x'\, \mathrm{d}y', \tag{19}$$

where

$$H_\gamma(w) = \frac{w}{\gamma + \sqrt{\gamma^2 + |w|^2}}.$$

3.1.2. Reduced self-consistency equation

Let us consider equation (19) in the case of the trigonometric coupling function (10). First, we define an inner product on the space $C([-\pi,\pi];\mathbb{C})$,

$$\langle u, v\rangle = \frac{1}{(2\pi)^2}\int_{-\pi}^{\pi}\int_{-\pi}^{\pi} u(x,y)\overline{v}(x,y)\,\mathrm{d}x\,\mathrm{d}y.$$

Then, it is easy to see that for the trigonometric coupling function (10) we have

$$(\mathcal{G}u)(x,y) = \sum_{k=1}^{9} \xi_k \langle u, \psi_k\rangle \psi_k(x,y),$$

where

$$\begin{aligned} &\psi_1(x,y) = 1, \quad \psi_2(x,y) = \cos x, \quad \psi_3(x,y) = \cos y, \\ &\psi_4(x,y) = \sin y, \quad \psi_5(x,y) = \cos x \cos y, \quad \psi_6(x,y) = \cos x \sin y, \\ &\psi_7(x,y) = \sin x, \quad \psi_8(x,y) = \sin x \cos y, \quad \psi_9(x,y) = \sin x \sin y, \end{aligned}$$

and

$$\xi_k = \begin{cases} 1 & \text{for} \quad k = 1, \\ A & \text{for} \quad k = 2,3,4,7, \\ B & \text{for} \quad k = 5,6,8,9. \end{cases} \tag{20}$$

Note that the functions $\psi_k(x,y)$ are mutually orthogonal with respect to the inner product $\langle\cdot,\cdot\rangle$. Moreover,

$$\langle \psi_n, \psi_n\rangle = \begin{cases} 1 & \text{for} \quad n = 1, \\ 1/2 & \text{for} \quad n = 2,3,4,7, \\ 1/4 & \text{for} \quad n = 5,6,8,9. \end{cases} \tag{21}$$

Owing to the finite-rank nature of the resulting integral operator $\mathcal{G}$ every solution of the self-consistency equation (19) can be written in the form

$$w(x,y) = \sum_{k=1}^{9} \hat{w}_k \psi_k(x,y) \tag{22}$$

with complex coefficients $\hat{w}_k$. Inserting (22) into equation (19) and equating similar terms on the left and right sides, we obtain the finite-dimensional system

$$\hat{w}_j = \xi_j \left\langle H_\gamma\left(\sum_{k=1}^{9} \hat{w}_k \psi_k\right), \psi_j \right\rangle, \quad j = 1, \ldots, 9. \tag{23}$$

The system (23) inherits the three continuous symmetries of equation (19). Therefore a unique solution requires that we impose three *pinning conditions*, for example

$$\hat{w}_1 = |\hat{w}_1|, \qquad \hat{w}_4 = i|\hat{w}_4|, \qquad \hat{w}_7 = i|\hat{w}_7|. \tag{24}$$

Note that owing to the first pinning condition the value of $\hat{w}_1$ always coincides with the global order parameter R defined in equation (13).

It turns out that the vast majority of stable static solutions of equation (6) with the coupling function (10) and in particular almost all the patterns shown in figure 8 are represented by solutions of the system (23) and (24) on the invariant manifold determined by the identities

$$\begin{cases} \mathrm{Im}\,\hat{w}_k = 0 & \text{for} \quad k = 1,2,3,5,9, \\ \mathrm{Re}\,\hat{w}_k = 0 & \text{for} \quad k = 4,6,7,8. \end{cases} \tag{25}$$

The invariance of this manifold follows from the fact that the basis functions ψ_k with $k = 1,2,3,5,9$ have the reflection symmetry

$$\psi_k(-x,-y) = \psi_k(x,y),$$

while the remaining four functions with $k = 4,6,7,8$ satisfy the antisymmetric relation

$$\psi_k(-x,-y) = -\psi_k(x,y).$$

The restriction of the system (23), (24) to the manifold (25) almost halves the dimensionality of the system and allows a significant speed-up of its solution.

We may further reduce the dimensionality of the system (23), (24) by looking for Z_2-symmetric solutions of equation (19). Such solutions satisfy the relation $w(-x,y) = w(x,y)$, so we must assume $\hat{w}_7 = \hat{w}_8 = \hat{w}_9 = 0$. The resulting six equations require only the first two pinning conditions in (24) in order to obtain a unique solution. A similar approach applies to $\tilde{Z}_2$-symmetric solutions as well.

3.1.3. Initial conditions for system (23)

To apply a Newton solver to system (23) we need to have a good initial guess. In addition, it is desirable that this guess satisfies the pinning conditions (24). We perform this task as follows.

We run the numerical simulations for the oscillator system (3) with the coupling function (10) until it approaches a stationary state of interest. Using the last snapshot of the phases θ_{jk}, we calculate a discrete analog of formula (17),

$$W_{jk} = \left(\frac{2\pi}{N}\right)^2 \sum_{m,n=1}^{N} G\left(\frac{2\pi\,(j-m)}{N}, \frac{2\pi\,(k-n)}{N}\right) \mathrm{e}^{\mathrm{i}\theta_{mn}},$$

where the complex exponent $\mathrm{e}^{\mathrm{i}\theta_{mn}}$ appears instead of $z(-\pi + 2\pi\, m/N, -\pi + 2\pi\, n/N)$. Next, using the discrete Fourier transform, we calculate the necessary Fourier coefficients $\hat{w}_k$.

These coefficients do not, in general, satisfy the pinning conditions (24). To impose the pinning condition on $\hat{w}_1$, we apply a transformation

$$\hat{w}_k \mapsto \hat{w}_k \frac{\overline{\hat{w}_1}}{|\hat{w}_1|}, \qquad k = 1,2,\ldots,9.$$

Next, we perform a transformation that ensures the pinning condition for $\hat{w}_4$

$$\begin{aligned} \hat{w}_3 &\mapsto \hat{w}_3 \cos y_0 - \hat{w}_4 \sin y_0, \\ \hat{w}_4 &\mapsto \hat{w}_3 \sin y_0 + \hat{w}_4 \cos y_0, \\ \hat{w}_5 &\mapsto \hat{w}_5 \cos y_0 - \hat{w}_6 \sin y_0, \\ \hat{w}_6 &\mapsto \hat{w}_5 \sin y_0 + \hat{w}_6 \cos y_0, \\ \hat{w}_8 &\mapsto \hat{w}_8 \cos y_0 - \hat{w}_9 \sin y_0, \\ \hat{w}_9 &\mapsto \hat{w}_8 \sin y_0 + \hat{w}_9 \cos y_0, \end{aligned}$$

where

$$\mathrm{e}^{\mathrm{i}y_0} = \pm \frac{\mathrm{Re}\,(\hat{w}_3) - \mathrm{i}\mathrm{Re}\,(\hat{w}_4)}{\sqrt{[\mathrm{Re}\,(\hat{w}_3)]^2 + [\mathrm{Re}\,(\hat{w}_4)]^2}}$$

and from the two signs in the last formula, the one that makes the imaginary part of $\hat{w}_4$ positive is chosen. Finally, we perform a third transformation,

$$
\begin{aligned}
\hat{w}_2 &\mapsto \hat{w}_2 \cos x_0 - \hat{w}_7 \sin x_0, \\
\hat{w}_7 &\mapsto \hat{w}_2 \sin x_0 + \hat{w}_7 \cos x_0, \\
\hat{w}_5 &\mapsto \hat{w}_5 \cos x_0 - \hat{w}_8 \sin x_0, \\
\hat{w}_8 &\mapsto \hat{w}_5 \sin x_0 + \hat{w}_8 \cos x_0, \\
\hat{w}_6 &\mapsto \hat{w}_6 \cos x_0 - \hat{w}_9 \sin x_0, \\
\hat{w}_9 &\mapsto \hat{w}_6 \sin x_0 + \hat{w}_9 \cos x_0,
\end{aligned}
$$

where

$$
e^{ix_0} = \pm \frac{\mathrm{Re}\,(\hat{w}_2) - i\mathrm{Re}\,(\hat{w}_7)}{\sqrt{[\mathrm{Re}\,(\hat{w}_2)]^2 + [\mathrm{Re}\,(\hat{w}_7)]^2}}.
$$

The sign in this expression is chosen such that the imaginary part of $\hat{w}_7$ positive. The resulting coefficients $\hat{w}_k$ satisfy all the pinning conditions (24) *exactly*.

3.1.4. Stability analysis

To analyze the linear stability of the equilibria of equation (6), we proceed as follows. We insert the ansatz

$$
z(x,y,t) = a(x,y) + v(x,y,t)
$$

into the equation and linearize it with respect to the infinitesimal perturbation v. Thus

$$
\frac{dv}{dt} = -\eta_0(x,y)\,v + \frac{1}{2}\mathcal{G}v - \frac{1}{2}a^2(x,y)\,\mathcal{G}\bar{v}, \tag{26}
$$

where

$$
\eta_0(x,y) = \gamma + a(x,y)\,\mathcal{G}\bar{a},
$$

the subscript 0 on $\eta_0(x,y)$ indicating that we are considering a static pattern. Owing to (17) and (18), we have

$$
\eta_0(x,y) = \sqrt{\gamma^2 + |w(x,y)|^2}, \tag{27}
$$

implying that $\eta_0(x,y)$ is real and satisfies $|\eta_0(x,y)| \geqslant \gamma$.

The structure of equation (26) implies that the spectrum consists of two parts: the essential spectrum

$$
\sigma_{\mathrm{ess}} = \left\{ -\eta_0(x,y) \,:\, (x,y) \in [-\pi,\pi]^2 \right\} \subset \mathbb{R}
$$

and the point spectrum σ_{pt} consisting of isolated eigenvalues of finite multiplicity. To find the eigenvalues $\lambda \in \sigma_{\mathrm{pt}}$ we employ the ansatz

$$
v(x,y,t) = v_+(x,y)\,e^{\lambda t} + \bar{v}_-(x,y)\,e^{\bar{\lambda} t},
$$

which yields a solution to equation (26) provided the eigenvalue λ and the components $(v_+, v_-)^{\mathrm{T}}$ of the eigenmode satisfy

$$
\lambda \begin{pmatrix} v_+ \\ v_- \end{pmatrix} = \begin{pmatrix} -\eta_0 v_+ + \frac{1}{2}\mathcal{G}v_+ - \frac{1}{2}a^2\mathcal{G}v_- \\ -\eta_0 v_- + \frac{1}{2}\mathcal{G}v_- - \frac{1}{2}\bar{a}^2\mathcal{G}v_+ \end{pmatrix},
$$

or equivalently

$$
\begin{pmatrix} v_+ \\ v_- \end{pmatrix} = \frac{1}{2}(\lambda + \eta_0)^{-1} \begin{pmatrix} \mathcal{G}v_+ - a^2\mathcal{G}v_- \\ \mathcal{G}v_- - \bar{a}^2\mathcal{G}v_+ \end{pmatrix}. \tag{28}
$$

Applying the integral operator $\mathcal{G}$ to both sides of equation (28), we obtain the nonlocal eigenvalue problem

$$
\begin{pmatrix} V_+ \\ V_- \end{pmatrix} = \frac{1}{2} \begin{pmatrix} \mathcal{G}\left[(\lambda + \eta_0)^{-1}(V_+ - a^2 V_-)\right] \\ \mathcal{G}\left[(\lambda + \eta_0)^{-1}(V_- - \bar{a}^2 V_+)\right] \end{pmatrix} \tag{29}
$$

for the components

$$
V_+(x,y) = (\mathcal{G}v_+)(x,y), \quad V_-(x,y) = (\mathcal{G}v_-)(x,y)
$$

of the eigenmode of the local mean field $V \equiv \mathcal{G}v$.

Recall that for the coupling function (10), the integral operator $\mathcal{G}$ has a finite-dimensional range spanned by the functions $\psi_k(x,y)$, $k = 1,\ldots,9$. Therefore, every solution of equation (29) can be written in the form

$$V \equiv \begin{pmatrix} V_+ \\ V_- \end{pmatrix} = \sum_{k=1}^{9} \hat{V}_k \psi_k(x,y)$$

with some $\hat{V}_k \in \mathbb{C}^2$. Inserting this ansatz into equation (29) yields a system of nonlinear equations for the nine pairs of complex coefficients $\hat{V}_k$. Collecting these coefficients into a single vector $\hat{V} \in \mathbb{C}^{18}$, we can rewrite these equations as an equivalent matrix equation,

$$\hat{V} = \frac{1}{2} B(\lambda)\, \hat{V},$$

where we solve for the eigenvalue λ and the corresponding vector $\hat{V} \in \mathbb{C}^{18}$. The matrix $B(\lambda)$ has the structure

$$B(\lambda) = \begin{pmatrix} B_{11}(\lambda) & B_{12}(\lambda) & \cdots & B_{19}(\lambda) \\ B_{21}(\lambda) & B_{22}(\lambda) & \cdots & B_{29}(\lambda) \\ \vdots & \vdots & \ddots & \vdots \\ B_{91}(\lambda) & B_{92}(\lambda) & \cdots & B_{99}(\lambda) \end{pmatrix}$$

and consists of 2×2 blocks:

$$B_{mn}(\lambda) = \xi_m \begin{pmatrix} \left\langle \frac{1}{\lambda+\eta_0}\psi_m, \psi_n \right\rangle & -\left\langle \frac{H_\gamma(w)^2}{\lambda+\eta_0}\psi_m, \psi_n \right\rangle \\ -\left\langle \frac{\overline{H_\gamma(w)}^2}{\lambda+\eta_0}\psi_m, \psi_n \right\rangle & \left\langle \frac{1}{\lambda+\eta_0}\psi_m, \psi_n \right\rangle \end{pmatrix},$$

where the ξ_m are defined by (20) and we have replaced $a(x,y)$ by expression (18). Thus the matrix $B(\lambda)$ is completely determined by the solution $w(x,y)$ of the self-consistency equation (19).

The eigenvalues λ can be found as solutions of the characteristic equation

$$\det\left[I_{18} - \frac{1}{2}B(\lambda)\right] = 0, \tag{30}$$

where I_n denotes the $n\times n$ identity matrix. If all solutions $\lambda \neq 0$ of equation (30) lie in the left half-plane, $\mathrm{Re}\ \lambda < 0$, then the corresponding equilibrium $a(x,y)$ is linearly stable. In contrast, if equation (30) has at least one solution $\lambda = \lambda_*$ such that $\mathrm{Re}\ \lambda_* > 0$, then the equilibrium $a(x,y)$ is unstable.

3.1.5. Stability of the completely incoherent state

The completely incoherent state corresponds to the zero solution $w(x,y) = 0$ of equation (19) and hence to the zero solution $z(x,y,t) = 0$ of equation (6). It is present for all values $A, B \in \mathbb{R}$. In this case, $\eta_0(x,y) = \gamma$ from equation (27), and therefore

$$B_{mn}(\lambda) = c_m \langle \psi_m, \psi_n \rangle (\lambda+\gamma)^{-1} I_2.$$

Owing to the mutual orthogonality of the trigonometric functions ψ_m and the relations (21), we easily see that equation (30) factorizes into three equations

$$\det\left[I_2 - \frac{1}{2}(\lambda+\gamma)^{-1} I_2\right] = 0,$$

$$\det\left[I_2 - \frac{A}{4}(\lambda+\gamma)^{-1} I_2\right] = 0,$$

and

$$\det\left[I_2 - \frac{B}{8}(\lambda+\gamma)^{-1} I_2\right] = 0,$$

which determine three eigenvalues

$$\lambda = -\gamma + \frac{1}{2}, \quad \lambda = -\gamma + \frac{A}{4}, \quad \lambda = -\gamma + \frac{B}{8},$$

each of double multiplicity. Consequently, the completely incoherent state $z(x,y,t)=0$ is linearly stable if $\gamma \geqslant \max(1/2, A/4, B/8)$ and is unstable otherwise.

3.1.6. Stability of the partially coherent uniform state

This state corresponds to nonzero constant solutions of equations (19) and (6) of the form

$$w(x,y) = p.$$

Inserting this ansatz into equation (19) we obtain

$$p = \frac{p}{\gamma + \sqrt{\gamma^2 + p^2}}$$

yielding

$$p = \sqrt{1-2\gamma} \quad \text{for} \quad \gamma < 1/2,$$

and $\eta_0(x,y) = \sqrt{\gamma^2+p^2} = 1-\gamma$; see equation (27). Moreover,

$$B_{mn}(\lambda) = \frac{c_m\langle\psi_m,\psi_n\rangle}{\lambda+\eta_0}\begin{pmatrix} 1 & -p^2 \\ -p^2 & 1 \end{pmatrix} = \frac{c_m\langle\psi_m,\psi_n\rangle}{\lambda+1-\gamma}\begin{pmatrix} 1 & 2\gamma-1 \\ 2\gamma-1 & 1 \end{pmatrix}.$$

Due to the mutual orthogonality of the trigonometric functions ψ_m and the relations (21), we easily see that equation (30) factorizes into nine equations ($m = 1,\ldots,9$),

$$\det\left[I_2 - \frac{c_m\langle\psi_m,\psi_m\rangle}{2(\lambda+1-\gamma)}\begin{pmatrix} 1 & 2\gamma-1 \\ 2\gamma-1 & 1 \end{pmatrix}\right] = 0,$$

and that each factor determines two eigenvalues,

$$\lambda = -1+\gamma+\frac{c_m\langle\psi_m,\psi_m\rangle}{2}\left(1\pm(2\gamma-1)\right).$$

For $\gamma < 1/2$ and $c_m \geqslant 0$, the largest eigenvalue is

$$\lambda = -1+\gamma+\frac{c_m\langle\psi_m,\psi_m\rangle}{2}\left(1-(2\gamma-1)\right) = (1-\gamma)\left(c_m\langle\psi_m,\psi_m\rangle - 1\right).$$

Thus the linear stability condition for partially coherent uniform states reads

$$\frac{A}{2} - 1 \leqslant 0 \quad \text{and} \quad \frac{B}{4} - 1 \leqslant 0.$$

If either of the above two inequalities is violated, then the corresponding partially coherent uniform state is unstable.

3.2. Moving spiral wave chimeras for equation (6) with $\alpha \neq 0$

In this section we describe the mathematical tools used to calculate moving spiral wave solutions of equation (6) and to determine their stability. We focus on Z_2-symmetric solutions of the form

$$z(x,y,t) = a(x,y-st)\,\mathrm{e}^{\mathrm{i}\Omega t} \tag{31}$$

with speed s, collective frequency Ω and a reflection-symmetric profile $a(x,y) = a(-x,y)$.

3.2.1. Self-consistency equation

Inserting ansatz (31) into equation (6), reordering the terms and dividing the resulting equation by $s \neq 0$, we obtain

$$\frac{\partial a}{\partial y} = \frac{\gamma+\mathrm{i}\Omega}{s}a - \frac{1}{2s}\mathrm{e}^{-\mathrm{i}\alpha}\mathcal{G}a + \frac{1}{2s}\mathrm{e}^{\mathrm{i}\alpha}a^2\mathcal{G}\overline{a}. \tag{32}$$

We look for 2π-periodic solutions in both x and y satisfying the inequality $|a(x,y)| \leqslant 1$. Therefore, if we happen to know s, Ω and $\mathcal{G}a$, then for each fixed $x \in [-\pi,\pi]$ equation (32) can be read as a periodic boundary value problem for the complex Riccati equation

$$\frac{\mathrm{d}a}{\mathrm{d}y} = w(x,y) + \zeta a - \overline{w}(x,y)\,a^2, \tag{33}$$

where $a(x,\cdot)$ is an unknown function, x is a parameter,

$$w = -\frac{1}{2s}\mathrm{e}^{-\mathrm{i}\alpha}\mathcal{G}a$$

and

$$\zeta = \frac{\gamma + \mathrm{i}\Omega}{s}.$$

It is known [56] that, for every $\zeta \notin i\mathbb{R}$ and every $w(x,\cdot) \in C_{\mathrm{per}}([-\pi,\pi];\mathbb{C})$, equation (33) has a unique 2π-periodic solution $u(y)$ depending on x as a parameter such that $|u(y)| < 1$. The corresponding solution operator is denoted by $\mathcal{U}(w,\zeta)$. Then equation (32) with the additional condition $|a(x,y)| \leqslant 1$ can be recast into the equivalent form

$$-2s\mathrm{e}^{\mathrm{i}\alpha}w(x,y) = \mathcal{G}\mathcal{U}\left(w(x,y), \frac{\gamma+\mathrm{i}\Omega}{s}\right). \tag{34}$$

We interpret equation (34) as a self-consistency equation analogous to equation (19). It is to be solved for the function $w(x,y)$ and the two scalars s and Ω. This can be done if we equip equation (34) with two pinning conditions,

$$\mathrm{Im}\left(\int_{-\pi}^{\pi}\int_{-\pi}^{\pi} w(x,y)\,\mathrm{d}x\,\mathrm{d}y\right) = 0, \tag{35}$$

$$\mathrm{Im}\left(\int_{-\pi}^{\pi}\int_{-\pi}^{\pi} w(x,y)\sin y\,\mathrm{d}x\,\mathrm{d}y\right) = 0, \tag{36}$$

and recall that $w(x,y)$ must share the reflection symmetry of the function $a(x,y)$.

In the case of the trigonometric coupling function (10) we can assume

$$w(x,y) = \sum_{k=1}^{6}\hat{w}_k\psi_k(x,y).$$

The basis function ψ_7, ψ_8 and ψ_9 do not appear in the sum because they do not satisfy the symmetry relation $\psi(-x,y) = \psi(x,y)$. Equation (34) is thus equivalent to the six-dimensional complex system

$$-2s\mathrm{e}^{\mathrm{i}\alpha}\hat{w}_j = \xi_j\left\langle \mathcal{U}\left(\sum_{k=1}^{6}\hat{w}_k\psi_k, \frac{\gamma+\mathrm{i}\Omega}{s}\right), \psi_j\right\rangle$$

for six complex unknowns $\hat{w}_j$ and two real unknowns Ω and s. The balance between the number of equations and the number of unknowns is ensured by the two pinning conditions (35) and (36), which are equivalent to the two scalar constraints

$$\mathrm{Im}\ \hat{w}_1 = 0 \qquad \text{and} \qquad \mathrm{Im}\ \hat{w}_4 = 0.$$

3.2.2. Solution operator $\mathcal{U}(w,\zeta)$

There is no explicit expression for the operator $\mathcal{U}(w,\zeta)$. But, as shown in [56], its value can be determined by solving only four initial value problems for equation (33). This possibility follows from the fact that the Poincaré map of equation (33) coincides with the classical Möbius transformation.

3.2.3. Stability analysis

The linear stability analysis of a uniformly drifting state (31) can be performed by analogy with the static case, see section 3.1. For this, we insert the ansatz

$$z(x,y,t) = (a(x,y-st) + v(x,y-st,t))\,\mathrm{e}^{\mathrm{i}\Omega t}$$

into equation (6) and linearize the resulting equation with respect to the infinitesimal perturbation v. We thereby obtain a linear partial integro-differential equation for v,

$$-s\frac{\partial v}{\partial \xi} + \frac{\partial v}{\partial t} = -\eta(x,\xi)\,v + \frac{1}{2}\mathrm{e}^{-\mathrm{i}\alpha}\mathcal{G}v - \frac{1}{2}\mathrm{e}^{\mathrm{i}\alpha}a^2(x,\xi)\,\mathcal{G}\bar{v}, \tag{37}$$

where $\xi \equiv y - st$ is the comoving variable and

$$\eta(x,\xi) \equiv \gamma + \mathrm{i}\Omega + \mathrm{e}^{\mathrm{i}\alpha} a(x,\xi)\mathcal{G}\overline{a}.$$

The spectral problem for the eigenvalues $\lambda \in \mathbb{C}$ and eigenmodes $(v_+, v_-)^{\mathrm{T}}$ can be derived from equation (37) on using the ansatz

$$v(x,\xi,t) = v_+(x,\xi)\,\mathrm{e}^{\lambda t} + \overline{v}_-(x,\xi)\,\mathrm{e}^{\overline{\lambda} t}.$$

After substitution into equation (37), we obtain

$$\lambda \begin{pmatrix} v_+ \\ v_- \end{pmatrix} = \begin{pmatrix} s\dfrac{\partial v_+}{\partial \xi} - \eta v_+ + \dfrac{1}{2}\mathrm{e}^{-\mathrm{i}\alpha}\mathcal{G}v_+ - \dfrac{1}{2}\mathrm{e}^{\mathrm{i}\alpha}a^2\mathcal{G}v_- \\ s\dfrac{\partial v_-}{\partial \xi} - \overline{\eta}v_- + \dfrac{1}{2}\mathrm{e}^{\mathrm{i}\alpha}\mathcal{G}v_- - \dfrac{1}{2}\mathrm{e}^{-\mathrm{i}\alpha}\overline{a}^2\mathcal{G}v_+ \end{pmatrix}, \tag{38}$$

where it is assumed that v_+ and v_- are 2π-periodic with respect to x and ξ.

Rigorous analysis of the properties of the spectrum defined by equation (38) can be performed using the approach proposed in [24, section 4]. On the other hand, a naive way to calculate the spectrum numerically is to discretize equation (38) on a uniform grid, approximate the derivatives by finite differences and the integrals by the trapezoid rule. This procedure leads to a matrix eigenvalue problem, which can be solved by standard numerical routines. However, this method has a significant drawback. Since the eigenmodes $v_+(x,\xi)$ and $v_-(x,\xi)$ depend on two variables, each of these functions must be approximated by arrays of minimal size $100 \times 100 = 10^4$. The corresponding eigenvalue problem thus involves a huge, dense matrix of size $10^4 \times 10^4$. As a consequence, the computation of the eigenvalues is extremely time-consuming and we do not perform it in this paper. As an alternative stability analysis scheme, we use the following phenomenological approach. Given a solution (31) of equation (6), we calculate an initial condition of the corresponding system (3) using the formula

$$\theta_{jk}(0) = \arg a\left(-\pi + 2\pi j/N, -\pi + 2\pi k/N\right).$$

We then run simulations of the system (3) for 10^4 time units. If at the end we obtain a state resembling the expected solution (31), we consider it a stable solution of equation (6). Moreover, in this case, we use the last 5000 time units to calculate the mean drift speed of the corresponding pattern, which is plotted on top of the theoretically predicted curves in figure 11(b).

4. Discussion and conclusion

We have shown that both stationary and moving partially synchronized states of two-dimensional arrays of nonlocally coupled nonidentical phase oscillators are well described in the continuum limit by a self-consistency condition originally derived by Ott and Antonsen [44]. In particular, we have shown that we can correctly compute the speed s of these structures as a function of the phase-lag parameter α, with s solving a nonlinear nonlocal eigenvalue problem. We have also shown that the same procedure can be used to determine the stability of these states and confirmed the results using direct numerical simulations of the discrete oscillator system. Our results explain the multiplicity of the different stable states in systems of this type, as well as the various bifurcations responsible for transitions between them.

Although the work was motivated by simulations performed with a top-hat coupling function, much of our progress was based on a two-parameter truncation of the Fourier expansion of this function. The advantage of using coupling functions of this type is apparent from earlier work in [31, 35, 57]. It turns out, for reasons that we do not fully understand, that the values of the parameters A and B typical of different top-hat coupling functions in fact capture the most interesting regimes in the (A,B) plane, regimes where stable stationary and moving chimeras are present (figures 7 and 10).

Our approach enabled us to understand how stable two-core spiral chimeras are generated for different values of the parameters (A,B) as well as of α, albeit for a single value of the width of the Lorentzian frequency distribution, $\gamma = 0.01$. We have seen that when $\alpha = 0$ two-core symmetric spiral chimeras, either Z_2-symmetric or $\tilde{Z}_2$-symmetric, are found on tertiary branches, following three successive symmetry-breaking bifurcations, the first of which generates a π-periodic state $|a(x,y)|$ from the partially coherent state, while the second creates a 2π-periodic state $|a(x,y)|$, after which the incoherent cores localize in the transverse direction. For stability these two-core states require nonzero values of both coupling coefficients A and B; the optimal conditions are such that the functions 1, $A\cos x$, $A\cos y$ and $B\cos x\cos y$ have comparable L^2-norms, i.e. for $A \approx 2$ and $B \approx 4$. Four-core states are created by a similar process. These states are all static.

When $\alpha > 0$, these states begin to drift, resulting in a quasiperiodic state. Such two-frequency states are associated with the appearance of curved filaments in the incoherent cores. The number of such filaments increases with α, and the addition of each new filament is associated with a fold in the bifurcation diagram, resulting in states with a great many filaments in the core such as state (viii) of figure 12. The filaments of moving symmetric chimera states are curved in the direction opposite to the direction of motion. Moreover, they typically appear in the front part of the moving structure, in contrast to the one-dimensional traveling chimera states, where similar spatial oscillations emerge in the wake of the moving structure. However, the speed s of such states is in general a highly nonmonotonic function of α and may vanish for nonzero α. It is remarkable that results of this complexity can be accessed semi-analytically and that their stability properties can likewise be established by similar techniques. Direct numerical simulations of the discrete system have confirmed these results with exquisite accuracy (figure 11(b)).

In this paper, we focused on the properties of symmetric moving spiral wave chimeras with a trigonometric coupling function. We expect that with some modifications, the computational scheme described in section 3.2 can also be applied to study asymmetric spiral wave chimeras. Our results for the variational case $\alpha = 0$ show how such states are related to each other. Moreover, our methods readily extend to three-dimensional arrays of phase oscillators with trigonometric coupling functions [36] as well as to spatially-coupled arrays of phase oscillators with finite response times [58].

Although most of our results are for the trigonometric coupling function, the results qualitatively reproduce many of the direct numerical simulation results obtained for the top-hat coupling function. The trigonometric coupling approximation to this and related coupling functions has the advantage that both stable and unstable spiral chimera states can be readily computed. The latter are of inestimable value for establishing the sequence of bifurcations that are required to generate the observed stable states. We expect that the scenarios we have identified for the trigonometric coupling function carry over to other, more realistic coupling functions, where their presence can be established only with the greatest difficulty.

At a practical level, our findings can be used to explain the appearance of traveling spiral wave chimera-like patterns in phase oscillator models related to the dynamics of hydrodynamically coupled cilia carpets [6, 7]. On the other hand, they can potentially suggest new experimental designs for experiments on Belousov-Zhabotinsky chemical oscillators [8, 9]. In a broader context, we may expect that qualitatively similar spiral waves and corresponding bifurcation scenarios can be found in neural field models [59, 60] or models of cardiac tissue electrophysiology [61], where moving spiral waves are common. Potential systems that also support spiral wave chimeras include excitable optical systems, such as semiconductors lasers with [62, 63] or without absorber-saturable medium [64] or with two distinct time delays [65]. We mention, finally, two recent papers describing novel realizations of chimera states, an experimental system of degenerate optical parametric oscillators mimicking neuronal dynamics in biological systems [66] and a two-component Bose–Einstein condensate of ultracold atoms, a Hamiltonian system exhibiting spiral chimera states that may also be realizable in experiments [67].

Data availability statement

No new data were created or analyzed in this study.

Acknowledgment

M B G and M G C thank the ANID-Millenium Science Initiative Program-ICN17_012 and FONDECYT Project No. 1210353 for financial support. The work of E K was supported in part by the National Science Foundation under Grant DMS-1908891. The work of O.E.O. was supported by the Deutsche Forschungsgemeinschaft under Grant No. OM 99/2-2.

ORCID iDs

M G Clerc https://orcid.org/0000-0002-8006-0729
O E Omel'chenko https://orcid.org/0000-0003-0526-1878

References

[1] Huygens C 1986 *Christiaan Huygens' The Pendulum Clock, or, Geometrical Demonstrations Concerning the Motion of Pendula as Applied to Clocks* (Iowa State University Press) Translated by R Blackwell
[2] Bennett M, Schatz M F, Rockwood H and Wiesenfeld K 2002 *Proc. R. Soc.* A **458** 563–79
[3] Sakaguchi H 2006 *Phys. Rev.* E **73** 031907
[4] Luke T B, Barreto E and So P 2013 *Neural Comput.* **25** 3207–34

[5] Omel'chenko O and Laing C R 2022 *Proc. R. Soc.* A **478** 20210817
[6] Uchida N and Golestanian R 2010 *Phys. Rev. Lett.* **104** 178103
[7] Golestanian R, Yeomans J M and Uchida N 2011 *Soft Matter* **7** 3074–82
[8] Nkomo S, Tinsley M R and Showalter K 2013 *Phys. Rev. Lett.* **110** 244102
[9] Totz J F, Rode J, Tinsley M R, Showalter K and Engel H 2017 *Nat. Phys.* **14** 282–5
[10] Guo S, Dai Q, Cheng H, Li H, Xie F and Yang J 2018 *Chaos Solitons Fractals* **114** 394–9
[11] Rode J, Totz J F, Fengler E and Engel H 2019 *Front. Appl. Math. Stat.* **5** 31
[12] Adler R 1946 *Proc. IRE* **34** 351–7
[13] Wang S S and Winful H G 1988 *Appl. Phys. Lett.* **52** 1774–6
[14] Nishikawa T and Motter A E 2015 *New J. Phys.* **17** 015012
[15] Kuramoto Y and Battogtokh D 2002 *Nonlinear Phenom. Complex Syst.* **5** 380–5
[16] Abrams D M and Strogatz S H 2004 *Phys. Rev. Lett.* **93** 174102
[17] Panaggio M J and Abrams D M 2015 *Nonlinearity* **28** R67–R87
[18] Schöll E 2016 *Eur. Phys. J. Spec. Top.* **225** 891–919
[19] Omel'chenko O E 2018 *Nonlinearity* **31** R121–64
[20] Majhi S, Bera B K, Ghosh D and Perc M 2019 *Phys. Life Rev.* **28** 100–21
[21] Haugland S W 2021 *J. Phys. Complex.* **2** 032001
[22] Parastesh F, Jafari S, Azarnoush H, Shahriari Z, Wang Z, Boccaletti S and Perc M 2021 *Phys. Rep.* **898** 1–114
[23] Xie J, Knobloch E and Kao H C 2014 *Phys. Rev.* E **90** 022919
[24] Omel'chenko O E 2020 *Nonlinearity* **33** 611–42
[25] Kuramoto Y and Shima S-I 2003 *Prog. Theor. Phys. Suppl.* **150** 115–25
[26] Shima S-I and Kuramoto Y 2004 *Phys. Rev.* E **69** 036213
[27] Nicolaou Z G, Riecke H and Motter A E 2017 *Phys. Rev. Lett.* **119** 244101
[28] Aranson I S and Kramer L 2002 *Rev. Mod. Phys.* **74** 99–143
[29] Barkley D 1992 *Phys. Rev. Lett.* **68** 2090–3
[30] Chaté H and Manneville P 1996 *Physica* A **224** 348–68
[31] Omel'chenko O E, Wolfrum M and Knobloch E 2018 *SIAM J. Appl. Dyn. Syst.* **17** 97–127
[32] Omel'chenko O E, Wolfrum M, Yanchuk S, Maistrenko Y L and Sudakov O 2012 *Phys. Rev.* E **85** 036210
[33] Silber M and Knobloch E 1991 *Nonlinearity* **4** 1063–107
[34] Maistrenko Y, Sudakov O, Osiv O and Maistrenko V 2015 *New J. Phys.* **17** 073037
[35] Xie J, Knobloch E and Kao H C 2015 *Phys. Rev.* E **92** 042921
[36] Omel'chenko O E and Knobloch E 2019 *New J. Phys.* **21** 093034
[37] Bi H and Fukai T 2022 *Chaos* **32** 083125
[38] Ulonska S, Omelchenko I, Zakharova A and Schöll E 2016 *Chaos* **26** 094825
[39] Hagerstrom A M, Murphy T E, Roy R, Hövel P, Omelchenko I and Schöll E 2012 *Nature Phys.* **8** 658–61
[40] Wickramasinghe M and Kiss I Z 2013 *PLoS One* **8** e80586
[41] Kapitaniak T, Kuzma P, Wojewoda J, Czolczynski K and Maistrenko Y 2014 *Sci. Rep.* **4** 6379
[42] Rosin D P, Rontani D, Haynes N D, Schöll E and Gauthier D J 2014 *Phys. Rev.* E **90** 030902(R)
[43] Omel'chenko O E, Wolfrum M and Maistrenko Y L 2010 *Phys. Rev.* E **81** 065201(R)
[44] Ott E and Antonsen T M 2008 *Chaos* **18** 037113
[45] Omel'chenko O E 2013 *Nonlinearity* **26** 2469–98
[46] Omel'chenko O E 2019 *J. Phys. A: Math. Theor.* **52** 104001
[47] Bataille-Gonzalez M, Clerc M G and Omel'chenko O E 2021 *Phys. Rev.* E **104** L022203
[48] Firth W J, Columbo L and Scroggie A J 2007 *Phys. Rev. Lett.* **99** 104503
[49] Firth W J, Columbo L and Maggipinto T 2007 *Chaos* **17** 037115
[50] Barbay S, Hachair X, Elsass T, Sagnes I and Kuszelewicz R 2008 *Phys. Rev. Lett.* **101** 253902
[51] Thiele U, Archer A J, Robbins M J, Gomez H and Knobloch E 2013 *Phys. Rev.* E **87** 042915
[52] Pradenas B, Araya I, Clerc M G, Falcón C, Gandhi P and Knobloch E 2017 *Phys. Rev. Fluids* **2** 064401
[53] See supplementary material for animations of a moving spiral wave chimera and the solution snapshots along the bifurcation diagram in figure 3
[54] Laing C R 2009 *Physica* D **238** 1569–88
[55] Laing C R 2017 *SIAM J. Appl. Dyn. Syst.* **16** 974–1014
[56] Omel'chenko O E 2023 *Nonlinearity* **36** 845–61
[57] Omel'chenko O E, Wolfrum M and Laing C R 2014 *Chaos* **24** 023102
[58] Lee W S, Restrepo J G, Ott E and Antonsen T M 2011 *Chaos* **21** 023122
[59] Huang X, Troy W C, Yang Q, Ma H, Laing C R, Schiff S J and Wu J Y 2004 *J. Neurosci.* **24** 9897–902
[60] Huang X, Xu W, Liang J, Takagaki K, Gao X and Wu J Y 2010 *Neuron* **68** 978–90
[61] Clayton R H, Bernus O, Cherry E M, Dierckx H, Fenton F H, Mirabella L, Panfilov A V, Sachse F B, Seemann G and Zhang H 2011 *Prog. Biophys. Mol. Biol.* **104** 22–48
[62] Barbay S, Kuszelewicz R and Yacomotti A M 2011 *Opt. Lett.* **36** 4476–8
[63] Selmi F, Braive R, Beaudoin G, Sagnes I, Kuszelewicz R and Barbay S 2014 *Phys. Rev. Lett.* **112** 183902
[64] Marino F and Balle S 2005 *Phys. Rev. Lett.* **94** 094101
[65] Marino F and Giacomelli G 2019 *Phys. Rev. Lett.* **122** 174102
[66] Makinwa T *et al* 2023 *Commun. Phys.* **6** 121
[67] Lau H W H, Davidsen J and Simon C 2023 *Sci. Rep.* **13** 8590

7.1 Perspectives

We have investigated the emergence of moving two-core spiral chimeras for a top-hat and a trigonometric kernel. In particular, for the former kernel, it has been shown that new filaments develop in the incoherent core after a pair of folds in the bifurcation diagram. On the other hand, for the trigonometric kernel, a more in-depth analysis was carried out revealing all equilibria for $\alpha = 0$ and their transitions. In particular, the sequence of three symmetry breaking bifurcations originating from the partially coherent uniform state, explaining the emergence of two-core spirals, has been uncovered. Through an extension of the semi-analytical method, the case of symmetric spirals for $\alpha \neq 0$ was studied, unveiling a similar bifurcation diagram as for the top-hat coupling, confirming the robustness of our results. Therefore, it can be expected that the results shown here may, to a certain extent, persist for different and more realistic coupling kernels.

The totality of the results presented here are based on a detailed analysis of the equilibria and their transitions. Particularly, the different possible configurations of two-core spirals both symmetric and asymmetric were found for a given set of parameters. Nevertheless, the time evolution from a certain initial condition to the final stable configuration remains unknown. A systematic study of the previously described transient dynamics, could shed light on how they spiral chimeras interact between each other and form stable two-core (even four-core and beyond) states. Therefore, this research direction could provide a complementary understanding on the formation of multi-core spiral chimeras, and deserves to be pursued.

Chapter 8

Conclusions

This thesis was devoted to the study and characterization of the dynamics of localized structures in different one- and two-dimensional nonlocal systems. To achieve this, we explored the effect of both asymmetric and symmetric nonlocal couplings in optical resonator and phase oscillator systems, respectively. In both cases, the emergence of traveling LSs was observed, and the main bifurcations leading to their creation, stabilization and disappearence were numerically identified.

In the case of fiber ring resonators, we considered variations of the Lugiato-Lefever equation with different asymmetric coupling terms: the Raman effect, and spectral filtering. The latter was modeled as a gradient expansion of the nonlocal operator. In both cases, these reflection symmetry-breaking terms were found to be responsible for the drift of both localized and periodic states. Additionally, numerical continuation revealed that these terms caused the destruction of the traditional homoclinic snaking bifurcation scenario, which led to the formation of isolas of LSs. Nevertheless, not all of the bifurcations present in the diagram were completely identified, and further work is needed in this direction.

Subsequently, we studied the dynamics of spiral wave chimeras in a two-dimensional network of nonlocally coupled phase oscillators. Unexpectedly, we found that this system exhibits moving spiral chimeras, in spite of the coupling function beeing symmetric and isotropic. The motion of these structures was, therefore, found to be driven by a spontaneous symmetry breaking. Moreover, we identified three different types of moving spirals chimeras according to their motion, and found their respective stability region. The case of symmetric spirals was found to be the most approachable in terms of computational cost, and thus was studied in more detail. More specifically, we obtained the corresponding bifurcation diagram showcasing its main bifurcations. In addition, we considered the effect of a sinusoidal coupling, since it allowed to perform semi-analytic calculations. In this case, we found the sequence of bifurcations which lead to the creation of moving spiral chimeras from a homogeneous state.

Bibliography

[1] Eugen Merzbacher. *Quantum mechanics*. John Wiley & Sons, 1998.

[2] Albert Messiah. *Quantum mechanics*. Courier Corporation, 2014.

[3] Eugene P Gross. "Particle-like solutions in field theory". In: *Annals of Physics* 19.2 (1962), pp. 219–233.

[4] Ilya Prigogine and Gregoire Nicolis. "Self-organization in Non-equilibrium systems". In: 28 (1977).

[5] Len M Pismen. *Patterns and interfaces in dissipative dynamics*. Vol. 706. Springer, 2006.

[6] Paul B Umbanhowar, Francisco Melo, and Harry L Swinney. "Localized excitations in a vertically vibrated granular layer". In: *Nature* 382.6594 (1996), pp. 793–796.

[7] Igor S Aranson and Lev S Tsimring. "Patterns and collective behavior in granular media: Theoretical concepts". In: *Reviews of modern physics* 78.2 (2006), pp. 641–692.

[8] Stefano Minardi et al. "Three-dimensional light bullets in arrays of waveguides". In: *Physical review letters* 105.26 (2010), p. 263901.

[9] N Verschueren et al. "Spatiotemporal Chaotic Localized State in Liquid Crystal Light Valve Experiments¡? format?¿ with Optical Feedback". In: *Physical review letters* 110.10 (2013), p. 104101.

[10] Xu Yi et al. "Imaging soliton dynamics in optical microcavities". In: *Nature communications* 9.1 (2018), p. 3565.

[11] Mustapha Tlidi, Paul Mandel, and René Lefever. "Localized structures and localized patterns in optical bistability". In: *Physical review letters* 73.5 (1994), p. 640.

[12] Pierre Coullet, C Riera, and Charles Tresser. "Stable static localized structures in one dimension". In: *Physical review letters* 84.14 (2000), p. 3069.

[13] E Knobloch. "Spatial Localization in Dissipative Systems". In: *Annual Review of Condensed Matter Physics* 6 (2015), pp. 325–359.

[14] Lendert Gelens et al. "Impact of nonlocal interactions in dissipative systems: Towards minimal-sized localized structures". In: *Physical Review A—Atomic, Molecular, and Optical Physics* 75.6 (2007), p. 063812.

[15] Stephen Coombes. "Waves, bumps, and patterns in neural field theories". In: *Biological cybernetics* 93 (2005), pp. 91–108.

[16] René Lefever and Olivier Lejeune. "On the origin of tiger bush". In: *Bulletin of Mathematical biology* 59 (1997), pp. 263–294.

[17] Cristian Fernandez-Oto et al. "Strong nonlocal coupling stabilizes localized structures: an analysis based on front dynamics". In: *Physical review letters* 110.17 (2013), p. 174101.

[18] Marcel Gabriel Clerc, Saliya Coulibaly, and Mustapha Tlidi. "Time-delayed nonlocal response inducing traveling temporal localized structures". In: *Physical Review Research* 2.1 (2020), p. 013024.

[19] Mehran Kardar. *Statistical physics of fields*. Cambridge University Press, 2007.

[20] H Poincaré. "Sur l'équilibre d'une masse fluide animée d'un mouvement de rotation". In: *Acta Mathematica* 7 (1885), pp. 259–380.

[21] Steven H Strogatz. *Nonlinear dynamics and chaos: with applications to physics, biology, chemistry, and engineering*. CRC press, 2018.

[22] E. Atlee Jackson. *Perspectives of Nonlinear Dynamics*. Cambridge University Press, 1989.

[23] G Bard Ermentrout and John Rinzel. "Beyond a pacemaker's entrainment limit: phase walk-through". In: *American Journal of Physiology-Regulatory, Integrative and Comparative Physiology* 246.1 (1984), R102–R106.

[24] Lev Davidovich Landau and Evgenii Mikhailovich Lifshitz. *Statistical Physics: Volume 5*. Vol. 5. Elsevier, 2013.

[25] Lev D Landau. "On the problem of turbulence". In: *Dokl. Akad. Nauk USSR*. Vol. 44. 1944, p. 311.

[26] John Trevor Stuart. "On the non-linear mechanics of hydrodynamic stability". In: *Journal of Fluid Mechanics* 4.1 (1958), pp. 1–21.

[27] Igor S Aranson and Lorenz Kramer. "The world of the complex Ginzburg-Landau equation". In: *Reviews of modern physics* 74.1 (2002), p. 99.

[28] John Scott Russell. *Report on Waves: Made to the Meetings of the British Association in 1842-43*. 1845.

[29] Diederik Johannes Korteweg and Gustav De Vries. "On the change of form of long waves advancing in a rectangular canal, and on a new type of long stationary waves". In: *The London, Edinburgh, and Dublin Philosophical Magazine and Journal of Science* 39.240 (1895), pp. 422–443.

[30] Norman J Zabusky and Martin D Kruskal. "Interaction of" solitons" in a collisionless plasma and the recurrence of initial states". In: *Physical review letters* 15.6 (1965), p. 240.

[31] Clifford S Gardner et al. "Method for solving the Korteweg-deVries equation". In: *Physical review letters* 19.19 (1967), p. 1095.

[32] Clifford S Gardner et al. "Korteweg-de Vries equation and generalizations. VI. methods for exact solution". In: *Communications on pure and applied mathematics* 27.1 (1974), pp. 97–133.

[33] Aleksei Shabat and Vladimir Zakharov. "Exact theory of two-dimensional self-focusing and one-dimensional self-modulation of waves in nonlinear media". In: *Sov. Phys. JETP* 34.1 (1972), p. 62.

[34] Mark J Ablowitz et al. "Method for solving the sine-Gordon equation". In: *Physical Review Letters* 30.25 (1973), p. 1262.

[35] Mark C Cross and Pierre C Hohenberg. "Pattern formation outside of equilibrium". In: *Reviews of modern physics* 65.3 (1993), p. 851.

[36] Jack Swift and Pierre C Hohenberg. "Hydrodynamic fluctuations at the convective instability". In: *Physical Review A* 15.1 (1977), p. 319.

[37] Y Pomeau and P Manneville. "Stability and fluctuations of a spatially periodic convective flow". In: *Journal de Physique Lettres* 40.23 (1979), pp. 609–612.

[38] Jonathan HP Dawes. "After 1952: The later development of Alan Turing's ideas on the mathematics of pattern formation". In: *Historia mathematica* 43.1 (2016), pp. 49–64.

[39] John Burke and Edgar Knobloch. "Snakes and ladders: localized states in the Swift–Hohenberg equation". In: *Physics Letters A* 360.6 (2007), pp. 681–688.

[40] PD Woods and AR Champneys. "Heteroclinic tangles and homoclinic snaking in the unfolding of a degenerate reversible Hamiltonian–Hopf bifurcation". In: *Physica D: Nonlinear Phenomena* 129.3-4 (1999), pp. 147–170.

[41] WJ Firth, L Columbo, and AJ Scroggie. "Proposed resolution of theory-experiment discrepancy in homoclinic snaking". In: *Physical review letters* 99.10 (2007), p. 104503.

[42] Jonathan HP Dawes. "Localized pattern formation with a large-scale mode: slanted snaking". In: *SIAM Journal on Applied Dynamical Systems* 7.1 (2008), pp. 186–206.

[43] Cédric Beaume et al. "Convectons in a rotating fluid layer". In: *Journal of Fluid Mechanics* 717 (2013), pp. 417–448.

[44] Luigi A Lugiato and René Lefever. "Spatial dissipative structures in passive optical systems". In: *Physical review letters* 58.21 (1987), p. 2209.

[45] David James Kaup and Alan C Newell. "Theory of nonlinear oscillating dipolar excitations in one-dimensional condensates". In: *Physical Review B* 18.10 (1978), p. 5162.

[46] GJ Morales and YC Lee. "Ponderomotive-force effects in a nonuniform plasma". In: *Physical Review Letters* 33.17 (1974), p. 1016.

[47] Ivan S Grudinin et al. "High-contrast Kerr frequency combs". In: *Optica* 4.4 (2017), pp. 434–437.

[48] J. D. Jost et al. "Counting the cycles of light using a self-referenced optical microresonator". In: *Optica* 2.8 (2015), pp. 706–711.

[49] Pablo Marin-Palomo et al. "Microresonator-based solitons for massively parallel coherent optical communications". In: *Nature* 546.7657 (2017), pp. 274–279.

[50] Myoung-Gyun Suh et al. "Searching for exoplanets using a microresonator astrocomb". In: *Nature photonics* 13.1 (2019), pp. 25–30.

[51] Stéphane Coen et al. "Modeling of octave-spanning Kerr frequency combs using a generalized mean-field Lugiato–Lefever model". In: *Optics letters* 38.1 (2012), pp. 37–39.

[52] Stéphane Coen and Miro Erkintalo. “Universal scaling laws of Kerr frequency combs”. In: *Optics letters* 38.11 (2013), pp. 1790–1792.

[53] Yanne K Chembo and Curtis R Menyuk. “Spatiotemporal Lugiato-Lefever formalism for Kerr-comb generation in whispering-gallery-mode resonators”. In: *Physical Review A—Atomic, Molecular, and Optical Physics* 87.5 (2013), p. 053852.

[54] Dmitry Turaev, Mindaugas Radziunas, and Andrei G Vladimirov. “Chaotic soliton walk in periodically modulated media”. In: *Physical Review E—Statistical, Nonlinear, and Soft Matter Physics* 77.6 (2008), p. 065201.

[55] F Haudin et al. “Vortex emission accompanies the advection of optical localized structures”. In: *Physical Review Letters* 106.6 (2011), p. 063901.

[56] D Pinto-Ramos et al. “Nonreciprocal coupling induced self-assembled localized structures”. In: *Physical Review Letters* 126.19 (2021), p. 194102.

[57] D Michaelis et al. “Universal criterion and amplitude equation for a nonequilibrium Ising-Bloch transition”. In: *Physical Review E* 63.6 (2001), p. 066602.

[58] P Coullet et al. “Breaking chirality in nonequilibrium systems”. In: *Physical review letters* 65.11 (1990), p. 1352.

[59] JM Gilli, M Morabito, and T Frisch. “Ising-Bloch transition in a nematic liquid crystal”. In: *Journal de Physique II* 4.2 (1994), pp. 319–331.

[60] D Haim et al. “Breathing spots in a reaction-diffusion system”. In: *Physical review letters* 77.1 (1996), p. 190.

[61] Marcel G Clerc, Saliya Coulibaly, and David Laroze. “Localized states and non-variational Ising–Bloch transition of a parametrically driven easy-plane ferromagnetic wire”. In: *Physica D: Nonlinear Phenomena* 239.1-2 (2010), pp. 72–86.

[62] Christiaan Huygens. *Horologium oscillatorium*. Apud F. Muguet, Paris, France, 1673.

[63] Engelbert Kaempfer. *The history of Japan (With a Description of the Kingdom of Siam)*. Posthumous translation; or reprint by McLehose, Glasgow, 1906. 1727.

[64] John Buck. “Synchronous rhythmic flashing of fireflies. II.” In: *The Quarterly review of biology* 63.3 (1988), pp. 265–289.

[65] Donald C Michaels, Edward P Matyas, and Jose Jalife. “Mechanisms of sinoatrial pacemaker synchronization: a new hypothesis.” In: *Circulation research* 61.5 (1987), pp. 704–714.

[66] Andrej G Vladimirov, Gregory Kozyreff, and Paul Mandel. “Synchronization of weakly stable oscillators and semiconductor laser arrays”. In: *Europhysics Letters* 61.5 (2003), p. 613.

[67] Kurt Wiesenfeld, Pere Colet, and Steven H Strogatz. “Frequency locking in Josephson arrays: Connection with the Kuramoto model”. In: *Physical Review E* 57.2 (1998), p. 1563.

[68] Robert Adler. “A study of locking phenomena in oscillators”. In: *Proceedings of the IRE* 34.6 (1946), pp. 351–357.

[69] Yoshiki Kuramoto. "Self-entrainment of a population of coupled non-linear oscillators". In: *International Symposium on Mathematical Problems in Theoretical Physics*. Ed. by Huzihiro Araki. Berlin, Heidelberg: Springer Berlin Heidelberg, 1975, pp. 420–422. ISBN: 978-3-540-37509-8.

[70] Yoshiki Kuramoto and Yoshiki Kuramoto. *Chemical turbulence*. Springer, 1984.

[71] Francisco A Rodrigues et al. "The Kuramoto model in complex networks". In: *Physics Reports* 610 (2016), pp. 1–98.

[72] Oleh E Omel'chenko. "The mathematics behind chimera states". In: *Nonlinearity* 31.5 (2018), R121.

[73] Hiroaki Daido. "Onset of cooperative entrainment in limit-cycle oscillators with uniform all-to-all interactions: bifurcation of the order function". In: *Physica D: Nonlinear Phenomena* 91.1-2 (1996), pp. 24–66.

[74] CI Del Genio. "The structure and dynamics of networks with higher order interactions". In: *Physics Reports* 1018 (2023), pp. 1–64.

[75] Y Kuramoto and D Battogtokh. "Coexistence of Coherence and Incoherence in Nonlocally Coupled Phase Oscillators". In: *Nonlinear Phenomena in Complex Systems* 5.4 (2002), pp. 380–385.

[76] Daniel M Abrams and Steven H Strogatz. "Chimera states for coupled oscillators". In: *Physical review letters* 93.17 (2004), p. 174102.

[77] Mark J Panaggio and Daniel M Abrams. "Chimera states: coexistence of coherence and incoherence in networks of coupled oscillators". In: *Nonlinearity* 28.3 (2015), R67.

[78] Eur Schöll. "Synchronization patterns and chimera states in complex networks: Interplay of topology and dynamics". In: *The European Physical Journal Special Topics* 225 (2016), pp. 891–919.

[79] Sindre W Haugland. "The changing notion of chimera states, a critical review". In: *Journal of Physics: Complexity* 2.3 (2021), p. 032001.

[80] Soumen Majhi et al. "Chimera states in neuronal networks: A review". In: *Physics of life reviews* 28 (2019), pp. 100–121.

[81] Fatemeh Parastesh et al. "Chimeras". In: *Physics Reports* 898 (2021), pp. 1–114.

[82] Aaron M Hagerstrom et al. "Experimental observation of chimeras in coupled-map lattices". In: *Nature Physics* 8.9 (2012), pp. 658–661.

[83] Mark R Tinsley, Simbarashe Nkomo, and Kenneth Showalter. "Chimera and phase-cluster states in populations of coupled chemical oscillators". In: *Nature Physics* 8.9 (2012), pp. 662–665.

[84] Simbarashe Nkomo, Mark R Tinsley, and Kenneth Showalter. "Chimera states in populations of nonlocally coupled chemical oscillators". In: *Physical review letters* 110.24 (2013), p. 244102.

[85] Jan Frederik Totz et al. "Spiral wave chimera states in large populations of coupled chemical oscillators". In: *Nature Physics* 14.3 (2018), pp. 282–285.

[86] Erik Andreas Martens et al. "Chimera states in mechanical oscillator networks". In: *Proceedings of the National Academy of Sciences* 110.26 (2013), pp. 10563–10567.

[87] Lennart Schmidt et al. “Coexistence of synchrony and incoherence in oscillatory media under nonlinear global coupling”. In: *Chaos: An Interdisciplinary Journal of Nonlinear Science* 24.1 (2014).

[88] Evgeny A Viktorov et al. “Coherence and incoherence in an optical comb”. In: *Physical review letters* 112.22 (2014), p. 224101.

[89] Mahesh Wickramasinghe and István Z Kiss. “Spatially organized dynamical states in chemical oscillator networks: Synchronization, dynamical differentiation, and chimera patterns”. In: *PloS one* 8.11 (2013), e80586.

[90] Rüdiger Seydel. *Practical bifurcation and stability analysis*. Vol. 5. Springer Science & Business Media, 2009.

[91] Eusebius J Doedel. “Lecture notes on numerical analysis of nonlinear equations”. In: *Numerical Continuation Methods for Dynamical Systems: Path following and boundary value problems* (2007), pp. 1–49.

[92] Herbert B Keller. “Numerical solution of bifurcation and nonlinear eigenvalue problem”. In: *Application of bifurcation theory* (1977).

[93] Eusebius J Doedel. “AUTO: A program for the automatic bifurcation analysis of autonomous systems”. In: *Congr. Numer* 30.265-284 (1981), pp. 25–93.

[94] Hannes Uecker. “Hopf Bifurcation and Time Periodic Orbits with pde2path – Algorithms and Applications”. In: *Communications in Computational Physics* 25 (Aug. 2017).

[95] H.B. Keller. *Numerical Methods for Two-point Boundary-value Problems*. Blaisdell book in numerical analysis and computer science. Blaisdell, 1968.

[96] Mustapha Tlidi et al. *Localized structures in dissipative media: from optics to plant ecology*. 2014.

[97] Thomas Heimburg and Andrew D Jackson. “On soliton propagation in biomembranes and nerves”. In: *Proceedings of the National Academy of Sciences* 102.28 (2005), pp. 9790–9795.

[98] Orazio Descalzi et al. *Localized states in physics: solitons and patterns*. Springer Science & Business Media, 2011.

[99] H-G Purwins, HU Bödeker, and Sh Amiranashvili. “Dissipative solitons”. In: *Advances in Physics* 59.5 (2010), pp. 485–701.

[100] Adrian Ankiewicz and Nail Akhmediev. *Dissipative solitons: from optics to biology and medicine*. Springer, 2008.

[101] K Nozaki and N Bekki. “Solitons as attractors of a forced dissipative nonlinear Schrödinger equation”. In: *Physics Letters A* 102.9 (1984), pp. 383–386.

[102] Michel A Ferré et al. “Localized structures and spatiotemporal chaos: comparison between the driven damped sine-Gordon and the Lugiato-Lefever model”. In: *The European Physical Journal D* 71 (2017), pp. 1–8.

[103] John Burke, SM Houghton, and Edgar Knobloch. “Swift-Hohenberg equation with broken reflection symmetry”. In: *Physical Review E* 80.3 (2009), p. 036202.

[104] Pedro Parra-Rivas et al. "Third-order chromatic dispersion stabilizes Kerr frequency combs". In: *Optics letters* 39.10 (2014), pp. 2971–2974.

[105] James Dickson Murray and James Dickson Murray. *Mathematical biology: II: spatial models and biomedical applications*. Vol. 18. Springer, 2003.

[106] Marcel Gabriel Clerc, Sebastian Echeverría-Alar, and Mustapha Tlidi. "Localised labyrinthine patterns in ecosystems". In: *Scientific Reports* 11.1 (2021), p. 18331.

[107] D Pinto-Ramos et al. "Vegetation covers phase separation in inhomogeneous environments". In: *Chaos, Solitons & Fractals* 163 (2022), p. 112518.

[108] D Pinto-Ramos, MG Clerc, and M Tlidi. "Topological defect law for migrating banded vegetation patterns in arid climates". In: *Science Advances* 9.31 (2023), eadf6620.

[109] Florent Bessin et al. "Gain-through-filtering enables tuneable frequency comb generation in passive optical resonators". In: *Nature communications* 10.1 (2019), p. 4489.

[110] Alan L Hodgkin and Andrew F Huxley. "A quantitative description of membrane current and its application to conduction and excitation in nerve". In: *The Journal of physiology* 117.4 (1952), p. 500.

[111] Yoshiki Kuramoto and Shin-ichiro Shima. "Rotating spirals without phase singularity in reaction-diffusion systems". In: *Progress of Theoretical Physics Supplement* 150 (2003), pp. 115–125.

[112] Shin-ichiro Shima and Yoshiki Kuramoto. "Rotating spiral waves with phase-randomized core in nonlocally coupled oscillators". In: *Physical Review E* 69.3 (2004), p. 036213.

[113] Patrick S Hagan. "Spiral waves in reaction-diffusion equations". In: *SIAM journal on applied mathematics* 42.4 (1982), pp. 762–786.

[114] Oleh E Omel'chenko, Matthias Wolfrum, and Edgar Knobloch. "Stability of spiral chimera states on a torus". In: *SIAM Journal on Applied Dynamical Systems* 17.1 (2018), pp. 97–127.

[115] Jianbo Xie, Edgar Knobloch, and Hsien-Ching Kao. "Twisted chimera states and multicore spiral chimera states on a two-dimensional torus". In: *Physical Review E* 92.4 (2015), p. 042921.

[116] E Omel'Chenko and Edgar Knobloch. "Chimerapedia: coherence–incoherence patterns in one, two and three dimensions". In: *New Journal of Physics* 21.9 (2019), p. 093034.

[117] W. J. Firth, L. Columbo, and T. Maggipinto. "On homoclinic snaking in optical systems". In: *Chaos: An Interdisciplinary Journal of Nonlinear Science* 17.3 (Sept. 2007), p. 037115.

[118] S. Barbay et al. "Homoclinic Snaking in a Semiconductor-Based Optical System". In: *Phys. Rev. Lett.* 101 (25 Dec. 2008), p. 253902.

[119] Uwe Thiele et al. "Localized states in the conserved Swift-Hohenberg equation with cubic nonlinearity". In: *Phys. Rev. E* 87 (4 Apr. 2013), p. 042915.

[120] Ramon Guevara Erra, Jose L. Perez Velazquez, and Michael Rosenblum. "Neural Synchronization from the Perspective of Non-linear Dynamics". In: *Frontiers in Computational Neuroscience* 11 (2017).

[121] Marcel G Clerc, Sebastián Echeverría-Alar, and Mustapha Tlidi. "Localized states with nontrivial symmetries: Localized labyrinthine patterns". In: *Physical Review E* 105.1 (2022), p. L012202.

[122] AJ Alvarez-Socorro, MG Clerc, and Mustapha Tlidi. "Spontaneous motion of localized structures induced by parity symmetry breaking transition". In: *Chaos: An Interdisciplinary Journal of Nonlinear Science* 28.5 (2018).

[123] Tobias J Kippenberg, Ronald Holzwarth, and Scott A Diddams. "Microresonator-based optical frequency combs". In: *science* 332.6029 (2011), pp. 555–559.

[124] "Mathematical aspects of heart physiology". In: *Courant Institute of Mathematical Science Publication, New York* (1975), pp. 268–278.

[125] John Buck and Elisabeth Buck. "Synchronous fireflies". In: *Scientific American* 234.5 (1976), pp. 74–85.